The Philosophical Magazine

UNIVERSITY OF HAWAII
LIBRARY
JAN 27

FIRST PUBLISHED IN 1798

A Journal of Theoretical Experimental and Applied Physics

Vol. 5 November 1960 No. 59
Eighth Series

25s. 0d., plus postage
Annual Subscription £13 10s. 0d., payable in advance

ALERE FLAMMAM

Printed and Published by
TAYLOR & FRANCIS LTD
RED LION COURT, FLEET STREET, LONDON, E.C.4

THE PHILOSOPHICAL MAGAZINE

Editor

Professor N. F. MOTT, M.A., D.Sc., F.R.S.

Editorial Board

Sir LAWRENCE BRAGG, O.B.E., M.C., M.A., D.Sc., F.R.S.
Sir GEORGE THOMSON, M.A., D.Sc., F.R.S.
Professor A. M. TYNDALL, C.B.E., D.Sc., F.R.S.

AUTHORS wishing to submit papers for publication in the Journal should send manuscripts directly to the Publishers.

Manuscripts should be typed in *double* spacing on one side of quarto (8 × 10 in.) paper, and authors are urged to aim at absolute clarity of meaning and an attractive presentation of their texts.

References should be listed at the end in alphabetical order of authors and should be cited in the text in terms of author's name and date. Diagrams should normally be in Indian ink on white card, with lettering in soft pencil, the captions being typed on a separate sheet.

A leaflet giving detailed instructions to authors on the preparation of papers is available on request from the Publishers.

Authors are entitled to receive 25 offprints of a paper in the Journal free of charge, and additional offprints can be obtained from the Publishers.

The *Philosophical Magazine* and its companion journal, *Advances in Physics*, will accept papers for publication in experimental and theoretical physics. The *Philosophical Magazine* publishes contributions describing new results, letters to the editor and book reviews. *Advances in Physics* publishes articles surveying the present state of knowledge in any branch of the science in which recent progress has been made. The editors welcome contributions from overseas as well as from the United Kingdom, and papers may be published in English, French and German.

The Fermi Surface in White Tin†

By A. V. Gold
Royal Society Mond Laboratory, University of Cambridge, and Division of Pure Physics, National Research Council, Ottawa, Canada‡

and M. G. Priestley
Royal Society Mond Laboratory, University of Cambridge

[Received July 25, 1960]

Abstract

The orientation dependence of the de Haas–van Alphen periods in tin single crystals has been studied in high pulsed magnetic fields. As many as seven periods have been found at some orientations, indicating that the Fermi surface is much more complicated than the 3-ellipsoid model suggested by Fawcett. The general degree of complexity of the results is much the same as that predicted by the free-electron model, but serious discrepancies are found when a detailed comparison is made. Effective mass values have been determined at the principal orientations from the temperature dependence of the amplitudes; these are compared with the results of cyclotron resonance experiments and with the free-electron orbit masses.

§ 1. INTRODUCTION

The period, P, of the de Haas–van Alphen oscillations in a metal single crystal at low temperatures is related to the extreme (maximum or minimum) area of cross section, $\mathscr{A}_0$, of the Fermi surface normal to the magnetic field by the Onsager–Lifshitz and Kosevich relation:

$$P = 2\pi e/c\hbar\mathscr{A}_0. \qquad (1)$$

($\mathscr{A}_0$ in $\mathbf{k}$-space), and from the temperature dependence of the oscillation amplitudes one can obtain the corresponding cyclotron (orbit) effective mass, m^*, which is defined by:

$$m^* = (\hbar^2/2\pi)(\partial\mathscr{A}/\partial E)_0. \qquad (2)$$

In principle a study of the variation of P and m^* with orientation is sufficient to determine the shape of the Fermi surface and the Fermi velocity at all points on the surface, and for a discussion of the present theoretical and experimental situation, the reader is referred to the review articles by Shoenberg (1957, 1960).

The orientation-dependence of the de Haas–van Alphen effect in metallic tin has been studied at magnetic fields up to 15 kG principally by Shoenberg

---

† Communicated by the Authors.

‡ N.R.C. Postdoctorate Fellow. Now at Physics Department, Iowa State University, Ames, Iowa, U.S.A.

(1952) and Berlincourt (1952), whose findings were, for the most part, consistent with a Fermi surface consisting of two small ellipsoids oriented along the tetragonal axis and capable of accounting for a total of about 10^{-2} carrier per atom at most. Subsequent preliminary studies using impulsive fields of up to 100 kG (Shoenberg 1953) revealed a rich variety of short-period de Haas–van Alphen oscillations associated with the major portions of the Fermi surface. A detailed orientation-dependence study of the periods in lead using the impulsive-field technique has been successful in determining the Fermi surface in this metal (Gold 1958; hereinafter referred to as (I)) and in this paper we describe such a study of metallic tin.

The high-field de Haas–van Alphen results turn out to be very complicated and are, in fact, of the same order of complexity as predicted by the simple free-electron model. We shall make use of this simple model, which proved helpful in the interpretation of the lead results, in an attempt to relate the observed results to the Brillouin zone scheme. However, we shall conclude that further information, in particular from de Haas–van Alphen studies at still higher fields and from ultrasonic attenuation, cyclotron resonance and magneto-resistance experiments, is necessary before all of the geometrical features of the Fermi surface can be established with reasonable certainty. We have also determined the effective masses corresponding to principal orientations; these are compared with the results of cyclotron resonance experiments and with the orbit masses predicted by the free-electron model.

§ 2. Experimental Results

The experimental method is the same as that described in (I) and in the review article by Shoenberg (1957), so that no further details will be given here. Since the high-field results are so complex, with up to seven periodic terms superimposed on one another at some orientations, it was essential to use the resonance method in order to sort out the various terms; the presence of a background of the other terms nevertheless resulted in a greater uncertainty of period measurement than was the case for the simpler lead results (I). The measurements were carried out on single crystal wires of length 8 mm and diameter 0·55 mm; these were prepared from Johnson Matthey spectroscopically pure tin and grown with a principal crystallographic axis along the wire. As was explained in (I), the absolute orientation of the crystal axes relative to the magnetic field was obtained finally from the symmetry of the period-orientation results. The period measurements were carried out at 1·2°K and using field pulses rising up to 80 kG in about 11 ms. A few measurements were also made along [001] and [110] in a field of 150 kG; this became possible (using a specially designed field coil) only after the bulk of the measurements had been completed. The higher field greatly increased the observed amplitudes but revealed no new very short periods.

Fig. 1

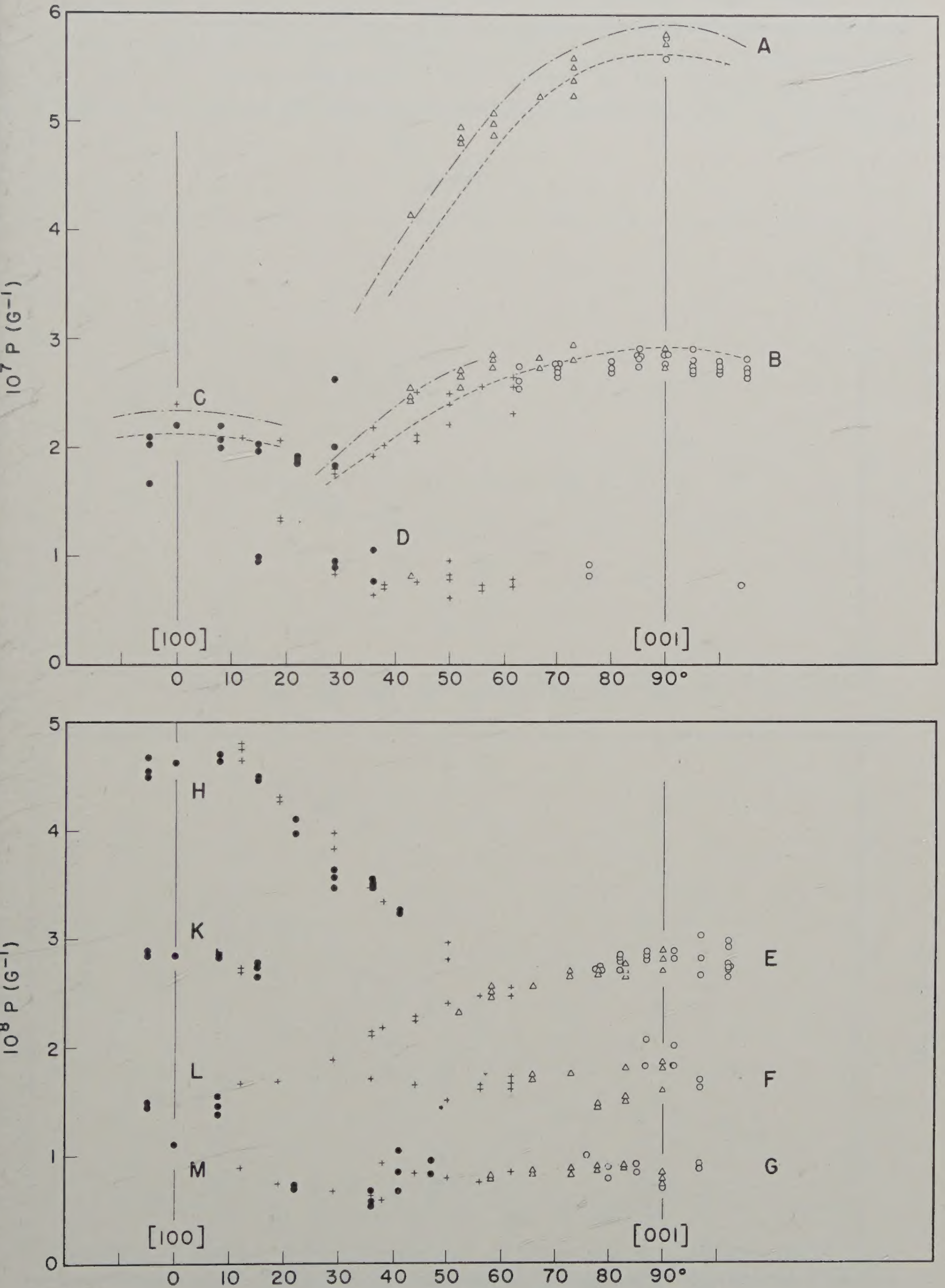

Variation of period with orientation of magnetic field in a (100) plane. Upper half: long-period oscillations; lower half: short-period oscillations. ○, △, specimens with [001] axis along wire; ●, specimen with [100] axis along wire; +, specimen with axis midway between [100] and [001] along wire. —·—·, Shoenberg (1952); – – –, Berlincourt (1952).

Fig. 2

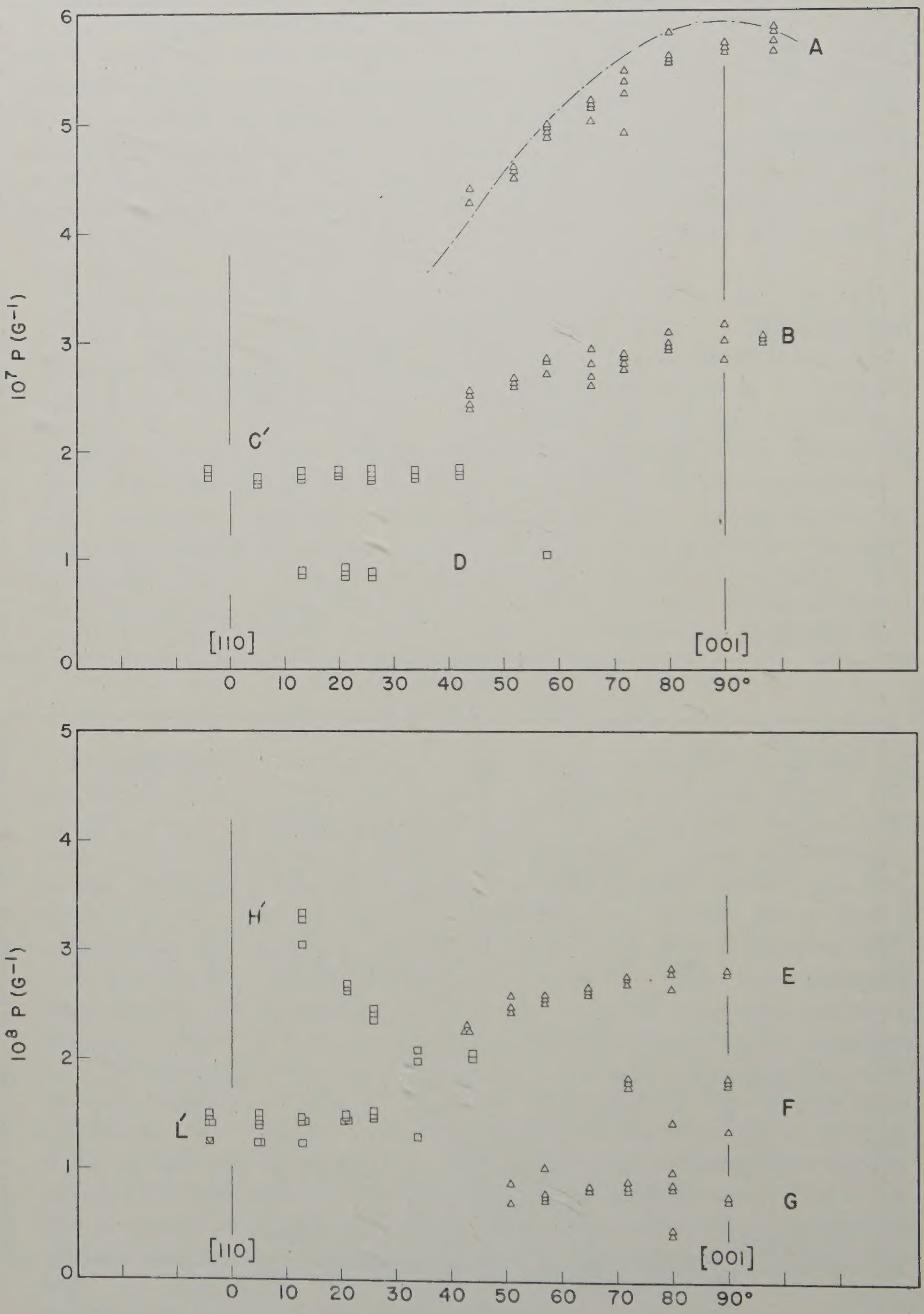

Variation of period with orientation of magnetic field in a (110) plane. Upper half: long-period oscillations; lower half: short-period oscillations. △, specimen with [001] axis along wire; □, specimen with [110] axis along wire. —·—·, Shoenberg (1952).

Figures 1, 2 and 3 show the variation of the periods with orientation of magnetic field in the (100), (110) and (001) planes, respectively. The results fall, broadly speaking, into two groups: long-period oscillations with $P \sim 10^{-7}\,\text{G}^{-1}$ (upper diagrams) and short-period oscillations with $P \sim 10^{-8}\,\text{G}^{-1}$ (lower diagrams). Also shown in the figures are smooth curves drawn through the long-period data obtained earlier by Shoenberg

Fig. 3

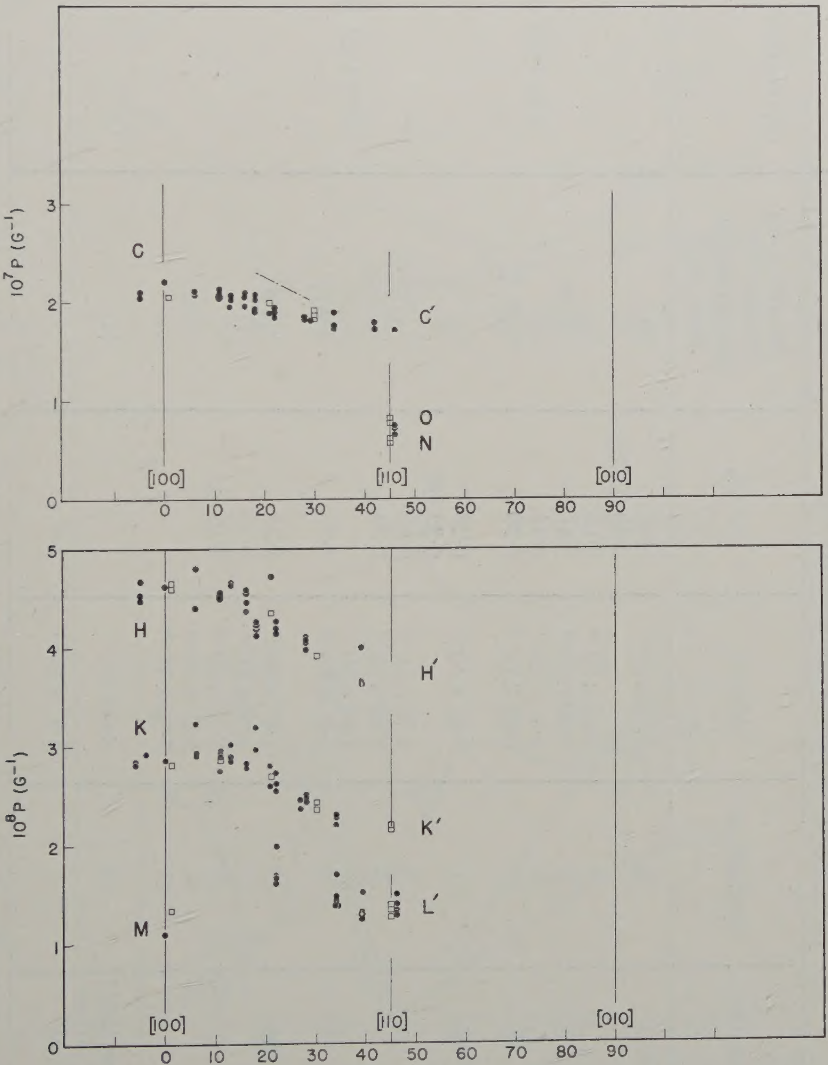

Variation of period with orientations of magnetic field in the (001) plane. Upper half: long-period oscillations; lower half: short-period oscillations. ●, specimen with [100] axis along wire; □, specimen with [110] axis along wire. —·—·, Shoenberg (1952).

Table 1

Observed periods and effective masses					m^*/m_0 from other experiments
Orientation	Oscillations	P(G^{-1})	m^*/m_0	Possible free-electron-like interpretation. Zone, orbit	
[001]	A	5.70×10^{-7}	0·09	3δ	
			0·10 (B, S)		
	B	$2{\cdot}85\times10^{-7}$	0·15	5μ	
	E	$2{\cdot}80\times10^{-8}$	0·51	$4\,(b)\tau$	
	F	$1{\cdot}8\ \times10^{-8}$	0·64	5σ	0·78, 0·60, 0·54, 0·47 (KH)
	G	$0{\cdot}88\times10^{-8}$	0·70	$4\,(a)\ \zeta$	
[100]	C	$2{\cdot}10\times10^{-7}$	0·26	3γ	
			0·22 (B)		
	H	$4{\cdot}70\times10^{-8}$	0·45	$4\,(b)\xi(?)$	
	K	$2{\cdot}86\times10^{-8}$	0·50	$5\chi(?)$	
	L	$1{\cdot}45\times10^{-8}$		(?)	0·88, 0·27, 0·26 (KH)
	M	$1{\cdot}1\ \times10^{-8}$	1·27	$4\,(a)\eta$	
[110]	C′	$1{\cdot}6\ \times10^{-7}$	0·34	$3\gamma(?)$	
	L′	$1{\cdot}35\times10^{-8}$	0·75	(?)	
	K′	$2{\cdot}16\times10^{-8}$	1·16	(?)	
	N	$5{\cdot}7_7\times10^{-8}$		$4\,(a)\epsilon'$	
	O	$7{\cdot}8_5\times10^{-8}$		3ϵ	
Between [001] and [100] or [110]	D	$\doteqdot 0{\cdot}8$ to $0{\cdot}9\ \times10^{-7}$		(?)	

Notes: m_0 is the free-electron mass and the values of m^*/m_0 are reliable to about 10%. There was some indication of oscillations of period $0{\cdot}4\times10^{-8}$ G^{-1} at orientations roughly midway beween [100] and [110]; however this feature was not reproducible and can probably be ascribed to noise effects. B, Berlincourt (1952); KH, Khaikin (1959); S, Shoenberg (1952). It is not certain which of the diad axes [100] or [110] Khaikin refers to.

(1952) and Berlincourt (1952) using the couple method at fields up to 15 kG, and it is satisfactory that the corresponding high-field results agree with the earlier low-field data. In table 1 we give values of the period and of the associated orbit effective mass at the principal orientations [001], [100] and [110].

Fig. 4

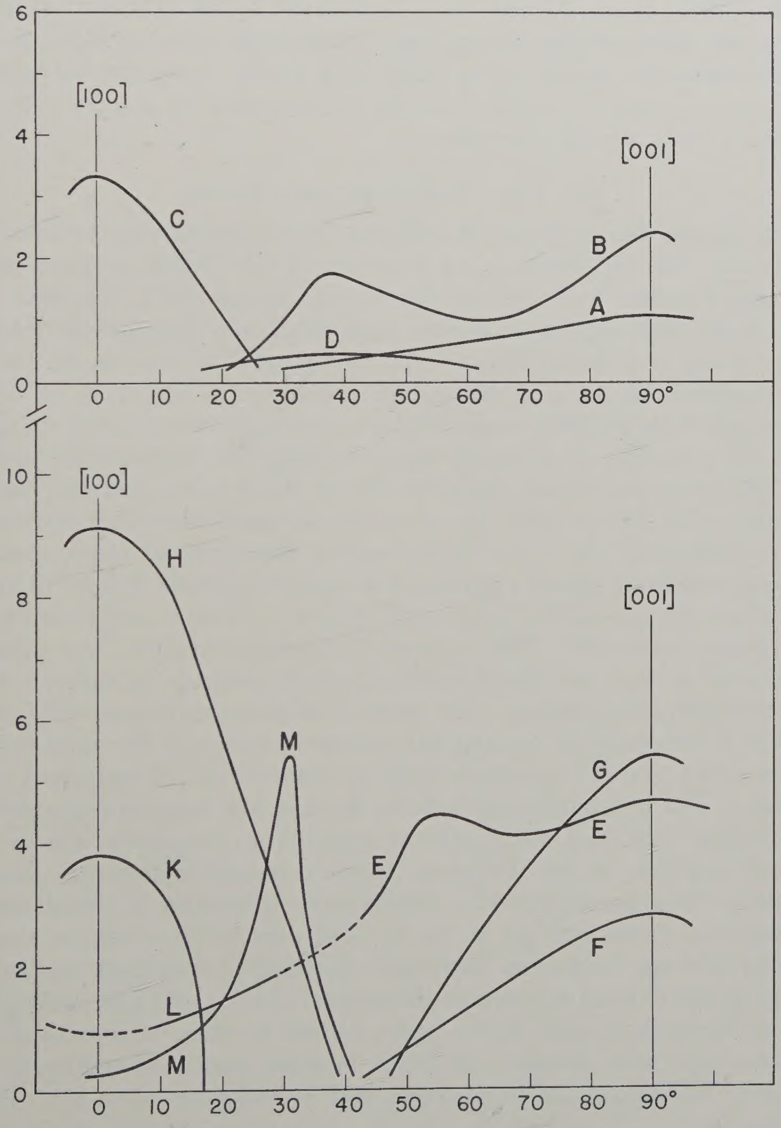

Variation of amplitudes with orientation of magnetic field in a (100) plane at 1·2°K (schematic). Upper half: long-period oscillations; lower half: short-period oscillations. The two drawings are on the same scale and the maximum amplitude corresponds to $|dI/dH| \sim 10^{-2}$.

Because of the considerable scatter of the experimental points and the rapid orientation dependence of amplitude (see fig. 4), it is not possible to decide unambiguously how to join up the experimental points into curves, without appeal to some theoretical model. For instance it is not clear whether the curve L in fig. 1 is a separate branch existing over only a limited angular range or whether it is an extension of E or of F, and there are clearly many similar ambiguities. For lead (I) certain features of the Fermi surface could be inferred by straightforward inspection of the data and the surfaces were then fitted into the Brillouin zone scheme using the free-electron model as a guide; however, we now find that for tin some theoretical model is necessary to suggest the very nature of the surfaces themselves.

§ 3. The Free-Electron Model

The simple free-electron model has been remarkably successful in accounting for the geometrical features of the Fermi surfaces in the polyvalent metals lead (I) and aluminium (Heine 1957, Harrison 1959, 1960) and it now appears to have a good theoretical foundation (Harrison 1960, Cohen and Heine 1960). We now appeal to this model for help in understanding the complex period variations in figs. 1, 2 and 3.

The primitive Brillouin zone for the white-tin lattice is shown in fig. 5†. Since the primitive zone always accommodates two electrons per smallest unit cell of the real lattice and since for tin the smallest unit cell contains two atoms, it follows that the zone can accommodate one electron per atom. Assuming tin to have four valence electrons per atom, these can be accommodated within a sphere in **k**-space of volume $8(2\pi/a)^3(a/c)\,\mathrm{cm}^{-3}$ and hence radius $1{\cdot}518\ (2\pi/a)\,\mathrm{cm}^{-1}$, where $a=5{\cdot}82\,\text{Å}$ and $c=3{\cdot}18\,\text{Å}$ are the lattice constants. This sphere completely encloses the primitive (first) zone so that the Fermi surface must lie entirely in higher zones in the extended zone scheme. In order to make comparison with experiment it is necessary to re-map the various portions of the surface in the higher zones into the primitive zone by translations of reciprocal lattice vectors. The extended zone scheme for the tin structure is extremely complicated and the very tedious remapping procedure was in part carried out for us by Petersen (private communication). Recently Harrison (1959) has described a much simpler procedure by which sections through the Fermi surface in the reduced zone scheme can be obtained directly and we have used Harrison's method to construct the surfaces shown in fig. 5, from sections in the central (100), (110) and (001) planes. The surfaces have been drawn more or less to scale, except that sharp corners have been rounded off, both because such a rounding is to be expected on account of band gaps, and in order to make the diagram clearer.

---

† The zone has been incorrectly described by Mott and Jones (1936); for a further discussion see Chambers (1956) and Barron and Fischer (1959). Space-group considerations of the tin structure have been given by Mase (1959).

Fig. 5.

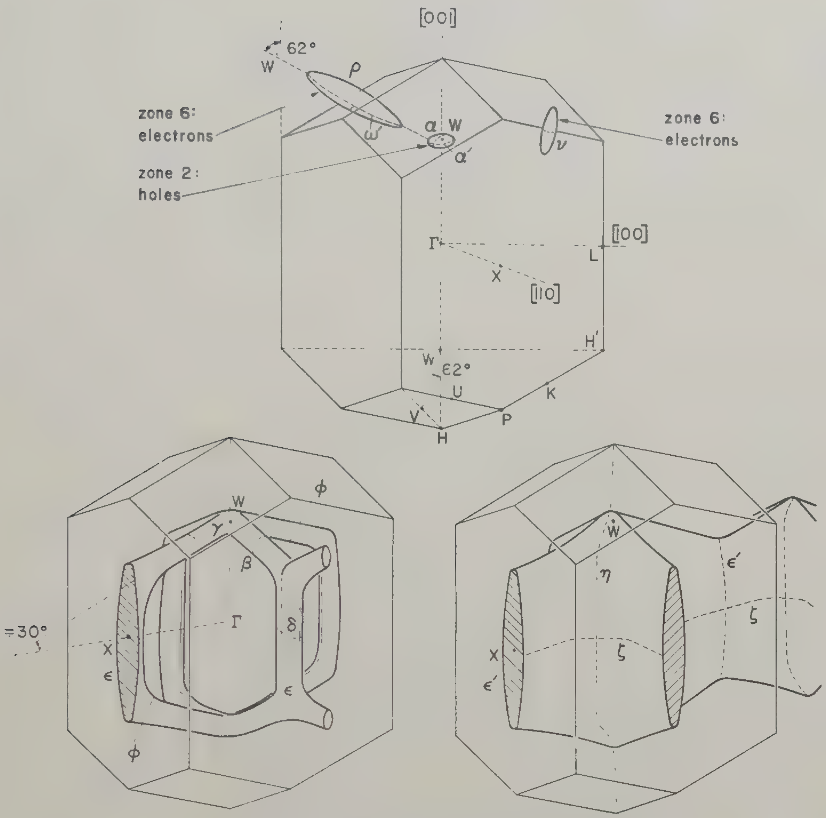

zone 3: holes

zone 4: (a) holes

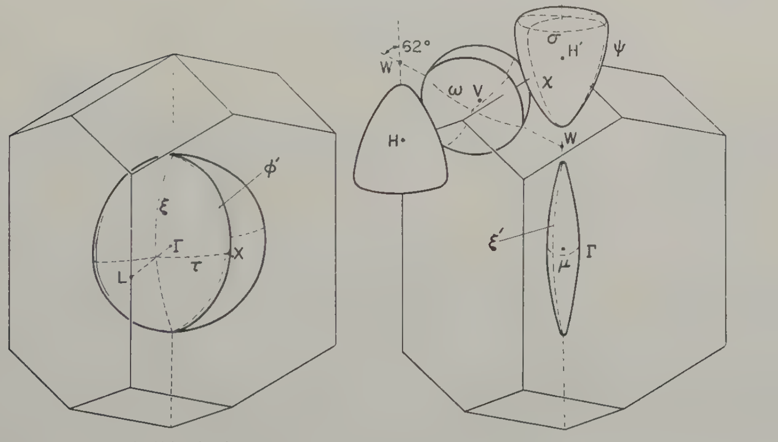

zone 4: (b) electrons

zone 5: electrons

The free-electron Fermi surface in the reduced-zone scheme. The principal dimensions of the zone are:

$$\Gamma\,\mathrm{L}=\frac{2\pi}{a},\quad \Gamma\,\mathrm{X}=\frac{1}{2}\left(\frac{2\pi}{a}\right),\quad \Gamma\,\mathrm{W}=\mathrm{LH}=\frac{1}{2}\left(\frac{a}{c}-\frac{c}{a}\right)\left(\frac{2\pi}{a}\right),\quad \mathrm{WH}=\left(\frac{c}{a}\right)\left(\frac{2\pi}{a}\right),$$

where $a=5{\cdot}82$ Å and $c=3{\cdot}18$ Å.

The predictions of the free-electron model are then as follows. The first zone is entirely filled and the second and third ones nearly so, except for two small pockets of holes centred on the points W in the second zone and a multiply-connected surface containing holes in the third zone. In the fourth zone the Fermi surface is one of two sheets and consists of a singly-connected surface 4 (*b*) formed by the intersection of two 'pancakes' containing electrons; this surface is surrounded by a region of unoccupied states which is in turn bounded by the multiply-connected surface 4 (*a*). In fig. 6 we show the central (001) section through the fourth zone, from which the relationship of the two surfaces to one another should become clear. The surfaces in the fifth zone all contain electrons and consist of a long ellipsoid along the tetragonal axis, 'pear-shaped' surfaces centred on the zone corners H (two surfaces per zone) and surfaces similar to that in zone 4 (*b*), but tilted and centred on the points V (four surfaces per zone). Finally we have in the sixth zone small ellipsoidal surfaces centred on the points V and still smaller ellipsoids centred on the points K, and inclined as shown; both sets of ellipsoids contain electrons.

Fig. 6

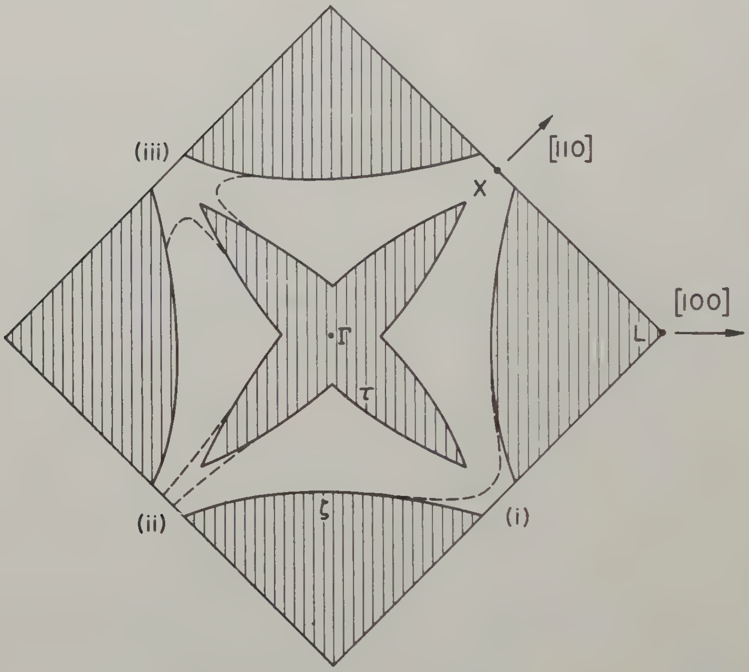

The central (001) section through the fourth zone showing the relation of the surfaces in zones 4 (*a*) and 4 (*b*) (fig. 5) to one another. The shaded regions are occupied.

We have indicated with broken curves in fig. 5 the principal orbits of maximum or minimum area of cross-section which would be expected to give rise to a de Haas–van Alphen effect. These orbits are labelled with small Greek letters and the associated de Haas–van Alphen periods from eqn. (1) are given in table 2. As Harrison (1960) has pointed out, his method of constructing the Fermi surface in the reduced-zone scheme also enables one to find the free-electron orbit masses (eqn. (2)) in a straightforward manner, and these masses are also given in table 2.

Table 2. The free electron model

Orientation	Zone, orbit	P(G^{-1})	m^*/m_0
[001]	2α	6×10^{-7}†	0·05†
	3δ	$4{\cdot}5\times10^{-7}$	0·061
	5μ	$1{\cdot}8\times10^{-7}$	0·089
	$4\ (b)\tau$	$2{\cdot}6\times10^{-8}$	0·40
	5σ	$1{\cdot}0\times10^{-8}$†	0·3†
	$4\ (a)\zeta$	$0{\cdot}87\times10^{-8}$	0·38
[100]	$2x'$	$6{\cdot}6\times10^{-7}$	0·055
	3γ	$5{\cdot}5\times10^{-7}$	0·083
	5ω	$8{\cdot}0\times10^{-8}$	0·50
	$6\omega'$		
	$4\ (b)\xi$	$3{\cdot}8\times10^{-8}$	0·32
	$5\xi'$		
	5χ	$1{\cdot}8\times10^{-8}$	0·28
	$4\ (a)\eta$	$0{\cdot}75\times10^{-8}$	0·42
[110]	3ϵ	6×10^{-8}†	0·2†
	$4\ (a)\epsilon'$		
	$5\xi'$	$5{\cdot}2\times10^{-8}$	0·23
	5ψ	$1{\cdot}4\times10^{-8}$	0·34
	3ϕ	$0{\cdot}94\times10^{-8}$	1·00
	$4\ (b)\phi'$		
28° from [100] in (100) plane	6ρ	6×10^{-7}†	
≑30° from [110] in (110) plane	3β	6×10^{-7}†	

† Estimated values.

§ 4. COMPARISON WITH EXPERIMENT

Before carrying out a detailed comparison with experiment we note that the number of periods to be expected on the basis of the free-electron model is about nine when the magnetic field is along the [001] direction, and considerably more at other orientations. In practice the *maximum* number found at any orientation is about seven (figs. 1, 2 and 3), suggesting either that the actual Fermi surface may not be quite as complex as the literal free-electron model would predict or that some periods are being missed because of low amplitude. One can get some idea about which of the free-electron periods might be absent from considerations of the x-ray structure factor, which vanishes across the vertical {110} planes of the zone but not across the inclined {101} planes (Mott and Jones 1936, p. 164). This leads us to suggest that the (001) section through Γ of the actual Fermi surface might not be too different from that in the free-electron model, but small portions of the surface near the upper and lower ends of the zone might be considerably affected by the presence of energy gaps. In particular, the zones one to five are degenerate at the zone corner H in the free-electron model, but in going from H in the first zone to the corresponding point in the fifth zone we must cross four planes of the type {101} with non-vanishing structure factor; this means that we might expect the 'pear-shaped' surfaces centred on H to be reduced in size. Such considerations lead us to suggest that the small pockets of holes at W in the second zone may be filled, and that the two sets of ellipsoidal surfaces in the sixth zone together with the thin 'intersecting pancake' surfaces in the fifth zone may all be absent. Our simplifying proposals find some justification in the fact that we have found no experimental evidence for the particular period anisotropies expected for these surfaces; thus, for example, we should expect one of the larger ellipsoids in the sixth zone to exhibit a period *maximum* when the field is inclined at 28° to [100] in the (100) plane (i.e. field along the axis of an ellipsoid), but as can be seen from fig. 1 this does not happen. Again, the proposed simplifications result in a considerable reduction in the total surface area and so are, broadly speaking, in keeping with Chambers' (1952) findings that the total surface area is only 0·43 times the free electron value. In what follows we shall therefore compare the results of figs. 1, 2 and 3 with the surfaces in only the four lower diagrams of fig. 5, but excluding the thin 'intersecting pancake' surfaces in the fifth zone.

It is convenient to begin by considering first of all the long-period oscillations (upper halves of figs. 1, 2 and 3) which arise from the smaller portions of the Fermi surface. The period variations in both (100) and (110) planes of the groups A and B can be accounted for by surfaces of revolution parallel to the [001] axis; the angular variation of group A is approximately as the cosine of the angle measured from the [001] axis, thus suggesting a more or less cylindrical surface with its axis along [001], while that of group B is less rapid than the cosine suggesting a convex surface. According to the free-electron model we could therefore associate the A and B oscillations with the orbits δ and μ respectively and we see from tables 1 and 2 that the observed periods are in fact reasonably close to the free-electron values. We do not expect to be able to follow the A and B oscillations all the way to the [100] and [110] orientations since the orbits δ are then no longer defined while the orbit ξ' of the fifth-zone ellipsoid is not particularly favourable for a de Haas–van Alphen effect. These considerations suggest then that the C oscillations, which are strongest at [100], are not connected with the groups A and B and we tentatively ascribe them to the orbits γ of the third-zone surface. However the C oscillations extend all the way to [110] (C′ in fig. 3) and this is only possible if the slanting arms of the multiply-connected surface are not present (i.e. 'pinched off' near W). This proposal is supported by the fact that fig. 2 reveals no oscillations which can reasonably be ascribed to the β-orbits round these arms; the existence of β-orbits would require a period which had a *maximum* value at about 30° from [110] in a (110) plane (fig. 2). Finally, the very weak oscillations D are too vague to suggest anything definite.

We now turn to the short-period oscillations (lower halves of figs. 1, 2 and 3) which are related to much larger portions of the Fermi surface. The magnitudes of the three periods E, F and G observed at [001] agree reasonably well with the three short periods τ, σ, ζ, respectively, predicted by the free-electron model. The G oscillations are fairly isotropic away from [001] and this might be accounted for by the fact that the free-electron orbit η in zone 4 (a) is actually concave where it crosses the orbit ζ, so that the area of the orbit ζ would not be expected to vary much when the field is tilted some 30° to 40° from [001].

The short periods found near [100] and [110] have not, however, found a plausible interpretation in terms of the free-electron model. Thus the M oscillations, which probably have a maximum period at [100], might be associated with the orbits η in zone 4 (a), but their amplitude variation (fig. 4) finds no plausible explanation. Again the H and H′ branches might be associated with the orbits ξ in zone 4 (b), but they do not appear to join smoothly with the E branch as would be required by this interpretation. The results of fig. 1 and fig. 4 in fact strongly suggest that it is the L oscillations which join smoothly to E (i.e. that it is L which must be associated with ξ) but the period *minimum* L at [100] does not fit in with the model. It can be seen that the free-electron model predicts three short periods near [100] corresponding to the orbits ξ, χ and η, while actually four, viz. H, K, L and M, are observed. Finally we should expect strong oscillations corresponding to the orbits ϵ' of zone 4 (a) with a period *maximum* at [110], but no such maximum is observed; the weak oscillations N, observed only at [110], have about the right period, but this may be fortuitous. The further weak period O also found only at [110] might be due to the orbit ϵ in zone 3.

It is natural to enquire if slight modifications of the free-electron model might not help to eliminate the major discrepancies pointed out above. It turns out that only small changes are required to produce quite marked changes in the connectivity of the Fermi surface in the fourth zone. For instance the modification (i) of fig. 6 is rather attractive since it would remove the need for explaining the apparent lack of oscillations from the orbit ϵ', which would require a period maximum at [110]; although the orbit ζ is then round a region of unoccupied states rather than occupied states, the area enclosed by the orbit remains practically unaltered by this modification. On the other hand, modification (ii) would make the orbit τ larger than the orbit ζ, requiring a still shorter period at [001] and *two* period maxima at [110], while (iii) would join orbits τ and ζ into one much smaller orbit which cannot now account for the two shortest periods at [001]. None of these modifications can, however, account for the presence of the *four* periods H, K, L and M, near [100] nor for the cylinder or hyperboloid of revolution about [100] which is required to explain the oscillations H, H′. In fact the only way in which such a cylinder or hyperboloid might fit into the framework of the free-electron scheme is by supposing the surfaces shown at the top of the fifth zone (fig. 5) to be reduced in size and yet to be so merged together as to form a multiply-connected surface of tubes whose axes lie along [100] axes through V. These [100] tubes could then give rise to the oscillations H while the oscillations F might conceivably be associated with a hole orbit around four tubes. This would also require an additional short period at [110]; the period L′ is of the right order of magnitude but it should be a maximum rather than a minimum at [110].

We conclude that the general degree of complexity of the experimental results is much the same as that of the free-electron model and that some of the details, notably the observed periods near [001], agree reasonably well with it. The serious discrepancies at other orientations, however, suggest considerable departures from the free-electron scheme, but it is hardly worth while speculating further about conceivable departures until more accurate and detailed data are available or until a better theoretical model is proposed with which the data can be compared. A ‘tight-binding’ calculation might be of help in suggesting surfaces to account for the short-period results in particular, and such a calculation is at present being carried out by Dr. M. Miasek.

§ 5. DISCUSSION OF OTHER RELEVANT EXPERIMENTS

A certain amount of information about the Fermi surface in tin is available from other types of experiment and this will now be briefly reviewed.

The anomalous skin effect was studied by Fawcett (1955) (see also Chambers 1956) and though it is now clear that the 3-ellipsoid model he used to interpret his results is far too simple, the interpretation of the present results is far from definite enough to allow detailed comparison with Fawcett's data. It is however worth mentioning that the free-electron surface of fig. 5 is quite capable of reproducing the salient features of the anisotropy in the surface conductivity. Thus the large radii of curvature of the orbits ζ and η in zone 4 (a), especially in the region where they cross, would result in a high surface conductivity when either the [001] or one of the [100] axes lies in the surface of the sample, which is just what Fawcett finds. It is impossible at this stage to deduce a value of the total surface area for comparison with Chambers' (1952) result of

0·43 times the free-electron value†, and the same holds for a comparison with the electronic specific heat.

The most detailed study so far of cyclotron resonance in tin is that of Khaikin (1959) and, as can be seen from table 1, Khaikin's masses at [001] are in fair agreement with the de Haas–van Alphen ones. However, the agreement is poorer at [100], but it is not clear if [100] is the diad axis to which Khaikin refers. The high value of $m^* = 8{\cdot}5m_0$ found by Khaikin at an intermediate orientation is indicative of a large closed orbit extending through several cells of the reciprocal lattice and the free-electron model would suggest that this is most likely to be associated with the multiply-connected surface of zone 4 (*a*). Assuming a free-electron-like interpretation of the present results, the de Haas–van Alphen effective masses are in as reasonable agreement with the free-electron ones as one might expect (tables 1 and 2), bearing in mind the discrepancies observed in other metals (Harrison 1960). Cyclotron resonance experiments using circularly polarized radiation would be most helpful in deciding which of the surfaces contain electrons and which holes.

The magneto-resistance results of Alekseevski and Gaidukov (1959) suggest that the Fermi surface of tin has open directions along [100] and [110] but this conclusion is based on only preliminary results. Further evidence on open orbits comes from ultrasonic attenuation experiments. Olsen and Morse (1959) find open orbits but no details are given. Mackintosh (private communication) also finds evidence for open directions along [100] and [110]. The suggestion of open orbits along [100] is not inconsistent with the de Haas–van Alphen data (see pp. 1101, 1102) but we have found no period maxima at [100]; however, further comparison is premature until more detailed results are available.

ACKNOWLEDGMENTS

We are indebted to Dr. D. Shoenberg, F.R.S., for his keen interest in this work and for his continued encouragement and advice. We are also grateful to Dr. R. F. Petersen for giving us sketches of parts of the Fermi surface in the reduced-zone scheme, to Dr. G. Fischer and Dr. V. Heine for helpful discussions and to Mr. H. L. Davies for help with the experiments.

Note added in proof.—We wish to point out that the free-electron surface of fig. 5 has been constructed assuming that electrons are Bragg-reflected at all proper Brillouin-zone planes whether or not the structure factor is zero; a vanishing structure factor does not necessarily imply an energy gap which is identically zero over the whole plane (see refs. at foot of p. 1096 Crystal symmetry requires the energy gap on the {110} zone faces, which have vanishing structure factor, to be zero *only* along the lines XL and XP

---

† Dr. Fawcett has informed us that his figure of 0·39 is low on account of a calibration error.

(Mase 1959; we are grateful to Dr. J. M. Keller for pointing this out to us). It appears that the only important alteration in the free-electron model brought about by this requirement is that an electron initially moving round orbit ζ in zone 4 (a) will continue round half the orbit δ in zone 3 after contacting the line XL of the (110) face, and so on. This results in a 'four-cornered rosette' orbit normal to [001] whose maximum linear extension (along [110]) is somewhat larger than that of the zone but whose area is practically the same as the original orbit ζ. However such a 'freak' orbit would have vanishingly small statistical weight and we have found no convincing experimental evidence for it.

References

Alekseevski, N. E., and Gaidukov, Yu., P., 1959, *J. exp. theor. Phys., U.S.S.R.*, **37,** 672.

Barron, T. H. K., and Fischer, G., 1959, *Phil. Mag.*, **4,** 826.

Berlincourt, T. G., 1952, *Phys. Rev.*, **88,** 242.

Chambers, R. G., 1952, *Proc. roy. Soc.* A, **215,** 481; 1956, *Canad. J. Phys.*, **34,** 1395.

Cohen, M. H., and Heine, V., 1960 (to be published).

Fawcett, E., 1955, *Proc. roy. Soc.* A, **232,** 519.

Gold, A. V., 1958, *Phil. Trans.* A, **251,** 85.

Harrison, W. A., 1959, *Phys. Rev.*, **116,** 555; 1960, *Ibid.*, **118,** 1190.

Heine, V., 1957, *Proc. roy. Soc.* A, **240,** 340.

Khaikin, M. S., 1959, *J. exp. theor. Phys., U.S.S.R.*, **37,** 1473.

Mase, S., 1959, *J. phys. Soc., Japan*, **14,** 1538.

Mott, N. F., and Jones, H., 1936, *Theory of Metals and Alloys* (Oxford: Clarendon Press).

Olsen, T., and Morse, R. W., 1959, *Bull. Amer. phys. Soc.* II, **4,** 167.

Shoenberg, D., 1952, *Phil. Trans.* A, **245,** 1; 1953, *Physica*, **19,** 791; 1957, *Progress in Low Temperature Physics*, Vol. II, ed. C. J. Gorter (Amsterdam: North Holland Publ. Co.); 1960, *Proc. Intl. Conf. on Fermi Surfaces in Metals* (New York: Wiley).

The Determination of the Flux of Cosmic Ray Protons with Nuclear Emulsions†

By C. J. Waddington
H. H. Wills Physical Laboratory, University of Bristol

[Received June 1, 1960]

Abstract

The flux of protons in the primary cosmic radiation has been determined in a stack of nuclear emulsions exposed during 1954 over northern Italy. This determination, which depended on the observation of the nuclear interactions produced by the protons, gave a flux at the top of the atmosphere of 500 ± 70 protons/m^2 ster sec, a value in good agreement with that expected from counter measurements. A simple model of the variation of the proton flux with depth in the atmosphere has been derived which appears to be in reasonable agreement with the experimental data.

§ 1. Introduction

Nuclear photographic emulsions have been extensively used to investigate the heavier components of the primary cosmic radiation, but have not provided much information on the primary protons‡. Present data on these particles come entirely from measurements made with electronic counters. In particular, the Čerenkov-scintillator array of McDonald (1956) (see also McDonald and Webber (1959)) is almost entirely responsible for our present knowledge of the fluxes of these particles, since only this equipment appears able to discriminate adequately against the large background of upward moving albedo particles. Even this equipment, however, is unable to eliminate the re-entrant albedo, since these particles, which are predominantly electrons (McDonald and Webber 1959), have the same direction of flight as do those of primary origin. An alternative method of measuring these fluxes, and one which preferably discriminates against the re-entrant albedo, is thus very desirable. Such a method is provided by determining the flux from the nuclear interactions produced in nuclear emulsions.

§ 2. Method

When emulsions are used to investigate the heavier particles of the primary radiation it is usual to detect these nuclei by searching a given area for their tracks and from the frequency determining the flux. Such a procedure is hardly practical in the case of the primary protons due to the extremely tenuous nature of the tracks left by fast singly-charged particles as they traverse the emulsion. Furthermore, even if by very careful scanning it were possible to detect *all* the tracks of particles producing minimum ionization which crossed a given area in the emulsions, it would be extremely difficult to distinguish the tracks left by protons from those left by other energetic but secondary singly-charged particles. Nor, in general, would it be possible to obtain any indication of the direction of motion of these particles.

---

† Communicated by the Author.

‡ In what follows no distinction will be made between protons and the other isotopes of hydrogen that may be present in the primary cosmic radiation.

The nuclei of the primary radiation may, alternatively, be detected by observing the nuclear interactions, or 'stars', that they produce while passing through the emulsions. Until recently the determination of absolute fluxes from the frequency of these stars was also impracticable, due to the extreme difficulty of locating *all* the interactions that are produced in any given volume. However, now that systematic observations with beams of artificially accelerated protons are available, these detection inefficiencies can be calculated and allowed for.

The additional requirement that the observed particles should produce a nuclear interaction has the great advantage that it serves to remove all those weakly interacting secondary particles, i.e. μ-mesons and electrons, from the sample being considered, and thus greatly reduces the problem of how to take account of the albedo particles. The short lifetime of π-mesons means that the majority of those produced at any distance from the emulsions will have decayed to weakly interacting particles before they arrive. Thus only locally produced mesonic secondary particles are detected, and if the volume searched for stars is chosen to be near the top of the emulsion stack, then these will be predominantly upward moving, and can usually be eliminated from a study of the characteristics of the stars. The only serious contamination by secondary particles would appear to be that due to knock-on protons and to protons produced by the break-up of heavy nuclei above the emulsions. It appears to be possible to make a reasonable estimate of the abundance of these particles, and thus to calculate the flux at the top of the atmosphere.

§ 3. EXPERIMENTAL DETAILS

While no emulsion stacks which had been exposed at the same time as a Čerenkov-scintillor array were available in this laboratory, there was one which had a closely similar α-particle flux to that measured by counters. This stack was exposed on September 14, 1954 over northern Italy, and has previously been used to measure the α-particle flux and energy spectrum (Fowler and Waddington 1956), and the flux and charge spectrum of the heavier nuclei (Waddington 1957 a, Hillier and Rajopadhye 1958). This stack consists of 80, 6 in. × 8 in. 600 μ G5 emulsions, and was exposed for 5·75 hours at an altitude of about 106 000 ft. The flight curve has been published previously, e.g. the E stack (Rajopadhye and Waddington 1958).

A volume, all of which was less than 1 cm from the top of this stack, was scanned for stars which satisfied the following conditions.

(i) The star lay within the inner 80% of the emulsion thickness, since stars near an emulsion face are difficult to analyse.

(ii) Each star had to have three or more black or grey tracks ($N_h \geqslant 3$), one of which had a potential range more than 60 microns. This requirement on length removes those stars due to radioactive decays in the emulsion.

Each of the stars found was carefully examined under high magnification by one or two observers for the presence of minimum tracks produced by fast primary or secondary particles. In those cases where such a track was found to lie within 60° of the vertical the star was, with a few exceptions discussed later, denoted as one produced by an energetic downward moving particle. The flux of these particles, $J(X)$, which are assumed to be all protons, that is, neglecting any downward meson component, is then given by

$$J(X) = \frac{\lambda \, dN}{V \, . \, \Omega \, . \, t} \text{ particles/m}^2 \text{ ster sec} \quad . \quad . \quad . \quad . \quad (1)$$

where λ is the interaction mean free path of protons in emulsion, measured in metres, dN is the number of stars produced by these protons, V is the scanned volume in cubic metres, Ω is the solid angle over which particles are accepted and t the duration of the exposure in seconds. This equation is derived assuming that the maximum distance a particle may traverse in the volume is much less than λ.

The value of dN obtained directly from scanning must be corrected for several forms of detection inefficiency.

3.1. *Detection Efficiency of Stars*

No attempt has been made to detect those stars with $N_h \leqslant 2$, since it is well known that area-scanning cannot hope to detect such stars efficiently. Instead a correction has been made by using the experimental data available on the interactions produced in nuclear emulsions by artificially accelerated protons. Winzeler *et al.* (1960) have published a N_h distribution for those stars found by 'along the track scanning' of 6·2 Bev protons. This distribution has been used to correct that found in this experiment. Figure 1 shows these distributions normalized for those stars with $N_h \geqslant 5$, since it appears that there has also been some loss of stars with $N_h = 3$ and 4 in this experiment. The correction factor derived for the loss of stars with $N_h < 5$ is $1 \cdot 56 \pm 0 \cdot 13$.

The validity of this procedure depends on the assumption that the N_h distribution is nearly independent of energy, which appears to be generally true for energies above 1 or 2 Bev. Furthermore, since the geomagnetic cut-off energy in this experiment was approximately 3·6 Bev for the protons, the median energy of these particles was about 5·7 Bev. Thus the majority of the primary protons had energies which are not too different from those of the artificially accelerated protons with which they are being compared.

Fig. 1

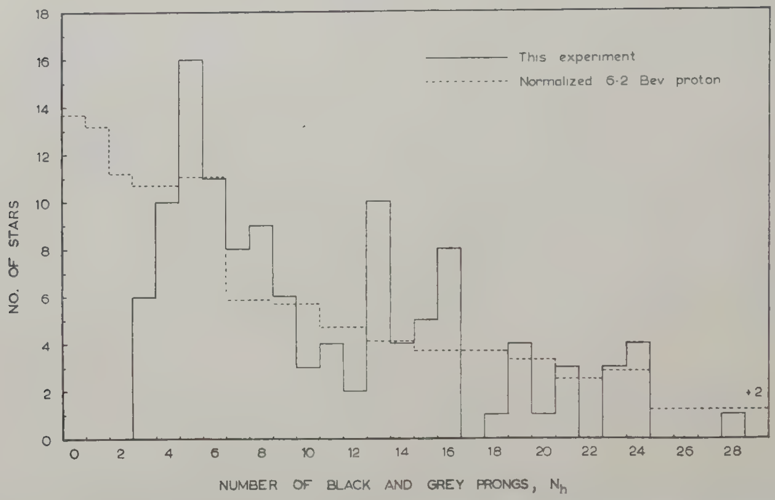

The N_h distribution observed in this experiment and that observed by Winzeler *et al.* (1960) on 6·2 BEV protons. These distributions are normalized for those stars with $N_h \geqslant 5$.

Fig. 2

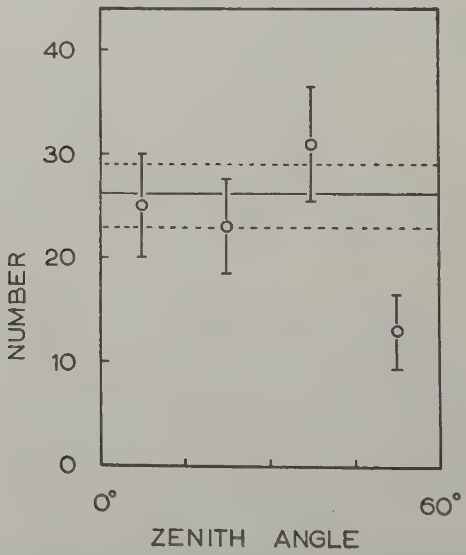

The zenith angle distributions of those tracks which could definitely be assumed to be due to primary particles. The data has been divided into four equal frequency intervals. The mean of the first three, together with its standard deviations are shown by the horizontal lines.

3.2. *Detection Efficiency for Primary Particles*

The tracks left by fast singly-charged particles are the most tenuous observable in nuclear emulsions and the most careful inspection is necessary to detect all such tracks associated with each star. Approximately one-third of all the stars were examined by two observers, and the good agreement between them suggests that both had very high efficiencies. However, such a comparison assumes that all tracks have an equal intrinsic probability of detection, and this may not be true. An alternative indication of the detection efficiency was supplied by studying the observed angular distribution of those particles which were assumed to be primary particles. It is reasonable to assume that the detection efficiency might be related to the zenith angle of the track, i.e. a particle dipping steeply in the emulsion might be more difficult to detect than one lying in the plane of the emulsion. The distribution of the space angles observed in this experiment is shown in fig. 2. It can be seen that if it is assumed that the incident particles are isotropically distributed there is a definite indication that particles with large space angles have been missed. To a first approximation these particles should be isotropically distributed and so a correction must be made for those missed. In this experiment, from a sample of 92 primary particles an additional 13·3 ± 4·7 were assumed to have been missed.

3.3. *Identification of Primary Particles*

When a star has more than one minimum track associated with it, it is not always clear which was produced by the primary particle. Thus it is necessary to consider each star in detail in an attempt to determine which track has the greatest probability of being due to the primary.

In an interaction of an energetic nucleon with an emulsion nucleus, the fast secondary particles are strongly collimated in the forward direction. As a result, in any particular star, the primary track may be taken as that which results in the least sum of the angles that the other minimum tracks make with the direction of motion of the assumed primary. In the majority of stars with three or more associated minimum tracks this condition is sufficient to determine the primary with a high degree of probability. However, in some cases no one track is clearly defined as being due to the primary.

For this reason those stars having a minimum track within the solid angle of acceptance, Ω, have been separated into seven groups. Sketch drawings of typical members of each group are shown in fig. 3.

(*a*) Stars with just one minimum track. Since any albedo of energetic neutral particles can be neglected, this minimum track has a high probability of being that due to the primary. In a sample of 100 stars, 18% were of this type.

(*b*) Stars with two minimum tracks, one of which is in the lower hemisphere. While either track could have been produced by the incident particle, there appears to be a much greater probability that the one in the upper hemisphere should be that due to the primary (see later). Frequency 19%.

(*c*) Stars with more than two minimum tracks, in which the only one in the upper hemisphere is clearly that due to the primary. Frequency 37%.

(*d*) As (*c*), but with two or more tracks in the upper hemisphere, only one of which is clearly due to the primary. Frequency 8%.

(*e*) As (*d*) but with no clear indication as to which track is due to the primary. These stars were given a weight depending on the number of tracks in the upper hemisphere within and outside Ω. Frequency 8%.

(*f*) Stars with more than two minimum tracks, in which one in the lower hemisphere is clearly produced by the primary. Frequency 5%.

(*g*) Stars with two or more minimum tracks, all in the upper hemisphere. These were given a weight as for (*e*). Frequency 5%.

Fig. 3

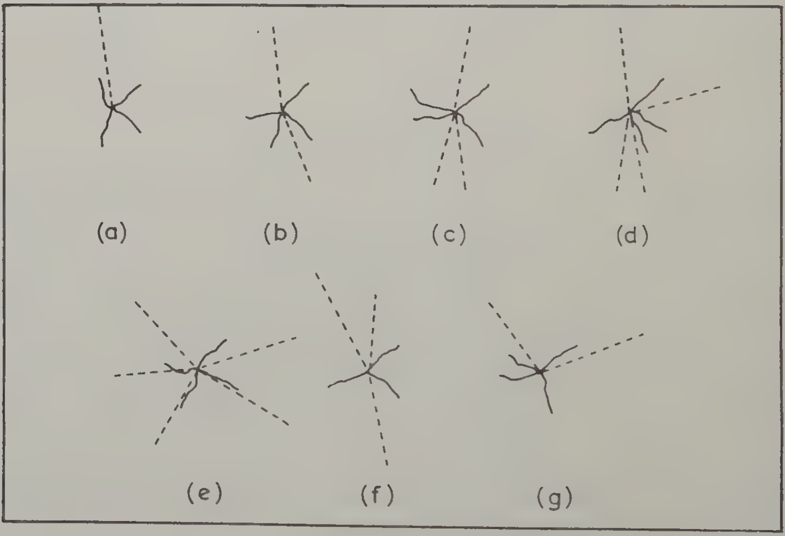

Sketch drawings of typical stars. Each star has $N_h = 4$.

Comparing groups (*c*) and (*d*) with group (*f*), it appears that only about 10% of the stars in groups (*b*) should have been produced by upward moving secondary particles. On a small sample of this sort, this is a negligible fraction. It could, of course, be further reduced by exposing a smaller stack of emulsions, so as to reduce the amount of local matter available to generate these particles.

§ 4. EXPERIMENTAL RESULTS

In scanning a volume of 1·47 cm^3, 101 stars were found which had primaries in the solid angle of acceptance and $N_h \geqslant 5$. To these were added 14·6 ± 5·1 stars to allow for the inefficiency of detecting primaries at large angles. The resulting 115·6 stars were multiplied by 1·56 ± 0·13, the correction factor for those stars with $N_h \leqslant 4$. Then, using eqn. (1), with $\lambda = 38{\cdot}2 \pm 1{\cdot}5$ cm, the value quoted by Winzeler *et al.* (1960), $\Omega = \pi$ steradians, and $t = 2{\cdot}07 \times 10^4$ sec, the time spent at ceiling altitude, $J(X) = 720 \pm 105$ protons/m^2 ster sec, where $J(X)$ was the flux of primary protons in the emulsion, and $X = 10$ g/cm^2 of residual matter.

§ 5. GROWTH CURVE OF PROTONS IN THE ATMOSPHERE

In order to extrapolate the flux value observed in the emulsions to the top of the atmosphere it is necessary to establish a growth curve for these particles. Furthermore, since in this experiment the emulsions were not re-orientated after they reached ceiling altitude it is essential to make a correction for those particles which entered while the emulsions were ascending and descending. For this purpose the growth curves must be known to appreciable depths in the atmosphere. It may be noticed that it is unnecessary to make a correction for those protons entering at sea level, since these will be closely collimated to the vertical, and it is unlikely that the stack would have been correctly orientated for them.

There appears to be little or no experimental evidence regarding the flux of energetic protons as a function of atmospheric depth, and it is therefore necessary to construct a growth curve from a theoretical model. The simple, and somewhat artificial one chosen here assumes that in a typical interaction of an energetic proton with an air nucleus the proton is generally not absorbed but merely degraded in energy. The energetic products of such an interaction consist mainly of π-mesons, which on the average take about one-third of the incoming energy (Zhdanov *et al.* 1960) and occasional knock-on protons. Thus the proton multiplicity, n, is greater than unity for a number of successive interactions. Eventually the protons are either absorbed, or their energies are reduced below that necessary to produce tracks of minimum ionization.

With these assumptions, if $J_p(x, \theta)$ is the flux of primary protons and protons produced by primary protons at a vertical depth x and zenith angle θ, and if J_0 is the flux of primary protons at the top of the atmosphere, then

$$J_p(x, 0) = J_0 \exp(-x/\lambda_p)\left[1 + \frac{n_1 x}{\lambda_p} + \frac{n_1 n_2 x^2}{2!\,\lambda_p{}^2} + \dots\right] = J_0 f_1(x) \qquad (2)$$

where λ_p is the interaction mean free path of protons in air, taken to be 100 g/cm^2, and $n_1, n_2, \dots$ are the multiplicities in the first, second, ... interactions.

In this experiment, where particles were accepted at zenith angles of up to 60°, the flux at any depth x is given by

$$\int J_p(x,\theta)\,d\omega = 2\pi x \int_x^{2x} \frac{J_p(y,0)}{y^2}\,dy$$

where $y = x/\cos\theta$ (Rossi 1952)

$$= 2\pi x \int_x^{2x} \frac{J_0 f_1(y)}{y^2}\,dy = \pi J_{pp}$$

which may be solved graphically.

Fig. 4

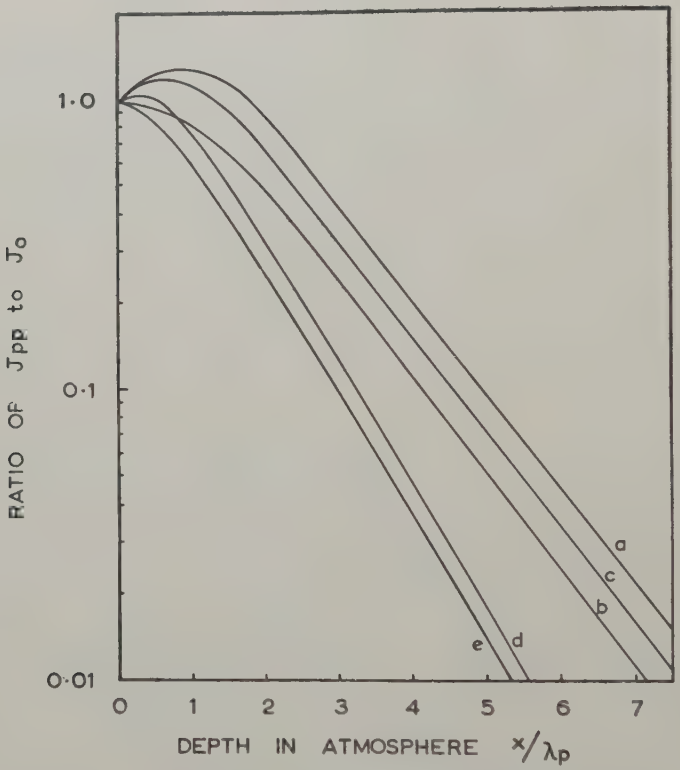

The variation of the ratio J_{pp}/J_0 with x.

A plot of the ratio J_{pp}/J_0 against x is shown in fig. 4 for various cases. (a), (b) and (c) assume a three-stage process, i.e. use the first three terms of eqn. (2), with $n_1 = n_2 = 1{\cdot}5$; $n_1 = n_2 = 1{\cdot}0$ and $n_1 = 1{\cdot}5$, $n_2 = 1{\cdot}0$, respectively. (d) and (e) assume a two-stage process, with $n_1 = 1{\cdot}5$ and $n_1 = 1{\cdot}0$ respectively.

It has been assumed that a three-stage process is more appropriate for protons above a cut-off energy of about 3·6 Bev, whereas a two-stage process applies for protons of lower energy. The only experimental justification for this appears to be the approximately correct prediction of the sea-level proton flux mentioned later. A more refined model would have to take account of the range of energies of the primary protons. The values of n are somewhat more justifiable, since 1·5 and 1·0 represent reasonable limits and the combination of these two values in assumption (c) appears to represent the best model for this experiment.

Approximately 50% of the nucleons in the primary cosmic radiation do not enter the atmosphere as free protons, but bound in nuclei. The median energy of these bound nucleons is approximately half that of the free ones, due to the influence of the geomagnetic field. For this reason it has been assumed that the protons released from these nuclei are capable of producing one fewer interaction than are the free protons before they are removed. For simplicity these bound nuclei have been assumed to enter only in the form of α-particles, and the primary α-particle flux has been taken to be one-quarter of the primary proton flux.

Thus, corresponding to a two-stage process for free protons

$$J_\alpha(x,0)=2J_{\alpha 0}\,\frac{\lambda_p}{\lambda_p-\lambda_\alpha}[\exp(-x/\lambda_p)-\exp(-x/\lambda_\alpha)]=J_{\alpha 0}f_2(x)$$

where λ_α is the interaction mean free path of α-particles in air, assumed to be half λ_p, and $J_{\alpha 0}$ is the assumed flux of α-particles at the top of the atmosphere.

So, as before

$$\pi J_{\alpha p}'=2\pi x\int_x^{2x}\frac{J_{\alpha 0}f_2(y)}{y^2}\,dy$$

where $J_{\alpha p}'$ is the flux of protons produced by α-particles in a two-stage process.

Similarly, in a three-stage process

$$J_\alpha(x,0)=2J_{\alpha 0}\frac{\lambda_p}{\lambda_p-\lambda_\alpha}\left[\exp(-x/\lambda_\alpha)\left(\frac{n_1\lambda_\alpha}{\lambda_p-\lambda_\alpha}-1\right)\right.$$
$$\left.+\exp(-x/\lambda_p)\left(1+\frac{n_1x}{\lambda_p}-\frac{n_1\lambda_\alpha}{\lambda_p-\lambda_\alpha}\right)\right]=J_{\alpha 0}f_3(x).$$

So, as before

$$\pi J_{\alpha p}''=2\pi x\int_x^{2x}\frac{J_{\alpha 0}f_3(y)}{y^2}\,dy.$$

Thus the total flux of protons, $J(x)$, at any depth x is given by

$$J(x)=J_{pp}+J_{\alpha p}.$$

Curves of the ratios $J_{\alpha p}/J_{\alpha 0}$ and $J(x)/J_0$ as a function of x are shown in figs. 5 and 6.

A *partial* test of the validity of this model is provided by comparing the flux predicted at sea level, i.e. $10\lambda_p$, with that measured experimentally. Mylroi and Wilson (1951) have measured a flux of 0·55 protons/m^2 ster sec at Manchester, England. This may be compared with the value of about 0·25 protons/m^2 ster sec predicted by models (d) and (e), which, because of the low cut-off energy over Manchester, should be the appropriate models. In view of the simplified nature of these models this agreement appears to be remarkably good.

Using the curves in fig. 6 it is possible to calculate the correction factor $f(t)$ for the ascent and descent of the balloon, as well as that for the overlying atmosphere during the level flight, $f(x)$. Values of $f(t)$ and $f(x)$ are shown in table 1, together with the resulting values of J_0, given by

$$J_0 = J(X) \,.\, f(t) \,.\, f(x),$$

where $J(X)$ is the flux measured in the emulsions (eqn. (1)).

Fig. 5

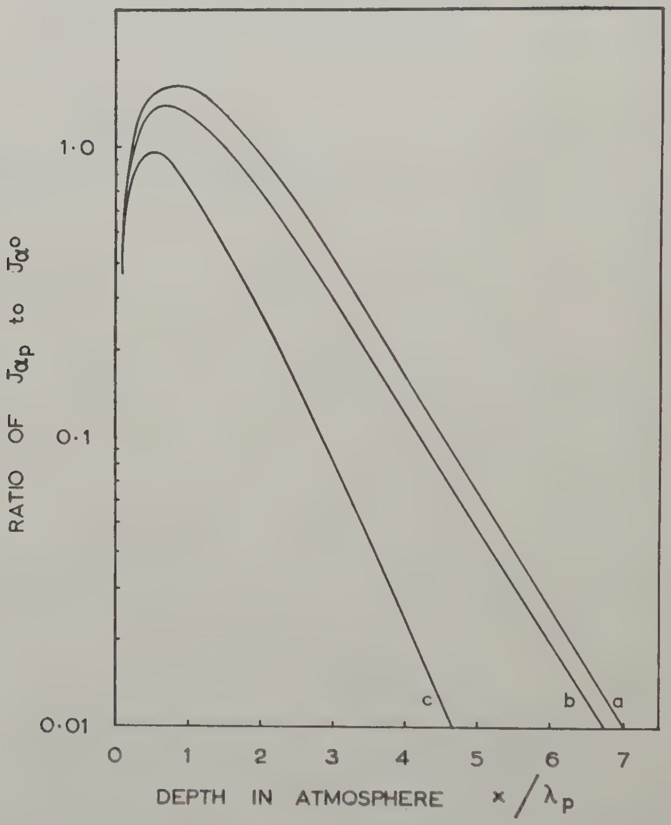

The variation of the ratio $J_{\alpha p} J_{\alpha 0}$ with x. Curves a and b are for a three-stage process with $n_1 = 1{\cdot}5$ and $1{\cdot}0$ respectively, while curve c is for a two-stage process.

Thus, $J(X)$ when corrected to the top of the atmosphere becomes, under the most plausible assumptions, model (c).

$$J_0 = 500 \pm 70 \text{ protons/m}^2 \text{ ster sec}$$

where the quoted error does not include the uncertainties in the extrapolation to the top of the atmosphere.

This value of J_0 may be compared with that of

$$590 \pm 50 \text{ protons/m}^2 \text{ ster sec}^\dagger$$

Fig. 6

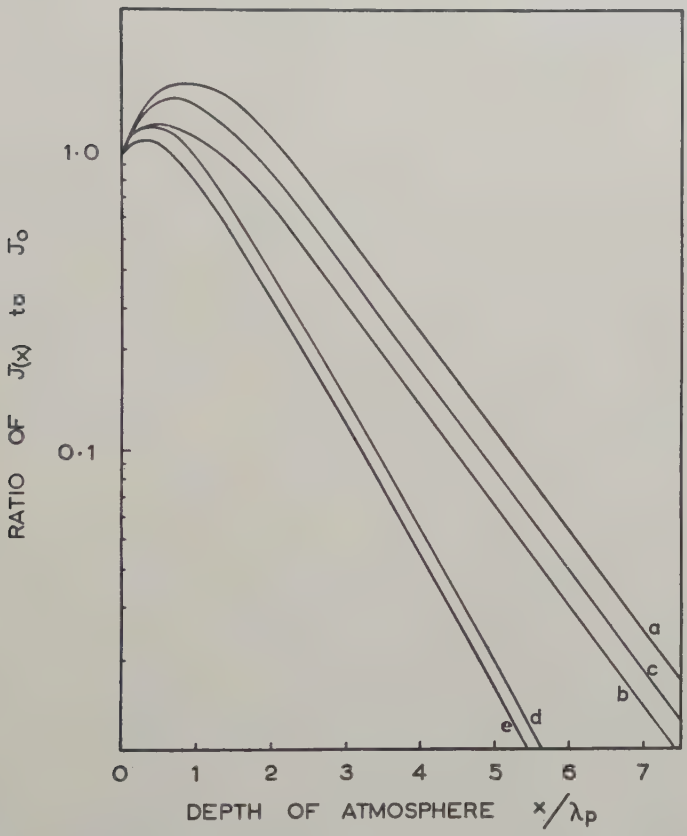

The variation of the ratio $J(x)/J_0$ with x.

Table 1. Correction Factors

Model	$f(t)$	$f(x)$	$f(t) \,.\, f(x)$	J_0 (protons/m^2 ster sec)
(*a*)	0·787	0·855	0·674	485 ± 70
(*b*)	0·829	0·910	0·753	540 ± 75
(*c*)	0·805	0·861	0·694	500 ± 70
(*d*)	0·850	0·905	0·769	555 ± 80
(*e*)	0·860	0·935	0·804	580 ± 85

---

† After correction for the re-entrant albedo of about 40 ± 10 particles/m^2 ster sec.

found by McDonald and Webber (1959) in a flight where the α-particles flux was almost precisely similar to that measured in this stack.

§ 6. Conclusions

The agreement between these two values of the proton flux appears reasonable, and suggests that there are no *serious* errors in either methods of determining these fluxes.

The fluxes of all the nucleonic components of the primary cosmic radiation have now been measured in the stack of emulsions used in this experiment. These flux values are shown in table 2.

Table 2. Fluxes of Nucleonic Components Measured in One Emulsion Stack

Component	Flux (particles/m² ster sec)	Reference
Protons	500 ± 70	This work
α-particles	89 ± 8	Waddington (1957 b)
$3 \leqslant Z \leqslant 5$ nuclei	$2 \cdot 3 \pm 0 \cdot 4$	Waddington (1957 a)
$6 \leqslant Z \leqslant 9$ nuclei	$6 \cdot 1 \pm 0 \cdot 6$	,,
$Z \geqslant 10$ nuclei	$2 \cdot 5 \pm 0 \cdot 3$	,,

With this demonstration of the feasibility of measuring proton fluxes with nuclear emulsions it should now be possible to use available experimental material to investigate the behaviour of this component of the primary cosmic radiation in some detail. However, it must be noted that emulsion experiments are still not able to give any information on the individual energies of these protons. Also that the accuracy of this method is limited by the uncertainties of the correction for secondary protons. This can be reduced by using small stacks exposed at great altitudes which have been re-orientated after reaching ceiling altitude. Under these conditions, and with the better data from machine experiments that should soon be available, accuracies of better than ±10% should be easily obtainable.

Acknowledgments

The author is grateful to Professor C. F. Powell, F.R.S., for the facilities of his laboratory, and to Mrs. W M. Dyer for her valuable assistance with the scanning and examination of the stars.

References

Fowler, P. H., and Waddington, C. J., 1956, *Phil. Mag.*, **1**, 637.
Hillier, R. R., and Rajopadhye, V. Y., 1958, *Nuovo Cim.*, Suppl., **8**, 520.
McDonald, F. B., 1956, *Phys. Rev.*, **104**, 1723.

McDonald, F. B., and Webber, W. R., 1959, *Phys. Rev.*, **115,** 194.
Mylroi, M. G., and Wilson, J. G., 1951, *Proc. phys. Soc., Lond.* A, **64,** 404.
Rajopadhye, V. Y., and Waddington, C. J., 1958, *Phil. Mag.*, **3,** 25.
Rossi, B., 1952, *High Energy Particles* (Prentice-Hall Inc.), p. 440.
Waddington, C. J., 1957 a, *Phil. Mag.*, **2,** 1059; 1957 b, *Nuovo Cim.*, **6,** 748.
Winzeler, H., Klaiber, B., Koch, W., Nikolić, M., and Schneeberger, M., 1960, *Nuovo Cim.*, **17,** 8.
Zhdanov, G. B., Markov, P. K., Strel'tsov, V. N., Iret'yakov, M. I., Cheng P'U-Ying, and Shafranova, M. G., 1960, *J. exp. theor. Phys.* (*USSR*), **37,** 611 or *J.E.T.P.*, **10,** 433.

X-ray Evidence for Segregation of Solute to Stacking Faults in a Copper–Aluminium Alloy†

By R. W. Cahn and R. G. Davies
Department of Physical Metallurgy, The University, Birmingham 15, England

[Received May 27, 1960]

Abstract

A study was made of the intensity of scattering of monochromatic x-rays at small angles from a copper-base solid solution containing 15 at. % aluminium. The intensity of scattering from a rolled foil was found to increase after heating at 150–250°c, a temperature range in which the alloy hardens, and there is little or no recrystallization. This increase is attributed to segregation of aluminium to the ribbons of stacking fault between partial dislocations. Various confirmatory tests were performed to check the validity of this conclusion.

§ 1. Introduction

1.1. *Anneal Hardening*

The present experiment was designed as an adjunct to a study (Chinowsky and Cahn 1961) of the *anneal hardening* of α-aluminium bronze. The cold-worked alloy becomes harder if it is annealed below the recrystallization temperature ; α-brass and some other solid solutions behave similarly. Hasiguti (1955) proposed the term ‘ anneal hardening ’ to denote this phenomenon. Two alternative theories have been put forward to account for it :

(1) The alloy may possess short-range order which is partly destroyed by deformation, and re-established by annealing. *If* the locking is in part determined by short-range order, this process can account for anneal hardening.

(2) The dislocations formed during deformation may become locked by a segregation of solute atoms to the broad ribbons of stacking fault that separate the dissociated partial dislocations in an alloy of low stacking-fault energy. Such segregation has been postulated by Suzuki (1952). It can come about during an anneal following deformation, and cause the alloy to become harder.

It is known (Borie 1958, private communication, Houska and Averbach 1959, Davies and Cahn 1961) that α-Cu/Al is liable to extensive short-range order and that this decreases with increase of the annealing temperature. Yet a sample quenched from 600°c, and accordingly almost disordered, does not harden on tempering at 200°c (a treatment which re-establishes

---

† Communicated by the Authors.

the order). For this, and other reasons, explanation (2) is more attractive, especially since α-brass and α-Cu/Al are known to have very low stacking-fault energies. More detailed discussion of the interpretation of anneal hardening will be found in a forthcoming paper by Chinowsky and Cahn.

1.2. *Small-angle X-ray Scattering due to Local Solute Segregation*

If 'Suzuki segregation' does occur, it should be possible to detect it by means of small-angle scattering of x-rays. When a solid solution is freshly cold-worked, the new dislocations will be devoid of segregate. On subsequent annealing below the recrystallization temperature, solute will go to the stacking faults, which thus come to resemble GP zones in an age-hardened alloy. The local perturbations in the initially uniform electron density, resulting from a local concentration of solute, will in both cases give rise to an additional scattering of x-rays at small angles (Guinier and Fournet 1955). In the case of age-hardening alloys, such as Al/Ag and Al/Cu, this prediction has been amply confirmed (e.g. Walker and Guinier 1953). It was the purpose of the present experiment to look for this effect in an anneal-hardening alloy.

The following conditions must be met if such an experiment is to have any hope of success :

(1) The alloy must have solvent and solute of widely differing atomic numbers Z, since for a given dislocation density and a given degree of segregation, the intensity of small-angle scattering will be proportional to $(f_{\text{solvent}} - f_{\text{solute}})^2$, where the f's are atomic scattering factors. For small scattering angles, this $= (Z_{\text{solvent}} - Z_{\text{solute}})^2$.

(2) The alloy must have a high dislocation density so that there are enough scattering centres for the predicted effect to be detectable.

(3) The alloy must have a low specific stacking-fault energy, so that the ribbons of stacking fault between partial dislocations shall be wide; this again will enhance the scattered intensity.

A copper-base alloy containing 15 at. % aluminium, cold-rolled to 50% reduction or more, satisfies all these conditions and was chosen as experimental material. The low stacking-fault energy and consequently large total area of stacking-fault ribbon in filings of Cu/Al alloys was confirmed by Paterson's x-ray line shift method (Christian and Spreadborough 1957, Smallman and Westmacott 1957). Moreover, an analysis of the x-ray line broadening from Cu/Al filings, due to Guseva and Babareko (1959) yielded results closely similar to those obtained by Warren and Warekois (1955) in analysing line-widths from α-brass filings, and which they were able to interpret in terms of a faulted domain structure.

Since the present work was completed, Nakajima (1959) has published a note in which he claims to have detected an increment of small-angle x-ray scattering due to Suzuki segregation in a Cu/Ni alloy. It will be surprising if this claim can be substantiated, since the alloy used by Nakajima signally fails to satisfy condition (1), above.

1.3. *Double Bragg Reflection Mechanism*

A complication arises from the small-angle x-ray scattering which is observed directly after deformation, and which is predominantly due to repeated Bragg reflections from pairs of subgrains in the deformed structure (Beeman and Webb 1959, Neynaber *et al.* 1959, Fricke and Gerold 1958, 1959, Atkinson 1958). However, by careful comparative measurements of scattered intensity before and after heat treatment, this effect can be allowed for, and this has been done in the present experiments.

§ 2. EXPERIMENTAL METHODS

The small-angle scattering apparatus used is shown diagrammatically in fig. 1. A beam of copper Kα radiation, monochromated by an asymmetrically cut bent quartz crystal, passed through the alloy foil before being blocked by a beam stop at the focus. The alloy foil was set in a holder so arranged that the same area could be irradiated after the foil had been temporarily removed for heat treatment. The intensity of the beam was continuously monitored by a Geiger counter which measured the intensity of the (311) line diffracted by a very thin cold-rolled foil of aluminium, set in the beam behind the quartz crystal.

Fig. 1

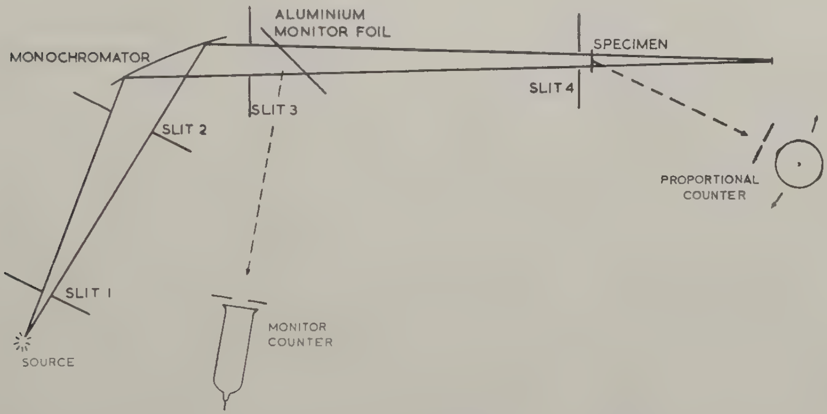

Schematic diagram of small-angle scattering apparatus.

The intensity scattered by alloy foil was measured by means of a proportional counter (20th Century Electronics Ltd.) set behind a slit on a rotating arm. Used in conjunction with a pulse amplifier and a pulse height analyser, this counter had a cosmic-ray background of only 4 counts/min. This rather elaborate counting equipment was essential since the scattered intensity was so small that a typical Geiger counter background of about 1 count/sec would have been of the same order as the 'signal'. Fluctuations of the beam intensity were allowed for by accumulating a fixed number of monitor counts, and counting the pulses arriving at the proportional counter during the corresponding period.

The high purity alloy used, containing 15 at. % aluminium, was rolled and carefully homogenized, reduced by further cold rolling to about 100 μ thickness, annealed and rolled down to 50 μ, and finally thinned uniformly to a thickness of about 15 μ by means of chemical polishing†.

§ 3. RESULTS

Figure 2 shows a scattering curve obtained from a cold-rolled alloy foil, using in front of the proportional counter a narrow slit that subtended 10′ of arc at the sample. The results in fig. 2 have been corrected for background count and for residual parasitic scattering, which was appreciable for scattering angles less than 1·8°. This curve is typical

Fig. 2

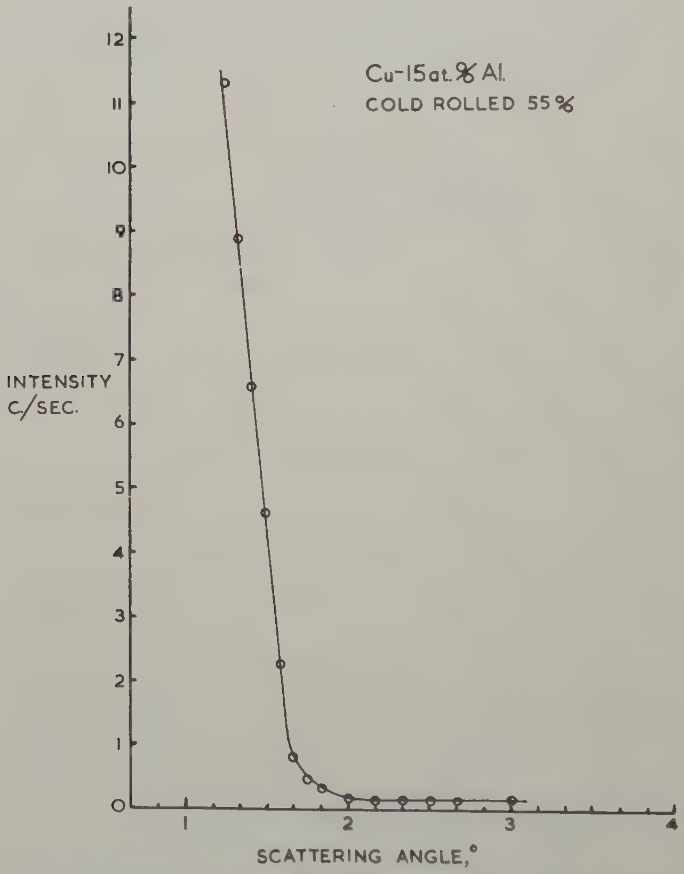

Small-angle scattering curve from an alloy foil rolled to 50% reduction. Correction for background count and parasitic scattering has been made.

---

† The polishing bath, used at 70°c, contained 50% glacial acetic acid, 30% conc. nitric acid, 10% conc. hydrochloric acid and 10% conc. orthophosphoric acid.

of those obtained for a rather weakly deformed metal (Neynaber *et al.* 1959, Webb and Beeman 1959).

The sample was then annealed progressively at 250°c and the scattered intensities at several angles between 1° and 1·7° were measured after each anneal. The intensities progressively increased, until after 13 hours' annealing all had increased by about 20%. This increase was statistically significant in spite of the fairly large probable error in counting.

Further experiments were now made using a larger slit at the counter, subtending 30′ of arc at the sample, and keeping to a fixed scattering angle of 2°, measured at the slit centre. In this way a higher statistical accuracy could be achieved. The intensities quoted hereafter are uncorrected for parasitic scattering (which was very weak at 2° scattering angle).

A foil was reduced 70% in thickness by rolling, cut in half and chemically thinned, and the intensity of x-ray scattering from each piece was measured. In each case this was about 470 counts during the period needed by the monitor to accumulate 30 000 counts. Most of this intensity was presumably due to double Bragg scattering. The pieces were then annealed in stages, one at 200°c and the other at 250°c, and the scattering from the same areas of the foils measured after each anneal. Figure 3 shows the results. The points denote the *increase* in the scattered intensity in terms of counts per 30 000 monitor counts ; the vertical line through each point represents the probable statistical error. The solid curves represent results for the isothermal hardening of a similar massive alloy sample†, plotted with a suitably normalized ordinate scale so that the hardness and intensity plots should concide as nearly as possible.

Figure 3 shows the following : (1) The intensity scattered from both samples increases significantly, the maximum increase from both samples being about 15%. (2) There is a very rapid initial rise in the scattering power ; an anneal of less than one minute at 200°c suffices to produce an 8% increase in intensity. (3) At 250°c, recrystallization begins after some hours for the degree of deformation used, and the scattered intensity then falls steeply. (4) The hardness increase at each stage is proportional to the increase of scattering power.

Attempts were made, using the point-focusing small-angle camera described by Atkinson (1958) (kindly loaned by Dr. P. B. Hirsch) to record the small-angle scattering photographically so as to study its distribution in azimuth, but these attempts failed because of the low intensity available.

§ 4. Discussion

The results shown in fig. 3 might in principle be associated with any of the following changes in the specimen during anneal hardening :

(1) The re-establishment of short-range order.

(2) Growth of subgrains in the alloy and subsequent modification of the intensity of double Bragg reflection.

(3) Suzuki segregation of solute to the stacking faults.

---

† Results due to Mr. S. Chinowsky.

Alternative (1) is improbable since increase of order will diminish the weak Laue monotonic scattering (Warren and Averbach 1953) and should thus actually lead to a slight decrease of small angle scattering. As a check, a piece of the alloy foil was annealed at 600°c and quenched, which recrystallized and disordered it, and the scattered intensity at 2° was measured. The foil was then annealed 17 hours at 150°c, which suffices to produce substantial short-range order (Davies and Cahn 1961). The scattering intensity after this treatment had not changed, within the statistical counting error of ±3%. Alternative (1) is thus ruled out.

Fig. 3

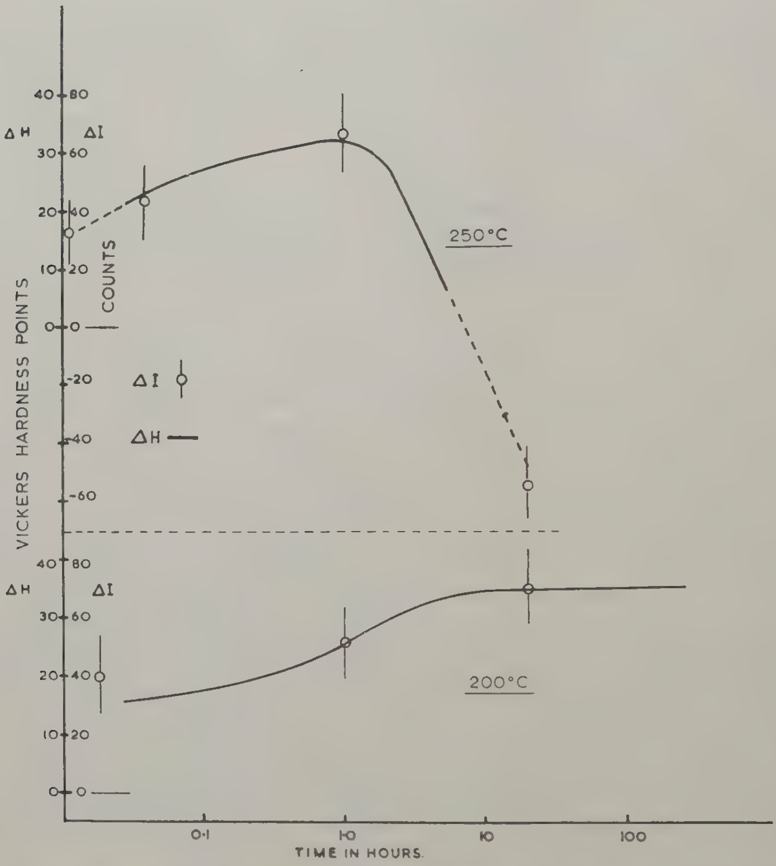

Isothermal kinetics, at 200 and 250°c, of the *change* in scattered x-ray intensity at 2°, and of the Vickers pyramid hardness.
X-ray results: Cu/15 at. % Al alloy, rolled 70%. Ordinate shows *increase* in counts per 30 000 monitor counts, above initial value of 470 counts.
Hardness results: Cu/14 at. % Al alloy, rolled 75%. Ordinate shows *increase* in Vickers hardness number.

Alternative (2) can also be excluded fairly definitively. The theory of double Bragg reflection (Webb and Beeman 1959) shows that the total scattered flux due to the double reflection mechanism is proportional to the inverse square of the mean subgrain diameter ; subgrain growth should thus lead to a rapid *reduction* of intensity scattered at small angles. This has indeed been confirmed by Reizman (1959), who studied the change, on annealing, of small-angle scattering from rolled copper foil. The resultant subgrain growth led to a *steady* decrease of the small-angle scattering ; there was no sign of a transient increase. We carried out an experiment to confirm this. Copper and alloy foils, rolled to approximately the same reduction, were each annealed 17 hours at 150°c, which is enough to harden the alloy considerably but not to cause any recrystallization in either the alloy or the copper. The x-ray scattering at 2° from the unannealed alloy was 927 ± 20 counts per 63 000 monitor counts, and it was 1076 ± 20 counts after heat treatment—an increase of 16%. The corresponding counts for the copper were 791 and 784 respectively ; the difference is not significant. A further anneal of 20 hours at 250°c caused substantial recrystallization of the copper and the count *fell* to 625. There is no reason why the double Bragg reflection process should be differently affected by heat treatment in the case of the alloy than in the case of copper.

There is therefore no cause, theoretical or experimental, to suppose that subgrain growth might in itself cause an increase of the small-angle scattering from the alloy.

§ 5. CONCLUSION

Having eliminated the alternatives, we are left with the conclusion that the increased small-angle scattering from the cold worked alloy, resulting from heat treatment at 150–250°c, is due to a segregation of solute to the stacking faults.

The present results are merely indicative; more detailed exploration is desirable of the isothermal kinetics of the change of the scattered intensity, of its dependence on the degree of deformation, on the state of polarization of the scattered x-rays, etc., but the low x-ray intensity available from our equipment precluded such a systematic study. In particular, experiments with rolled single crystals could show whether the distribution in azimuth of the scattered intensity was consistent with the presence of lamellar segregates parallel to the octahedral slip planes.

ACKNOWLEDGMENTS

We are indebted to Professor G. V. Raynor for his encouragement and providing laboratory facilities, to the D.S.I.R. for a grant to one of us (R.G.D.), and to Dr. P. B. Hirsch for a useful discussion and the loan of apparatus.

References

Atkinson, H. H., 1958, *Phil. Mag.*, **3**, 476.

Chinowsky, S., and Cahn, R. W., 1961, *J. Inst. Metals* (to be published).

Christian, J. W., and Spreadborough, J., 1957, *Proc. phys. Soc. Lond.* B, **70**, 1151.

Davies, R. G., and Cahn, R. W., 1961, *Phil. Mag.* (to be published).

Fricke, H., and Gerold, V., 1958, *Naturwissenschaften*, **45**, 287; 1959, *J. appl. Phys.*, **30**, 661.

Guinier, A., and Fournet, G., 1955, *Small Angle Scattering of X-rays* (New York : Wiley).

Guseva, L. N., and Babareko, A. A., 1959, *Soviet Physics Doklady*, **4**, 129.

Hasiguti, R. R., 1955, *J. Jap. Inst. Metals*, **19**, 103.

Houska, C. R., and Averbach, B. L., 1959, *J. appl. Phys.*, **31**, 1525.

Nakajima, K., 1959, *J. phys. Soc. Japan*, **4**, 1825.

Neynaber, R. H., Brammer, W. G., and Beeman, W. W., 1959, *J. appl. Phys.*, **30**, 656.

Reizman, F., 1959, Ph.D. Thesis, University of Wisconsin (*Dissertation Abstracts* 1959, **20**, 1049).

Smallman, R. E., and Westmacott, K. H., 1957, *Phil. Mag.*, **2**, 669.

Suzuki, H., 1952, *Sci. Rep. Res. Insts Tôhoku Univ.*, A, **4**, 455.

Walker, C. B., and Guinier, A., 1953, *Acta Met.*, **1**, 568.

Warren, B. E., and Averbach, B. L., 1953, *Modern Research Techniques in Physical Metallurgy* (Cleveland : Amer. Soc. for Metals), 95.

Warren, B. E., and Warekois, E. R., 1955, *Acta Met.*, **3**, 473.

Webb, M. B., and Beeman, W. W., 1959, *Acta Met.*, **7**, 203.

A Magnetic Study of Precipitation in a Gold–Cobalt Alloy†

By P. Gaunt
Department of Physics, University of Sheffield, Sheffield, 10

[Received May 26, 1960]

Abstract

The precipitation kinetics of a gold 1·5%, by weight, cobalt alloy have been followed by measuring the saturation magnetization of the precipitated cobalt and the results are compared with current theories. Marked differences were found between the ageing curves of air and water-quenched specimens. The remanent magnetization, coercive force and field to reduce remanence to zero of aged specimens have been measured and the results are discussed in terms of the single magnetic domain model. The magnetic properties are compared with those of the gold nickel system and the conclusion is reached that the dominant contribution to the anisotropy in the gold cobalt system is due to particle shape. In an appendix the remanence curve and coercivity for a random array of single domain ferromagnetic particles having a linear distribution of anisotropies have been calculated and shown to predict the main features of the observed results.

§ 1. Introduction

The magnetic properties of fine ferromagnetic precipitates in non-ferromagnetic matrices have been studied extensively in recent years and interpreted in terms of single domain theory. Much attention has been paid to the copper–cobalt system (Bate *et al.* 1955, Becker 1958, Mitui 1958), where the cobalt-rich precipitate is thought to form as the face-centred cubic allotrope (Rodbell 1958). Unfortunately the analogous system, copper–nickel, shows complete miscibility of the two constituents so that no comparison between the behaviour of the two face-centred cubic ferromagnetic metals in a copper matrix is possible. However, the gold–nickel and gold–cobalt systems both show limited solid solubility. The lattice parameters of the face-centred cubic forms of cobalt and nickel are very similar (3·545 kX and 3·517 kX), thus leading to similar disregistries between precipitate and gold matrix (lattice parameter 4·704 kX), of about 12%. The spontaneous magnetizations of cobalt and nickel do, however, differ considerably (164 and 58 e.m.u. per g), and any difference in magnetic properties between the two systems will be in large measure due to this. In particular, the theory of Stoner and Wohlfarth (1948) predicts that if the coercivity of an array of small single domain particles is due to shape anisotropy then it will be proportional to the spontaneous magnetization of the material. On the other hand, contributions due to crystalline and magnetostriction anisotropy will be inversely proportional to the spontaneous magnetization. A comparison of the two systems, with different spontaneous magnetizations but similar metallographic properties, should therefore indicate the dominant contribution to the observed anisotropy. The gold–nickel system has been investigated by Lothian *et al.* (1958), and results on the gold–cobalt system are presented in the present paper.

---

† Communicated by Professor W. Sucksmith.

According to the phase diagram of Raub and Walter (1950) it is possible to retain 1·5%, by weight, of cobalt in solid solution in gold at 960°c, and then to form a ferromagnetic precipitate, containing about 99% of cobalt, by ageing at a lower temperature. The allotropic transition from the face-centred cubic to the hexagonal close-packed form takes place at a temperature less than 500°c in cobalt–gold alloys containing 99% cobalt (Köster and Horn 1952). If, therefore, ageing is carried out at 500°c or above, the equilibrium precipitate will have a face-centred cubic structure.

§ 2. Preparation of Specimens

A gold–cobalt alloy containing 1·52%, by weight, of cobalt was made by melting the constituents together in an argon arc furnace on a water-cooled copper hearth. The alloy was then cast into a rod, about 0·4 cm in diameter and 5 cm long, by melting *in vacuo* in an evacuated silica tube using an induction furnace. This rod was homogenized, *in vacuo*, for 36 hours at 960°c before disc-shaped specimens about 0·1 cm thick were cut from the rod.

The specimens were annealed for 5 min at 960°c in evacuated silica capsules, and quenched to room temperature before ageing at 565°c. Some specimens were water-quenched, by withdrawing the silica capsules rapidly from the furnace and breaking them under cold water; others were quenched more slowly by allowing them to cool in air without breaking the tube.

§ 3. Measurements of Saturation Magnetization

Magnetization at fields greater than 4000 oe was measured using a Sucksmith ring balance (Sucksmith 1929 and 1939).

The magnetization of a quenched unaged specimen was proportional to field at room temperature but showed a tendency towards saturation at liquid nitrogen temperature. Quenched specimens showed no remanent magnetization or coercive force.

After ageing for 3 min the magnetization curve did not extrapolate through the origin, there was a remanent magnetization, and a coercive force of 900 oe was required to reduce the magnetization to zero.

In order to determine the saturation moment of the ferromagnetic precipitate a correction was made for the paramagnetism of the matrix solid solution by subtracting the small magnetization of the quenched specimen from that of the aged ferromagnetic specimen at each measuring field. The saturation magnetization was then determined from a linear extrapolation against the reciprocal of the measuring field.

The increase in saturation magnetization with ageing time for water- and air-quenched alloys is shown in fig. 1. The maximum value of the saturation moment was $1{\cdot}72 \pm 0{\cdot}02$ e.m.u./g which compares with the $1{\cdot}8 \pm 0{\cdot}1$ e.m.u./g predicted for this alloy from the data of Raub and Walter (1950).

Fig. 1

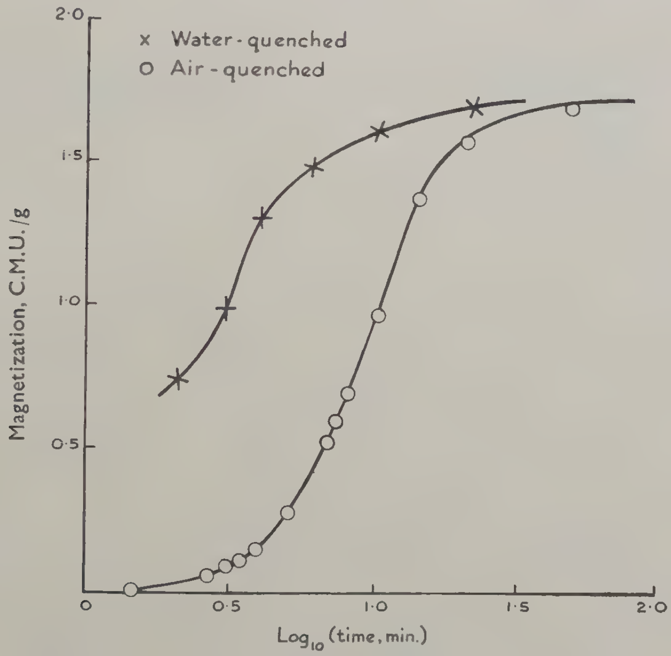

Variation of saturation magnetization with ageing time.

The initial rate of precipitation in water-quenched specimens was much greater than in air-quenched specimens. This is almost certainly due to there being a greater number of nucleation sites in the water-quenched alloys where the faster quench will retain the vacancies produced at the annealing temperature of 960°C.

§ 4. Remanent Magnetization

The remanent magnetization after the application of a field of 17 000 oe was measured using a torsion balance as described by Bate *et al.* (1955). The ratio of the remanent magnetization to the saturation magnetization was determined for 29 specimens including both air- and water-quenched specimens. There was no significant change in this ratio with ageing times from 1·5 to 50 min, the mean value of the ratio being 0·52, the standard deviation among the specimens being 0·05. The ratio of remanent to saturation magnetization is expected to be $\frac{1}{2}$ for a random array of single domain precipitate particles having predominantly uniaxial anisotropy (Wolhfarth 1955).

Complete remanence curves were plotted for a few specimens using the torsion balance. After ageing the specimen possesses zero magnetization, the individual particle moments lying along easy directions of magnetization. On applying and removing a small field, H, the magnetization of particles of low anisotropy is reversed and the specimen is left with a remanent magnetization $I_r(H)$. Further increase of H increases $I_r(H)$ until a saturation remanence, $I_r(\infty)$, is reached where all the particles have a component of magnetization parallel to the direction of the applied field. If a reverse field is now applied the remanent magnetization, $I_d(H)$, decreases to zero at H_r and to saturation remanence in the reverse direction at still higher fields.

Fig. 2

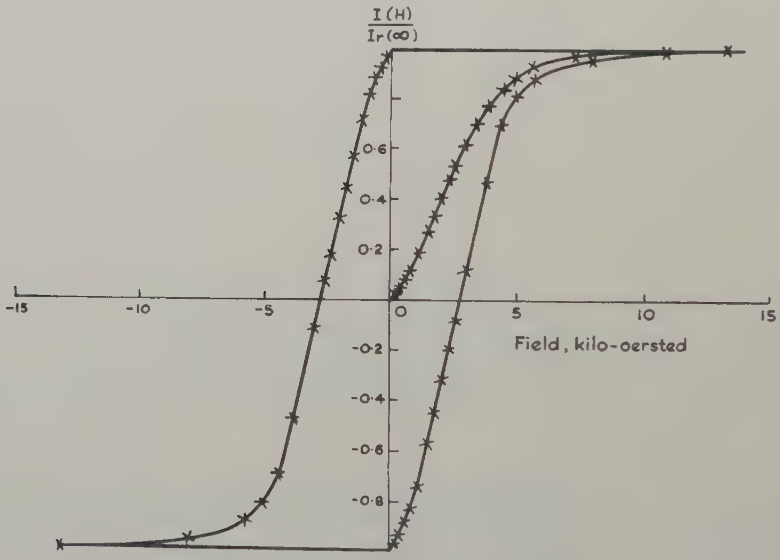

Remanence curve for a water-quenched specimen aged for 7 min.

A complete remanence curve for a water-quenched specimen, aged for 7 min, is shown in fig. 2. A field of more than 10 000 oe was required to produce saturation remanence indicating that the specimen must have contained particles with intrinsic coercivities as high as 10 000 oe.

('Intrinsic coercivity' of a particle is used to indicate the coercivity the particle would exhibit if the direction of lowest magnetic anisotropy energy were parallel to the field.) It was of interest to compare these results with an expression of Wohlfarth (1958) which gives:

Fig. 3

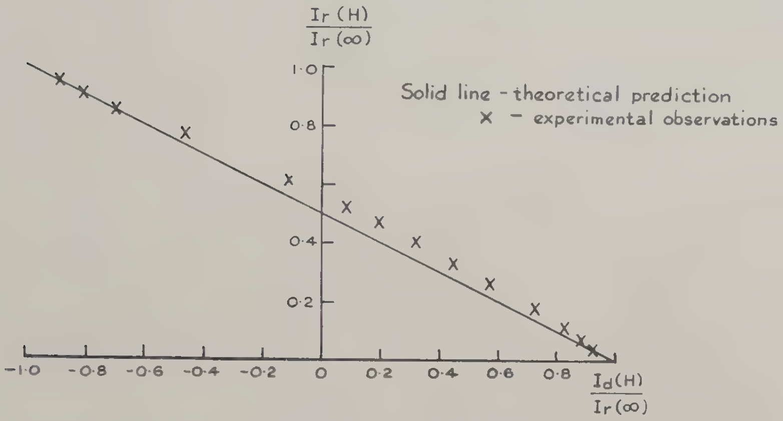

Relationship between initial remanence, $I_r(H)$, and demagnetizing remanence, $I_d(H)$.

Fig. 4

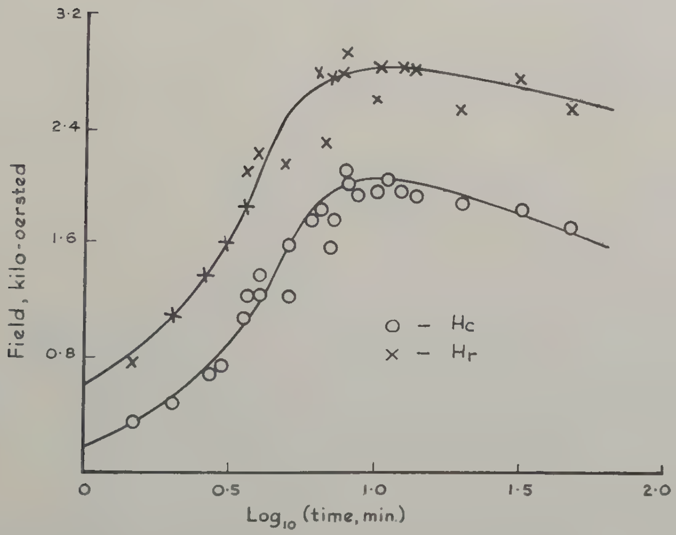

Variation of coercivity and remanence coercivity with ageing time for air-quenched specimens.

$$I_d(H) = I_r(\infty) - 2I_r(H).$$

This formula is easily proved for any array of non-interacting single domain particles of uniaxial anisotropy. In fig. 3, $I_d(H)$ is plotted against $I_r(H)$ showing a marked deviation from the ideal. The deviation may be due to the fact that the particles are not strictly uniaxial but possess mixed uniaxial and cubic anisotropies.

Fig. 5

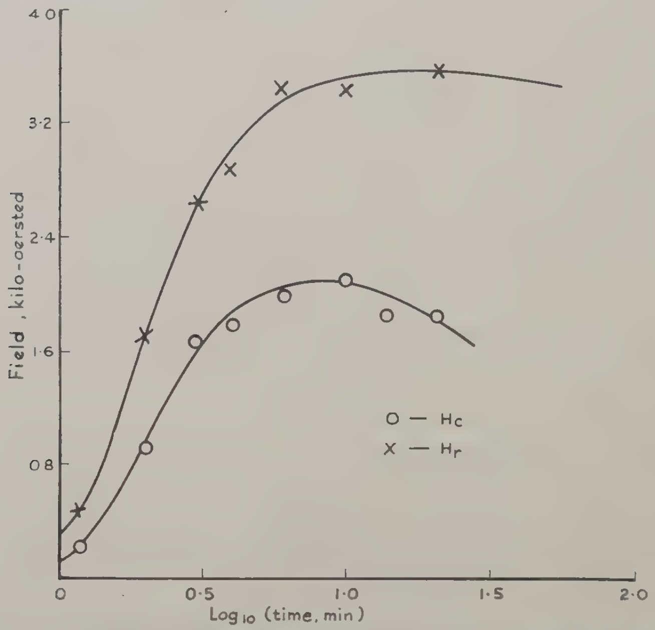

Variation of coercivity and remanence coercivity with ageing time for water-quenched specimens.

§ 5. COERCIVE FORCE AND FIELD TO REDUCE REMANENCE TO ZERO

Coercive forces greater than 900 oe were measured using the Sucksmith ring balance; forces less than 900 oe were determined with the torsion balance. The field to reduce remanence to zero, H_r, was also determined with the aid of the torsion balance. The variation of the two fields with ageing time in air-quenched specimens is shown in fig. 4. The maximum coercive force of 2050 ± 50 oe was attained after about 10 min ageing; the maximum H_r of 2800 oe being reached after about the same time. The ratio of the two fields was thus about 1·36 after 10 min ageing. For a random array of uniaxial single domain particles of uniform anisotropy this ratio should be 1·09 (Wohlfarth 1958); a ratio of 1·36 indicating a range of particle anisotropy of about the same order as observed by Lothian *et al.* (1958) in Au–Ni alloys. The change of the fields with time is consistent with the growth of single domain particles whose shape anisotropy increases as their size increases. The fall in the fields after the optimum ageing time is reached is then due to the onset of multidomain behaviour when the particles reach a critical size. Water-quenched specimens behave similarly, as shown in fig. 5, reaching a maximum H_c of 2050 oe after about 10 min ageing but attaining a higher value of H_r at 3500 oe. The ratio H_r/H_c is thus about 1·7, indicating a greater range of particle anisotropy than is found in air-quenched specimens.

The coercivity of the aged specimens was increased by *c.* 600 oe on cooling to liquid nitrogen temperature. A graph of H_c against temperature for a water-quenched specimen aged for 10 min is shown in fig. 6.

Fig. 6

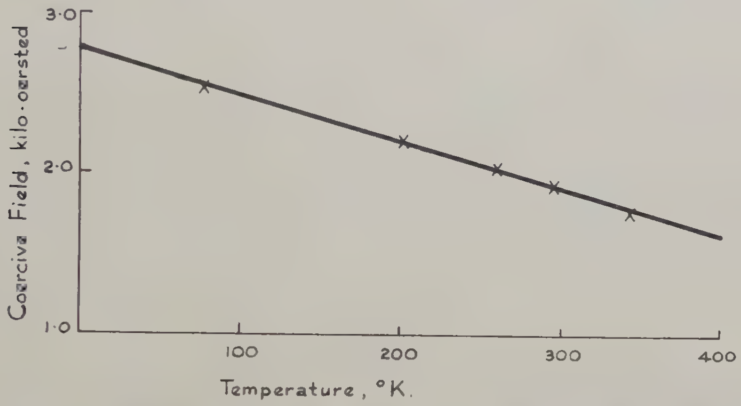

Variation of coercivity with temperature for a water-quenched specimen aged for 10 min.

§ 6. Effect of Strain

A preliminary experiment indicated that the aged alloys behaved in a similar way to Au–Ni alloys (Lothian *et al.* 1958); that is, the coercivity is greatest perpendicular to the axis in a drawing experiment and parallel to the axis in a compression experiment. Thus the coercivity of an air-quenched Au–Co specimen increased from 1880 oe to 2200 oe parallel to the axis and decreased to 1510 oe perpendicular to the axis after a compressive strain of 6%. This contrasts with the observations of Livingston and Becker (1958) in a Cu–Co alloy where they observed enhanced coercivity parallel to a tension axis, and the increase in anisotropy energy produced by the strain was consistent, up to 20% strain, with homogeneous deformation of matrix and precipitate. The contrast in behaviour may be due to the high disregistry of 12% between precipitate and matrix in the Au–Ni and Au–Co systems compared with the 1·7% disregistry in the Cu–Co system: if the disregistry is small the particles will remain coherent with the matrix and dislocations will pass easily through the particles thus making shape deformation of the particles possible. If disregistry is large the particles quickly lose their coherence and the passage of dislocations is impeded by the particles.

§ 7. X-RAY MEASUREMENTS

Debye–Scherrer photographs of quenched and aged needle specimens were taken using copper radiation. No extra lines due to the precipitate phase were detected. The quenched specimens gave sharp reflections at all Bragg angles, and the lattice parameter of the solid solution was 4·0535 kX. Ageing an air-quenched specimen for 2·75 min caused the high-angle reflections to blur toward the low Bragg angle side of the photograph; this blurring becoming more pronounced with further ageing. After 18 min, precipitation was almost complete, and after 2500 min ageing the high angle lines were again sharp, the matrix having a lattice parameter of 4·0658 kX. The water-quenched specimens behaved similarly. The films show that as precipitate particles begin to form the matrix far from the particles is left unchanged in composition and a cobalt-depleted region surrounds the particle. This suggests that almost as soon as precipitation begins the full lattice disregistry of 12% must be accommodated at the matrix particle interface. As ageing proceeds the concentration gradient in the matrix becomes smaller until the cobalt concentration reaches its equilibrium value and the high angle diffraction lines become sharp.

§ 8. DISCUSSION

8.1. *Saturation Magnetization*

The saturation magnetization of the specimen is a direct measure of the amount of precipitate and it was of interest to compare the kinetics of the precipitation process with a formula of Zener (1949) which gives the fraction precipitated as:

$$\alpha = 1 - \exp\left[-\left(\frac{t}{\tau}\right)^m\right]$$

where τ and m are constants and t is the ageing time. Thus if $\log\log(\sigma_\infty/\sigma_\infty - \sigma_t)$ is plotted against $\log t$, where σ_∞ is the saturation magnetization after complete ageing and σ_t is the saturation magnetization after time t, it should give a straight line of slope m. In fig. 7 this function is plotted for both air- and water-quenched specimens. The graphs show that the increase of saturation magnetization with time (in minutes), can be well represented up to 60% precipitation, in air-quenched specimens by:

$$\sigma_t = 1{\cdot}72[1 - \exp - (t/7{\cdot}50)^{2{\cdot}46}]$$

and in water-quenched specimens by

$$\sigma_t = 1{\cdot}72[1 - \exp - (t/1{\cdot}66)^{1{\cdot}23}].$$

Ham (1958) has treated the problem of precipitation from a supersaturated solid solution in a rigorous way and has shown that a formula of the type derived by Zener should be a good approximation for the first 50% of the precipitation process. He has further shown that the exponent m will be 1·5 for any shape of particle in a diffusion-limited process, where surface and strain-energy effects are negligible, and in which the inter-particle separation is about ten times the particle diameter. The eccentricity of the particles in such a process will remain constant after a short initial transient. For situations where a surface reaction is dominant m tends to 3, while for diffusion-limited growth where the initial particle volume is greater than one-tenth the final volume, m will be between 1·0 and 1·5.

Fig. 7

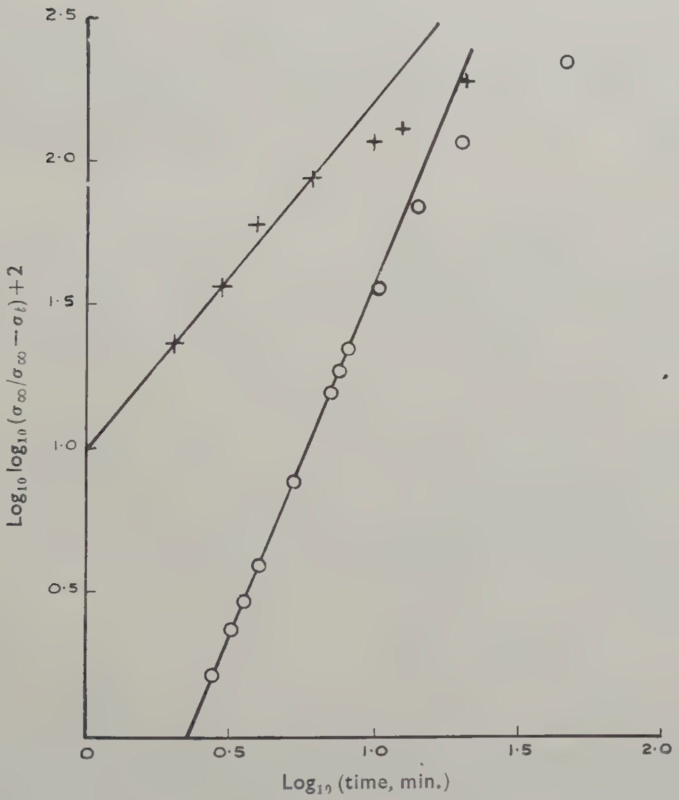

Logarithmic plot of saturation magnetization against ageing time.

For the air-quenched specimens $m > 1{\cdot}5$, indicating that precipitation cannot be purely diffusion-limited and surface and strain-energy effects are probably important. In the water-quenched specimens $m < 1{\cdot}5$ so that the nature of the nuclei formed by rapid quenching must be such that the coherency strains are more easily accommodated and large particles are formed in the initial transient process.

8.2. *Coercivity and Field to reduce Remanence to Zero*

The two fields H_c and H_r reached their maximum values after about 10 min ageing in both air- and water-quenched specimens. The optimum value of H_r was, however, significantly higher in water-quenched specimens although H_c was approximately the same for air- and water-quenched specimens. The larger value of H_r/H_c in water-quenched specimens indicates that they contain a wider range of particle anisotropies than the air-quenched specimens. This must be associated with the fact that as the optimum ageing time is reached in water-quenched specimens the supersaturation is small, precipitation being about 93% complete, but in air-quenched specimens it is larger since precipitation is only 55% complete. According to Nabarro (1940) a low supersaturation favours increasing eccentricity of the growing particle. Thus the shape anisotropy and hence the intrinsic coercivity of particles growing from a solution of low supersaturation will reach higher limiting values before the size of the particles allows domain walls to form. The range of anisotropies will therefore be wider in water-quenched specimens since particles of high anisotropy are favoured.

A graph of H_c against temperature, for a water-quenched alloy aged for 10 min is shown in fig. 6. The variation of H_c is linear over the range 77°K–380°K. Stacey (1959 a) has derived a formula relating the magnetic energy of a single domain particle to its volume v, and the coercivity of a random array H_c:

$$E = vH_cI_0 + kT \ln C\tau$$

where I_0 is the spontaneous magnetization per cm³ of the particle, k is Boltzmann's constant, T is the absolute temperature, τ is the time taken to measure H_c, and C is a frequency factor whose maximum value at room temperature is given as $6 \times 10^{12}\,\mathrm{sec}^{-1}$ by Stacey (1959 b). Thus assuming I_0 is independent of T over the range considered:

$$\frac{dE}{dT} = vI_0 \frac{dH_c}{dT} + k \ln C\tau + k/T .$$

(The factor k/T arises because $C \propto T$, Stacey 1949 b.) If now the magnetic energy is due to shape anisotropy alone then dE/dT is zero and the variation in coercivity arises only from temperature dependent fluctuations of the particle magnetization. Hence

$$v = -\frac{k(\ln C\tau + 1/T)}{I_0\, dH_c/dT} .$$

From the graph $dH_c/dT = -2{\cdot}87$ oe/c deg and taking τ as 1 sec (this is not critical), gives $v = 1{\cdot}010 \times 10^{-18}\,\mathrm{cm}^3$ and hence a particle radius of order 62 Å. This calculation gives an average size for the particles contributing to the observed coercivity. If the direction of low shape anisotropy is associated with a direction of low crystalline anisotropy energy, the contribution to dH_c/dT due to cubic crystalline anisotropy will be $-0{\cdot}66$ (Bean *et al.* 1959).

Thus

$$\frac{dE}{dT} = -0{\cdot}66 v I_0;$$

therefore

$$v = -\frac{k(\ln C\tau + 1/T)}{I_0(dH_c/dT + 0{\cdot}66)},$$

leading to a slightly larger value for v as $1{\cdot}311 \times 10^{-18}\,\mathrm{cm}^3$ and radius 68 Å.

The air-quenched specimens show approximately the same slope so that the particle radii are not appreciably different in air- and water-quenched specimens aged for 10 min. The value obtained above for the particle radius agrees with that found by Becker (1957) for the onset of ferromagnetic properties in copper–cobalt alloys.

8.3. *Remanent Magnetization*

The remanent magnetization of annealed specimens after the application of a field of 17 000 oe was half the saturation magnetization. This suggests that the precipitate particles have predominantly uniaxial magnetic anisotropy (Wohlfarth 1955). In fig. 2 the remanent magnetization was plotted against the applied field for a water-quenched specimen whose mean coercivity was 1570 oe and field to reduce remanence to zero was 2700 oe. The saturation remanence was not reached until a field greater than 10 000 oe was applied, showing that particles having intrinsic coercivities of this order were present. In the appendix a remanence curve for a simple linear distribution of anisotropies is calculated and compared with the experimental curve and using the linear distribution giving the best fit with the experimental remanence curve a value of H_c was calculated as 1440 oe.

The saturation remanence for an air-quenched specimen, for which H_r was 2500 oe and H_c 1850 oe, was reached at about 7000 oe, thus showing that a narrower range of anisotropies was present in these specimens.

The intrinsic coercive force of a prolate spheroid is given by $(N_b - N_a)I_0$ where N_b is the demagnetizing factor along the short axis and N_a along the long axis (Stoner and Wohlfarth 1948). The maximum value, for an infinitely long spheroid is thus given by $2\pi I_0$. For cobalt this value is 8962 oe but a spheroid of axial ratio 10 reaches 98% of this maximum value. A maximum contribution to the particle coercivity of $2K/I_0$ is possible due to crystalline anisotropy. If the precipitate is face-centred cubic this adds a maximum contribution of *c.* 1400 oe making a total of *c.* 10 400 oe. The observed maximum intrinsic coercivity can therefore be explained in terms of a cubic precipitate showing no magnetostriction effects. A magnetostriction contribution to the coercivity is possible if the precipitate experiences a uniaxial stress. This will only occur if the precipitate remains partially coherent with the matrix. In the gold–cobalt system the disregistry is about 12% so that the precipitate will begin to break away from the matrix when the particle diameter reaches 100/12 atom spacings since a dislocation can then be introduced to relieve the strain between the two lattices. Thus the precipitate will begin to break away from the matrix when its radius becomes greater than 30 Å, which is about half the lower limit of particle size to show ferromagnetic, rather than super-paramagnetic, behaviour (Becker 1957). The precipitate will therefore have started to break away after the optimum annealing time and there is not likely to be a large magnetostriction contribution to the magnetic anisotropy.

As shown in fig. 6, the remanence curve shows a marked deviation from the relation proposed by Wohlfarth (1958), relating the remanence $I_r(H)$ gained by the initial application of a field to an aged specimen and the remanence $I_d(H)$ remaining after the application of a demagnetizing field to a previously saturated specimen.

The relation will only be strictly obeyed for an array of perfectly uniaxial particles rather than the particles of mixed cubic and uniaxial anisotropy which are formed in practice. It is possible for particles in their initial state to have magnetization vectors not lying in the uniaxial direction but in one of the cubic easy directions.

The application and removal of a suitable field will turn these vectors into the easier uniaxial directions. On applying a demagnetizing field the cubic easy directions may no longer be available as remanence positions since there is no suitable field which will bring the magnetization vector close enough to the cubic axis for it to rest there on removal of the field ; the critical angle for reversal of the vector in the uniaxial direction being greater than the critical angle for return to the cubic direction. This means that the demagnetizing mode of the remanence curve will be harder than the initial magnetizing mode so that the remanence coercivity predicted from the initial magnetizing curve will be less than that found by demagnetization.

8.4. *Comparison with Au–Ni*

The maximum coercivity found by Lothian *et al.* (1958) in aged Au–Ni alloys was 325 oe. It was, however, observed that the coercivity increased if the alloy cross section was reduced by cold drawing. Thus Robinson (1957) found that after as little as 13% reduction the coercivity both parallel and perpendicular to the drawing axis increased to about 600 oe. The coercivity perpendicular to the axis was, however, greater than that parallel to the axis and further reduction increases this difference, the coercivity parallel to the axis decreasing. The initial rapid increase in coercivity can be explained if it is supposed that the elongated particles are in tension, thus giving a negative contribution to the coercivity. A small amount of cold work is then sufficient to relieve this tension as dislocations cross the particles. Orientation effects will, however, tend to make the coercivity parallel to the drawing axis less than that perpendicular to the axis.

The maximum coercivity observed in the Au–Co system was 2050 oe and in the compression experiment the coercivity parallel to the compression axis increased but perpendicular to the axis it decreased. An initial overall increase in coercivity, both parallel and perpendicular to the axis, was not therefore observed but the orientation effect was strong. Thus it appears that the magnetostriction contribution is much less than the shape anisotropy contribution in Au–Co. It is to be expected that the magnetostriction contribution will be smaller for cobalt than for nickel alloys since it is inversely proportional to the spontaneous magnetization.

The fact that the maximum observed coercivity in the cobalt alloys is bigger than in the nickel alloys suggests that the shape anisotropy term is dominant since this is proportional to the spontaneous magnetization. If it is further supposed that the particle shape is determined mainly by metallographic factors the constant of proportionality will be roughly the same for both systems because of the similarity of cobalt and nickel in structure and atomic size. With these assumptions it is possible to compare the two systems and estimate the magnetostriction contribution, to the anisotropy using the relation :

$$H_c = AI_s + \frac{B}{I_s} + \frac{C}{I_s}$$

where I_s is the spontaneous magnetization and A, B, and C are constants determining the shape, magnetostriction and magnetocrystalline contributions. Thus assuming A and B to be the same for both the nickel and cobalt systems and allowing 700 oe and 100 oe for the magnetocrystalline contributions in cobalt and nickel, gives :

$$1350 = 1400A + \frac{B}{1400} \text{ for cobalt,}$$

$$225 = 500A + \frac{B}{500} \text{ for nickel.}$$

This gives $A = 1{\cdot}04$ and $B = -1{\cdot}47 \times 10^5$.

The negative value of B is expected for nickel and cobalt in tension since the magnetostriction coefficient is negative for nickel in all directions and for cobalt in $\langle 111 \rangle$ directions. Using the formula of Stoner and Wohlfarth (1948) for the magnetostriction contribution from a random array of particles :

$$H_c = 0{\cdot}479\,\frac{3\lambda b}{I_s}$$

where λ is the magnetostriction coefficient and b is the uniaxial tension, gives a value of about $3{\cdot}0 \times 10^{10}$ dynes/cm² for b.

This is small compared with the upper limit for b suggested by Stoner and Wohlfarth of about $2 \times 10''$ dynes/cm².

The value of A gives a mean value for the axial ratio of the elongated particles of approximately 1·6.

A suggested breakdown of the anisotropy contributions for the two systems is shown in the table :

	H_c	Shape	Crystalline	Magnetostriction
Co	2050	1455	700	-105
Ni	325	520	100	-295

Thus relaxation of tension, by slight cold working, in the Au–Ni alloys increases the coercivity to 620 oe which agrees with experiment. In the Au–Co alloy the increase in coercivity, due to relaxation of tension by cold work, is swamped by the changes due to the orientation of the much larger shape and crystalline anisotropy contributions.

ACKNOWLEDGMENTS

The author wishes to thank Professor W. Sucksmith for his help and encouragement in this work.

APPENDIX

REMANENT MAGNETIZATION AND COERCIVITY FOR A LINEAR DISTRIBUTION OF PARTICLE ANISOTROPY

Current theories based on the single magnetic domain hypothesis generally deal with arrays of particles of uniform anisotropy. In practice, and especially in heterogeneous alloys, a wide range of anisotropies is present and theories based on a single anisotropy must prove inadequate. The simplest distribution of anisotropies which can be considered, and whose parameters can be easily varied, is a linear distribution with an upper and lower cut-off value. Such an approximation is sufficiently good to indicate the main features of an array containing a range of anisotropies and in particular to show how the ratio H_r/H_c depends on this range.

For a linear distribution of particle anisotropy the volume of precipitate, dv, whose intrinsic coercive force lies between H_0 and (H_0+dH_0) is given by :

$$dv = A dH_0 \text{ for values of } H_0 \text{ between } H_1 \text{ and } H_2$$

where A is a constant and H_1 and H_2 are the lower and upper cut-off values of H_0. Such a distribution, with suitably chosen values of H_1 and H_2, gives quite a good approximation to the results obtained in the present work and shows how the ratio H_r/H_c varies with the range of anisotropies present.

Remanent Magnetization

The remanence $dI_r(H)$ for a random array of particles of intrinsic coercivity H_0 can be tabulated from the data of Stoner and Wohlfarth (1948) using the method of Wohlfarth (1955). This gives the remanence on first applying a field H to a completely random array and the field H_r is that which produces a remanence of half the maximum value.

Thus :

$$dI_r(H)=Af(H/H_0)dH_0\ ;$$

therefore

$$\frac{dI_r(H)}{H}=Af(h)d\left(\frac{1}{h}\right)$$

where $h=H/H_0$; therefore

$$\frac{I_r(H)}{H}=A\int_{1/h=H_1/H}^{1/h=H_2/H} f(h)d(1/h). \qquad (1)$$

Fig. 8

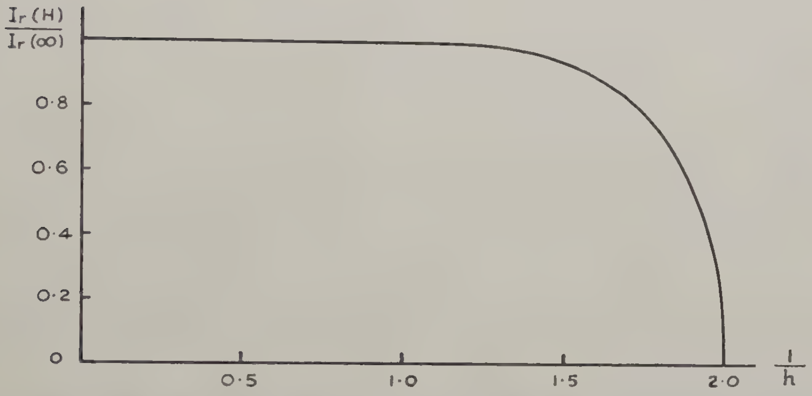

Variation of reduced initial remanence with reciprocal of reduced field for a random array of uniform anisotropy.

In fig. 8, $f(h)$ is plotted against $1/h$ and can be used to evaluate the integral of eqn. (1) for any particular value of H. When $H=H_2$ all the particles have turned toward the field direction and eqn. (1) becomes:

$$\frac{I_r(\infty)}{H_2}=A\int_{1/h=H_1/H}^{1/h=1} f(h)d(1/h)=A\,[1-H_1/H_2].$$

Equation (1) can therefore be re-written as :

$$\frac{I_r(H)}{I_r(\infty)}=\frac{H}{H_2-H_1}\int_{1/h=H_1/H}^{1/h=H_2/H} f(h)\,d(1/h) \qquad (2)$$

The field H_r is that for which $I_r(H)/I_r(\infty)=0{\cdot}5$; therefore

$$0{\cdot}5=\frac{H_r}{H_2-H_1}\{1{\cdot}855-(H_1/H_r)\}\text{ for }H_1/H_r\leqslant 1,\ (H_2/H_r)\geqslant 2.$$

Hence $H_r=0{\cdot}269\ (H_2+H_1)$ for $H_1/H_r\leqslant 1$, $H_2/H_r\geqslant 2$.

The values of H_r obtained experimentally from the initial and demagnetizing branches of the remanence curve were not the same ; the value from the demagnetizing branch being the greater. In fig. 9, therefore, the experimental value of $I_d(H)/I_r(\infty)$ from fig. 2 is compared with that for a linear array of anisotropies with $H_1=500$ and $H_2=9530$ using the relation of Wohlfarth (1958) :

Fig. 9

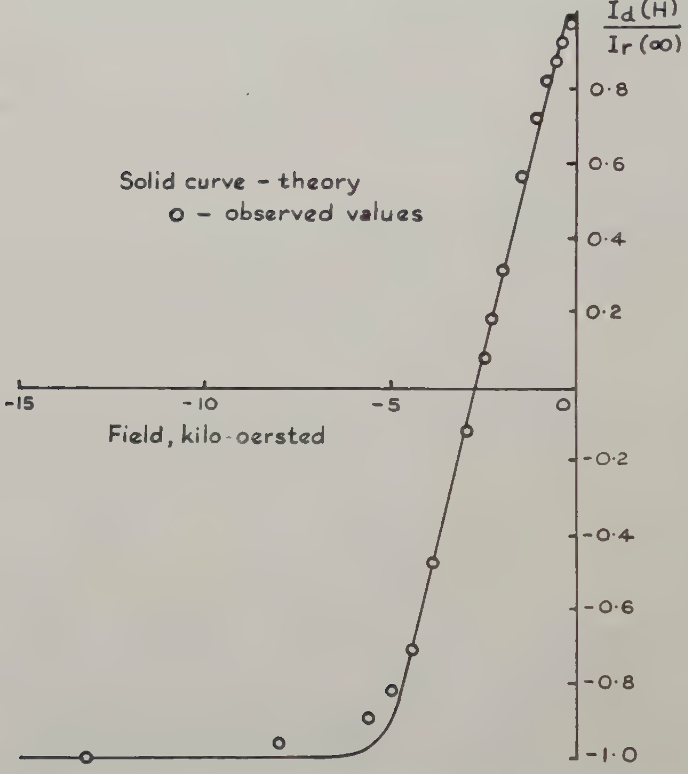

Comparison of demagnetizing remanence curve, for a linear anisotropy array, with observed values for a water-quenched specimen aged for 7 min.

$$I_d(H)=I_r(\infty)-2I_r(H)$$

to calculate $I_d(H)$. The theoretical curve has been chosen to fit at H_r and as closely as possible elsewhere. The uniform anisotropy distribution fits least well at the higher fields indicating that the true distribution contains fewer particles of anisotropy less than H_2 than is implied by the linear distribution.

Coercivity for a Linear Array

Stoner and Wohlfarth (1948) have tabulated the reduced magnetization curve for a random array of particles of intrinsic coercivity H_0. Thus by a similar argument to the above, for a linear anistropy distribution :

$$\frac{I(H)}{I(\infty)}=\frac{H}{H_2-H_1}\int_{1/h=H_1/H}^{1/h=H_2/H} g(h)\,d(1/h) \quad . \quad . \quad . \quad . \quad . \quad (3)$$

where $I(H)$ is the intensity of magnetization for the demagnetizing branch of the curve. The reduced magnetization, $g(h)$, for a random array of particles of uniform anisotropy is plotted against $1/h$. the reciprocal of the reduced field, in fig. 10. The coercive field is a function of H_1 and H_2 and is that field for which the integrand of eqn. (3) is zero. It can be represented to an accuracy of better than 1% by :

Fig. 10

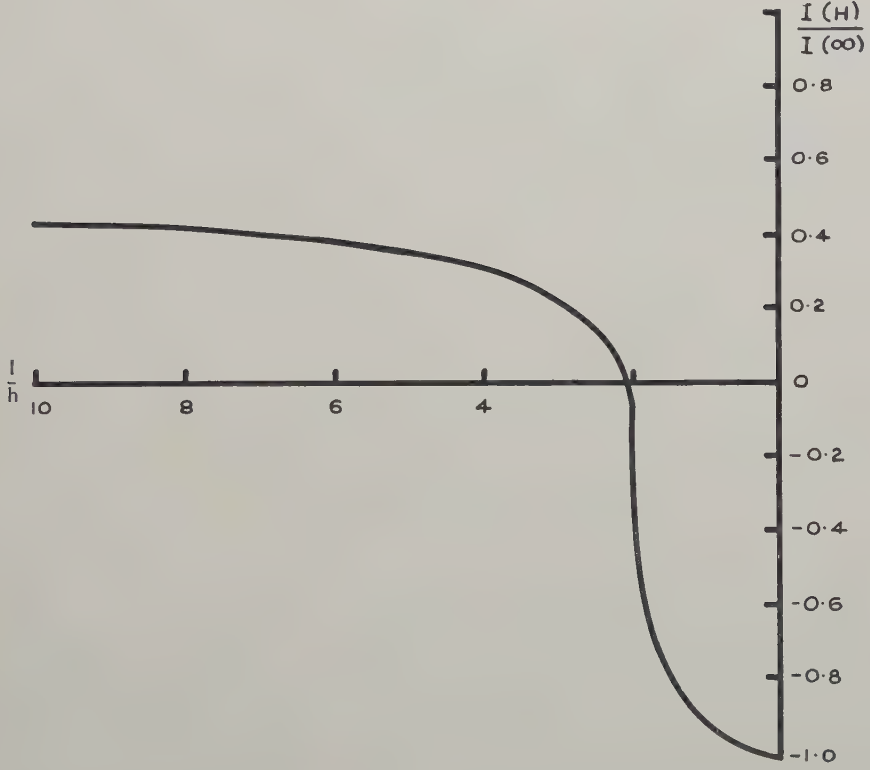

Variation of reduced magnetization, along demagnetizing branch, with reciprocal of reduced field for a random array of uniform anisotropy.

$$H_c=0{\cdot}133H_2\{1+2{\cdot}5(H_1/H_2)\}\ ;$$

further

$$H_r=0{\cdot}269\,H_2(1+H_1/H_2) \text{ for } H_1/H_2<1,\ H_2/H_r>2\ ;$$

therefore

$$H_r/H_c=2{\cdot}02\frac{1+H_1/H_2}{1+2{\cdot}5H_1/H_2}.$$

This formula is valid for values of H_r/H_c up to 0·37 when H_1/H_r becomes equal to one. For values of H_1/H_r greater than one H_r has to be calculated using fig. 8 to determine the appropriate integrand. In fig. 11 the ratio H_r/H_c is plotted against all possible values of H_1/H_2.

Fig. 11

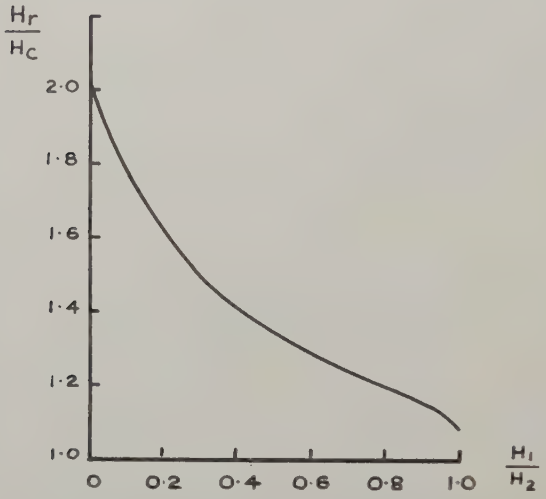

Variation of H_r/H_c with ratio of minimum to maximum anisotropy field in a linear anisotropy distribution.

For the water-quenched specimen considered above the observed values of H_r and H_c were 2700 and 1570 oe, so that H_r/H_c was 1·72. For the best fitted remanence curve the suggested value for H_1/H_2 of 0·0524 gives a value for H_r/H_c of 1·88 and for H_c of 1440 oe. Better agreement could doubtless be obtained by adopting a more realistic anisotropy distribution but the present approximation is sufficiently good to show the main features to be expected from an array of ferromagnetic particles having a range of anisotropies.

The calculations suggest that 2·02 will be the maximum possible value of H_r/H_c for such an array. Values of H_r/H_c greater than this could be produced in alloys containing a large proportion of super-paramagnetic material of zero coercivity. Thus almost all the values of H_r/H_c observed by Lothian *et al.* (1958), in Cu–Co alloys, were greater than 10 indicating a large super-paramagnetic contribution. However, in Au–Ni alloys and in the present work H_r/H_c was always less than 2, indicating that almost all the precipitate was in ferromagnetic form.

REFERENCES

BATE, G., SCHOFIELD, D., and SUCKSMITH, W., 1955, *Phil. Mag.*, **46,** 621.

BEAN, C. P., LIVINGSTON, J. D., and RODBELL, O. S., 1959, *J. Phys. Radium*, **20,** 298.

BECKER, J. J., 1957, *Trans. Amer. Inst. min.* (*metall.*) *Engrs*, **209,** 59; 1958, *Ibid.*, **212,** 138.

HAM, F. S., 1958, *J. Phys. Chem. Solids*, **6,** 335.

KOSTER, W., and HORN, E., 1952, *Z. Met.*, **43,** 333.

LIVINGSTON, J. D., and BECKER, J. J., 1958, *Trans. Amer. Inst. min.* (*metall.*) *Engrs*, **212,** 316.

LOTHIAN, B. W., ROBINSON, A. C., and SUCKSMITH, W., 1958, *Phil. Mag.*, **3,** 999.

MITUI, T., 1958, *J. phys. Soc. Japan*, **13,** 549.

RAUB, E., and WALTER, P., 1950, *Z. Met.*, **41,** 234.

ROBINSON, A. C., 1958, Thesis, University of Sheffield.

RODBELL, D. S., 1958, *J. appl. Phys.*, **29,** 311.

STACEY, F. D., 1959 a, *Proc. phys. Soc. Lond.*, **73,** 517; 1959 b, *Ibid.*, **73,** 136.

STONER, E. C., and WOHLFARTH, E. P., 1948, *Phil. Trans.* A, **240,** 599.

SUCKSMITH, W., 1929, *Phil. Mag.*, **8,** 158; 1939, *Proc. roy Soc.* A, **170,** 551.

WOHLFARTH, E. P., 1955, *Research*, **8,** S42; 1958, *J. appl. Phys.*, **29,** 595.

ZENER, C., 1949, *J. appl. Phys.*, **20,** 950.

Movement of Point Defects During Fatigue of Aluminium Crystals†

By E. Roberts and R. W. K. Honeycombe
Department of Metallurgy, University of Sheffield

[Received May 27, 1960]

Abstract

The dynamic stress–strain behaviour of aluminium crystals fatigued in a push–pull machine at 13 cycles/second is outlined. Room temperature interruptions to tests carried out at −196°c, −78°c and 20°c resulted in a transitory hardening which is attributed to the movement of point defects to dislocations.

A study has been made of the behaviour of 99·99% aluminium single crystals fatigued in a push–pull machine at 13 cycles/second. The stress pulse was fed to the X-plates of an oscilloscope, while the strain was measured by a capacitance strain gauge connected to the Y-plates so that a dynamic hysteresis loop was obtained continuously during a fatigue test (fig. 1, Pl. 146). In this way the dynamic hardening of the crystals could be studied over a wide range of fatigue conditions.

In tests carried out at room temperature, the width of the hysteresis loop (dynamic plastic strain) obtained at a given alternating stress gradually decreased (fig. 1 (*a*), (*b*) and (*c*)) in the way observed for much lower frequencies by Thompson *et al.* (1955). The maximum hardening occurred within the first 5% of the fatigue life, and a steady state was reached after about 15–20% (fig. 1 (*c*)). However, in tests carried out at −78°c and −196°c, no cyclic hardening whatsoever was detected, the loop width remaining at a steady value for large numbers of cycles (> 200 000 cycles).

In these low temperature tests, it was found that intermediate resting at room temperature resulted in a hardening of the crystals when fatigue was resumed at −196°c or −78°c. Figure 2 (*a*) (Pl. 146) shows the hysteresis loop of a crystal 22B after 6500 cycles ($\pm 1015\,\mathrm{g/m^2}$ resolved shear stress) at −78°c; the crystal was then rested at room temperature for 60 min and the loop width on immediate re-testing is shown in fig. 2 (*b*). After a further 100 cycles (fig. 2 (*c*)) the loop width had reached a size comparable to that prior to the interruption. The hardening tended to be most pronounced in the initial stages of a test when the deformation was carried out at −196°c or −78°c (fig. 3), but a large effect was still obtained on resting a week after 4×10^4 cycles.

---

† Communicated by the Author.

In tests undertaken at room temperature, not only was the observed hardening greater (fig. 4 (*a*)) but the effect persisted longer as can be seen by comparing the behaviour of an identical crystal at −196°c (fig. 4 (*b*)).

Fig. 3

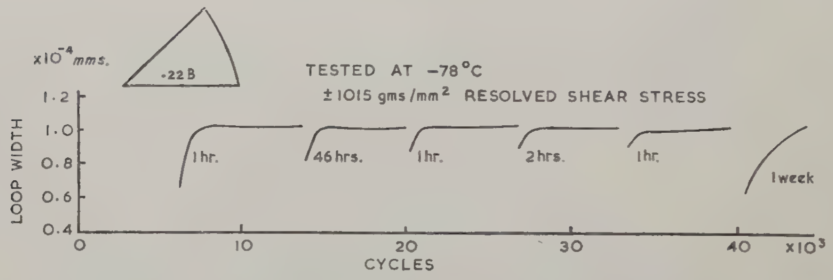

The effect of interruptions at room temperature on the loop width measured at −78°c.

Fig. 4

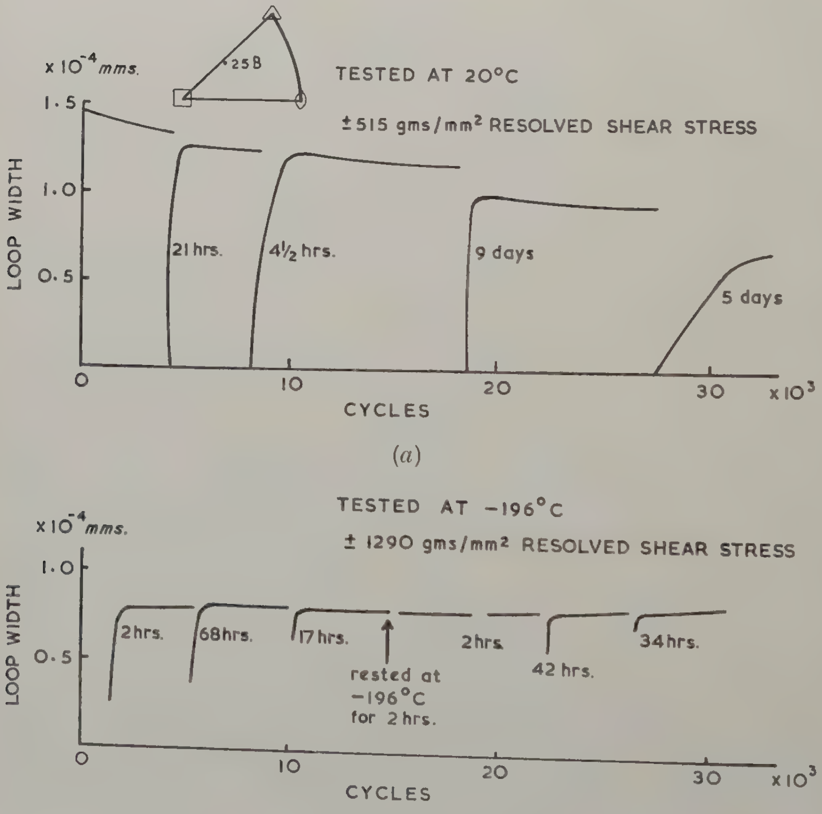

(*a*)

(*b*)

(*a*) The effect of room temperature interruptions on loop width measured at room temperature, (*b*) the effect of room temperature interruptions on the loop width measured at −196°c. (*a*) and (*b*) relate to tests carried out on identically oriented crystals.

The purity of the metal used is sufficiently high to exclude the possibility of impurity atom locking as a cause of the observed hardening, and to indicate instead point defects. Broom and Ham (1957, 1959) have suggested that point defects contribute to fatigue hardening by locking dislocations and moreover have shown yield phenomena when pure copper crystals previously fatigued at −196°C were deformed in tension in the range −196°C to 20°C. This view is supported by the electrical resistivity measurements of Rosenberg (1958) on copper fatigued at −253°C; the observed increase in resistivity is large with respect to that obtained as a result of uni-directional deformation and anneals out from −100°C upwards. The present experiments also indicate that point defects are formed during fatigue and migrate during resting at room temperature. It is thought that vacancy movement to dislocations will also explain the fatigue hardening observed in the present tests at room temperature.

The hardening obtained on resting is of a transitory nature for on further cycling the loop width (plastic strain) rapidly approached that which existed prior to resting. This appears to be in direct contrast to the results of tensile tests on fatigued crystals where a permanent upward displacement of the stress–strain curve was observed. The much bigger effect on the loop width observed at room temperature suggests that higher concentrations of point defects are generated than at lower temperatures, which would be in accord with the much heavier development of slip striae at room temperature (Hull 1958).

REFERENCES

BROOM, T., and HAM, R. K., 1957, *Proc. roy. Soc.* A, **242,** 166; 1959, *Ibid.*, **251,** 186.

HULL, D., 1958, *Phil. Mag.*, **3,** 513.

ROSENBERG, H. M., 1958, *Vacancies and other Point Defects in Metals and Alloys* (London: Institute of Metals), p. 206.

THOMPSON, N., COOGAN, C. K., and RIDER, J. G., 1955, *J. Inst. Met.*, **84,** 73.

The Variation with Time of the Flux and Energy Spectrum of Primary Cosmic Ray Alpha Particles†

By P. J. Duke

H. H. Wills Physics Laboratory, University of Bristol‡

[Received April 21, 1960]

Abstract

The total flux and energy spectrum of primary cosmic-ray alpha particles at the top of the atmosphere have been measured in emulsion stacks flown during September 1956 and June 1958. Values of 240 ± 26 and 130 ± 15 particles/m^2 steradian second respectively were obtained for the total flux. This reduction in the flux during June 1958 was caused by the partial removal of those alpha particles with energies between 100 and 2000 Mev/nucleon. These changes have been correlated with the 11-year cycle of solar activity.

§ 1. Introduction

It was pointed out by Forbush (1954) and others (e.g. Singer 1958), on the basis of observations made with neutron monitors at ground level, that periods of high solar activity, as measured by the Zurich sunspot number, were associated with a low cosmic-ray intensity. The corresponding variations in the flux and energy distribution of the primary radiation have been observed with nuclear plates flown to high altitudes and Freier *et al.* (1958) were able to show that the alpha particle flux in 1957 (measured over Minnesota) was reduced to about 50% of its value in 1954. Their results also indicated that this reduction was not caused by the application of an abrupt cut-off to the energy spectrum but that particles with energies as low as 200 Mev/nucleon were still able to reach the emulsions. The object of this present work has been to obtain further data on the energy spectrum and total flux of primary alpha particles using balloon-borne nuclear emulsions. The results have been obtained during September 1956 (Experiment 1) when the level of sunspot activity had risen considerably above the minimum of 1954 and in June 1958 (Experiment 2) near the maximum of the current solar cycle.

§ 2. Experimental Procedure

2.1. *September* 1956. *Experiment* 1

An emulsion stack consisting of 150 plates, each $40\,\text{cm} \times 30\,\text{cm} \times 600\,\mu$ in volume was flown to a mean height of 117 000 ft over Minnesota (North America) at a geomagnetic latitude of 55° N. for $6\frac{1}{4}$ hours. At this height the thickness of overlying air is equivalent to 6·5 g/cm^2. The observation and measurement of the alpha particles was divided into two parts, the first being the determination of the differential energy spectrum below 250 Mev/nucleon and the second the measurement of the total flux and the energy spectrum up to 1000 Mev/nucleon. For each section of the work a different sample of plates was searched using appropriate scanning criteria. In the first section only those tracks of density greater than 6 × minimum ionization were selected along a line 5 mm from the top edge of each plate. In the second section this density criterion was extended to 3 × minimum in order to include alpha particles of all possible energies. The alpha particles themselves were selected from all tracks recorded in the scanning by measuring the multiple coulomb scattering and grain density of each track. This method of identification was similar to that used by Fowler *et al.* (1958), except that in the present case the ionization was measured visually instead of using a densitometer. The scanning efficiency was checked in various ways. Some of the scanning was repeated by different observers and there was found to be no evidence for the omission of alpha particles. In addition, the number of alpha particles was found to be independent of the zenith angle (after correcting for atmospheric absorption) and the depth at which the track was found. It was assumed, therefore, that the scanning loss was negligible.

---

† Communicated by the Author.

‡ Now at the National Institute for Research in Nuclear Science, Harwell, Berkshire, England, and at present working at the Brookhaven National Laboratory, Upton, N.Y., U.S.A.

Fig. 1

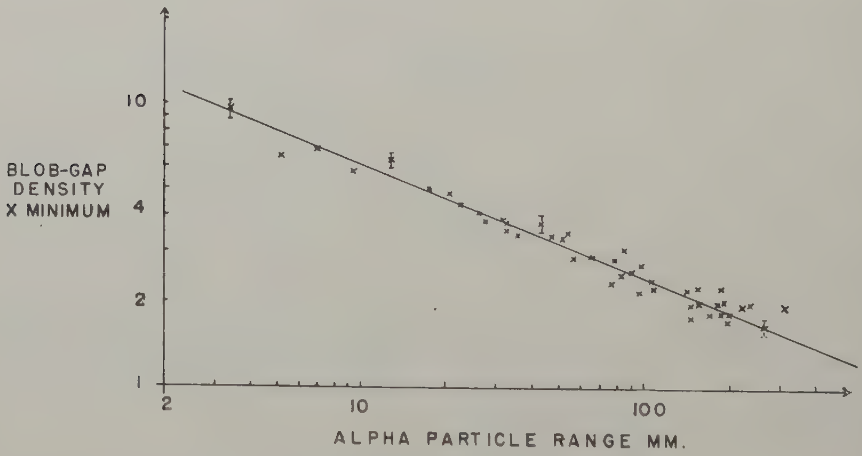

Blob-gap density–range relationship for alpha particles.

The methods used to obtain the alpha particle energies differed in parts 1 and 2 of experiment 1. In part 1 the measurement was based on a determination of either the grain density or the range of each track. Each alpha particle was followed through the emulsion stack until it either interacted, left the stack or came to rest. In the case of those particles which stopped, a measurement of the distance between the point of entry and the end point was sufficient to determine their energy. In those cases where the track did not end, the blob-gap density (Fowler and Perkins 1955) was measured either in the last few millimetres of available track or near to the point of entry. The blob-gap density was then related to the particle energy in the following way. A number of calibration plates were selected from those already scanned in part 1. These plates were searched for relativistic alpha particles which were used to give a value for the minimum blob-gap density in the plate concerned. All those alpha particles of known residual range which traversed the calibration plates were then blob-gap counted in those plates, to obtain a relationship between the blob-gap density, expressed as a multiple of the minimum density, and the residual range. The result of this procedure is shown in fig. 1. The full line shown in the figure was used to give the residual range of those alpha particles for which a direct range measurement could not be made. The energies which were obtained by this method were probably accurate to about ±10%.

In part 2, the alpha particle energies were obtained by a multiple coulomb scattering measurement, which was made over a length of track at least greater than 8 mm, using 500 μ cell sizes. The momentum and hence the energy of the particle was calculated using a value of the scattering constant obtained from the calculations of Fichtel and Friedlander (1958) and by eliminating the random noise between 500 μ and 1000 μ cell sizes, it being assumed that the contribution of the noise to the observations varied linearly with the cell size. This method gave a standard deviation of about ±15% in the energy region considered.

2.2. *June* 1958. *Experiment* 2

The dimensions of the stack in this second experiment were $20\,\text{cm} \times 12\,\text{cm} \times 600\,\mu$ and it was flown with the 20 cm edge uppermost over the same place as in Experiment 1 for $8\frac{1}{4}$ hours. The height was such that the mean thickness of air above the emulsions was $4\,\text{g/cm}^2$. The plates were scanned for all tracks greater than 3 × minimum, and the energies of the alpha particles were determined to an accuracy of 10–15% by multiple scattering measurements.

§ 3. RESULTS

The total fluxes were calculated using eqn. (1).

$$J = N\,\overline{\sec\theta}\cdot\frac{1}{A}\cdot\frac{1}{T}\cdot\frac{1}{\Omega}\ \text{particles/m}^2\,\text{ster. sec.} \qquad . \quad . \quad . \quad (1)$$

J = Flux of alpha particles ;
N = Number of particles ;
A = Area of emulsion ;
T = Time at maximum altitude ;
Ω = Solid angle ;
$\overline{\sec\theta}$ = Mean value of secant of zenith angle.

The values of N which were used in eqn. (1) were obtained from the numbers actually observed by correcting for the absorption of alpha particles and their production from the interactions of heavier nuclei in the emulsion and overlying atmosphere. These corrections were applied by inserting the fluxes of nuclei heavier than helium into the diffusion equations of Kaplon *et al.* (1954) and using the mean free paths and fragmentation probabilities of Rajopadhye and Waddington (1958). For the data of Experiment 1, values of 5, 15 and 5 particles/m^2 ster. sec were taken for the light, medium and heavy nuclei respectively, (cf. Dainton *et al.* (1952) and Kaplon *et al.* 1954), but for the results of Experiment 2 these values were reduced by 50%, it being assumed that the heavier components of the cosmic radiation decreased in the same proportion as the alpha particle flux (cf. Freier *et al.* 1959 a, b). The correction for those particles which arrived during the ascent of the emulsions was eliminated in Experiment 1 by launching the stack upside down and in Experiment 2 by launching it in an overturned position. The stacks were preset to rotate into the correct orientation when the maximum altitude was reached. Unfortunately, in Experiment 1, a short time was spent at altitude before rotation took place and a small correction was needed to allow for this.

Experiment number	Date	Number of alpha particles observed	Flux at top of atmosphere
1	September 18, 1956	200	240 ± 26 particles/m^2 ster. sec
2	June 14, 1958	167	130 ± 15 particles/m^2 ster. sec

The flux values which were obtained are shown in the table in which the errors shown are the standard deviations on the number of tracks observed, together with an allowance for the uncertainty in the thickness of the emulsion at the time of exposure. The number tabulated for Experiment 1 does not include the 75 particles with energies less than 250 MeV/nucleon which were obtained in part 1.

The differential energy spectra were obtained by extrapolating the observed energy of each alpha particle to the top of the atmosphere and then dividing the particles amongst suitable energy groups. The fluxes for each energy interval were found using eqn. (1) with the appropriate corrections. The resulting energy spectra are shown in fig. 2. There is good agreement between the two sets of low-energy results obtained in Experiment 1 even though the energies of the particles were found by different methods.

§ 4. Discussion

The results for the total flux of alpha particles obtained in the present experiment are compared in fig. 3 with other values obtained at a similar geomagnetic latitude but at different periods in the solar cycle (see Waddington (1960) for a list of references). The same figure also shows the variation with time of the Zurich sunspot number (Chernosky and Hagan 1958). It is clear that there is a strong anti-correlation between the alpha particle flux and the solar activity, as indicated by the sunspot number, so that periods of high solar activity are associated with a low flux of alpha particles. The most rapid change in the alpha particle flux coincides with the sharp rise to high sunspot number between 1955 and 1957.

Fig. 2

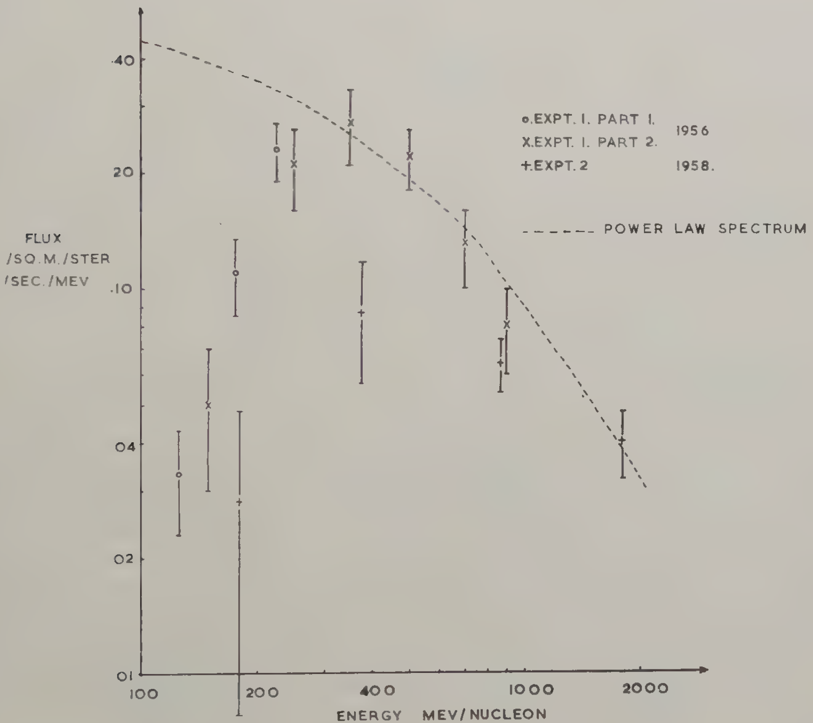

Differential energy spectrum.

The energy dependence of the variations can be seen from fig. 2. The spectrum obtained in September 1956 showed a pronounced peak in the region of 350 MEV/nucleon. At energies higher than that value the experimental points appeared to follow the power law given by eqn. (2) and shown by the hyphenated line in the figure:

$$\frac{dJ}{dE}=\frac{\text{Constant}}{(1+E)^{2\cdot5}}; \qquad \ldots\ldots\ldots \quad (2)$$

E = alpha particle energy in units of the particle rest energy. At energies below the peak there was a rapid decrease in intensity as the particle energy decreased to 100 MeV/nucleon. The alpha particle energy spectrum has been measured over a similar energy range in June 1954 at a geomagnetic latitude of 60°N. and, over the same place as this experiment, in October 1950 (Fowler *et al.* (1957) and Fowler *et al.* 1958), and in August 1956 (McDonald 1958). The results of McDonald were obtained with a Čerenkov and a scintillation counter and are in good agreement both with the results of Fowler *et al.* in 1950 and with the present experiment. However, the spectrum obtained in 1954 differs from those just mentioned in that it rises to a higher value at the peak energy of 350 MeV/nucleon and

Fig. 3

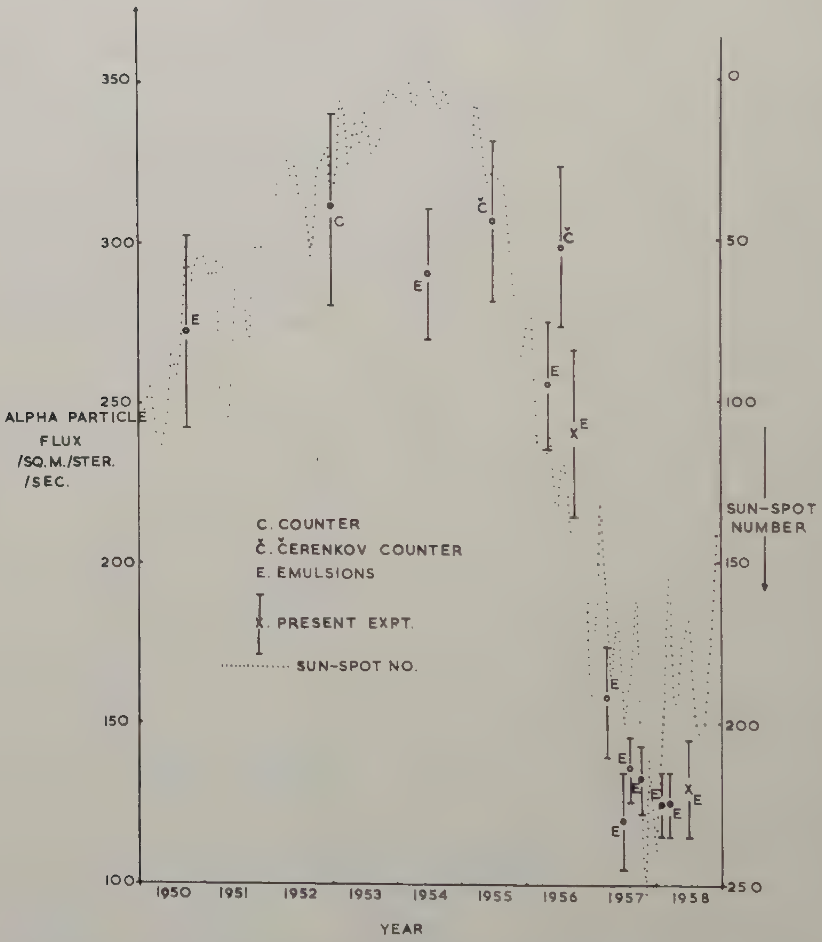

Variation of flux with time.

decreases less steeply between 350 and 150 MeV/nucleon. This may be related to the very low sunspot activity of 1954 compared with the increased activity in 1950 and 1956 on either side of the minimum. The spectrum of 1956 also showed that there was an appreciable number of alpha particles reaching the earth with energies approaching the limit of about 100 MeV/nucleon set by the air and packing materials above the emulsions. The fact that particles with energies as low as this were observed provided an upper limit to the cut-off energy over Minneapolis in 1956 which agrees with that observed by Fowler *et al.* (1957) in 1950 and which is somewhat lower than that given by the recent calculations of Quenby and Webber (1959).

The peak at 350 MeV/nucleon was still present in the 1958 results but it was much less prominent and the energy spectrum began to depart from the power law of eqn. (2) at a much higher energy, as can be seen in fig. 2. These results agree with those obtained in 1957 (Freier *et al.* 1959 b and Waddington 1960) and show that even during the years of maximum solar activity there are still an appreciable number of primary particles reaching the earth with energies as low as 200 MeV/nucleon as was observed by Freier *et al.* (1958). The height at which the emulsions were flown was sufficient to detect alpha particles of energy as low as about 80 MeV/nucleon but the number of particles observed with an energy of less than 200 MeV/nucleon was insufficient to determine the cut-off energy.

A number of attempts have been made to explain these variations but none are entirely satisfactory. Parker (1958 b) has attempted to explain the phenomena by invoking the solar wind hypothesis of Biermann (1951, 1952 and 1957). According to this theory, magnetic lines of force, emanating from the sun, are carried towards the outer regions of the solar system by a continual flow of ionized gas. It was predicted (Parker 1958 a) that this flow would become unstable in the region between the orbits of Mars and Jupiter and produce a shell of disordered magnetic field which would present a barrier to the incoming cosmic ray particles. Parker was able to show that for a given particle energy, the flux (J_0) in the vicinity of the earth would be related to that outside the barrier (J_∞) by eqn. 3.

$$J_0(E) = J_\infty(E) \exp\left\{ -A \cdot \left(\frac{Z}{M}\right)^2 \cdot \frac{E+1}{[E(E+2)]^{3/2}} \right\}. \quad . \quad . \quad (3)$$

In this equation Z/M is the change to mass ratio of the particles concerned and A is a constant depending only on the magnetic and geomagnetic properties of the barrier. The results of calculations based on eqn. (3), and assuming that $J_\infty(E)$ was given by eqn. (2), are shown in fig. 4. The lower curve was obtained using a value of $A(Z/M)^2$ of 0·58 which is that required by the calculations of Parker. The upper curve uses a value for $A(Z/M^2)$ equal to 0·12. There is fair agreement between the theoretical predictions and the experimental results. Unfortunately the theory does not predict any variation in the energy spectrum above about 2 BeV/nucleon in contrast to the observations made using neutron monitors (Forbush 1954, 1958).

Fig. 4

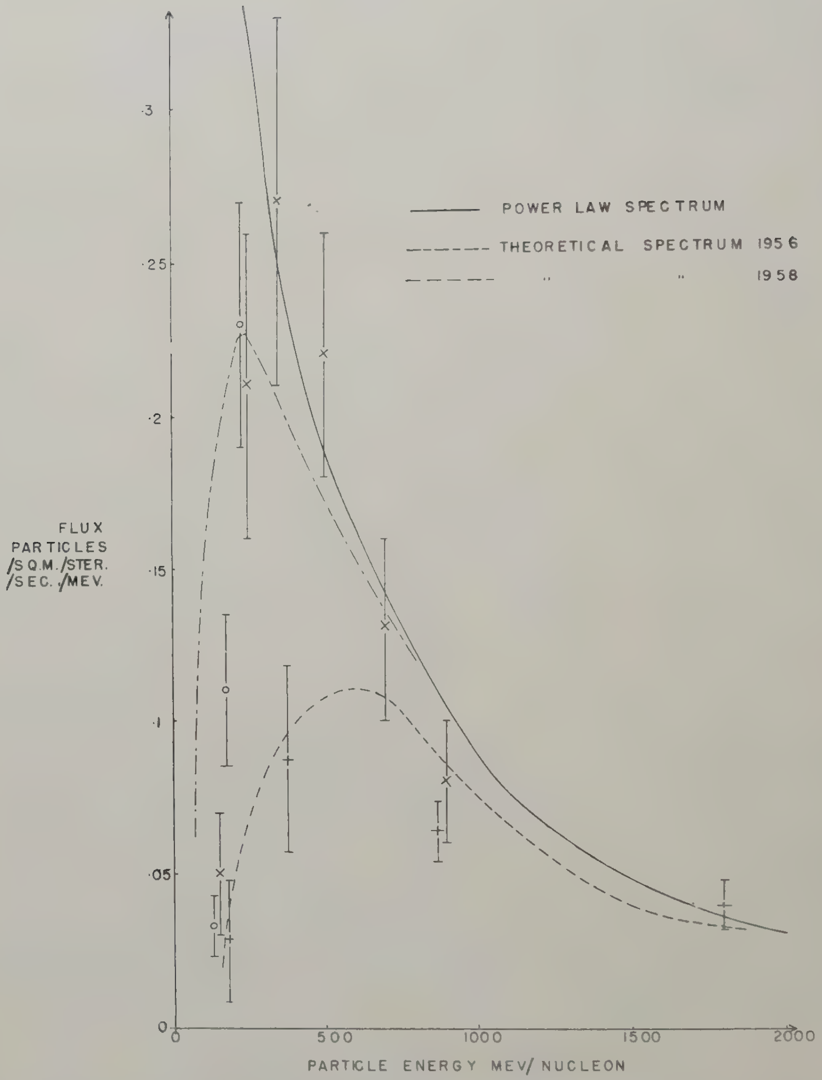

Comparison between theory and experiment.

§ 5. Conclusions

The total flux and the energy spectrum below about 2000 Mev/nucleon of primary cosmic ray alpha particles have been measured on two separate occasions. The results exhibit a strong anti-correlation between alpha particle intensity and solar activity and are in general agreement with the theory of Parker (1958 b). In spite of this, the theoretical understanding of the relationship between the cosmic-ray observations and the solar activity is still unsatisfactory.

ACKNOWLEDGMENTS

I am grateful to Professor C. F. Powell for his interest in this work and for his help and encouragement.

During the course of this experiment I have had many useful discussions with Dr. P. H. Fowler, Dr. C. J. Waddington, Dr. R. R. Hillier, and Mr. D. E. Evans.

I am indebted to the Misses B. Bolt, M. Brook, P. Curry, and P. Shore for their careful scanning of the plates and their assistance with some of the measurements.

This work was carried out during my period of tenure of a D.S.I.R. Research Fellowship.

REFERENCES

BIERMANN, L., 1951, *Z. Astrophys.*, **29,** 274; 1952, *Z. Naturforsch.* A, **7,** 127; 1957, *Observatory*, **77,** 109.
CHERNOSKY, E. J., and HAGAN, M. P., 1958, *J. geophys. Res.*, **63,** 775.
DAINTON, A. D., FOWLER, P. H., and KENT, D. W., 1952, *Phil. Mag.*, **43,** 729.
FICHTEL, C., and FRIEDLANDER, M. W., 1958, *Nuovo Cim.*, **10,** 1032.
FOWLER, P. H., FREIER, P. S., and NEY, E. P., 1958, *Nuovo Cim.* (Suppl.), **8,** 492.
FOWLER, P. H., and PERKINS, D. H., 1955, *Phil. Mag.*, **46,** 587.
FOWLER, P. H., WADDINGTON, C. J., FREIER, P. S., NAUGLE, J., and NEY, E. P., 1957, *Phil. Mag.*, **2,** 157.
FORBUSH, S. E., 1954, *J. geophys. Res.*, **59,** 525; 1958, *Ibid.*, **63,** 651.
FREIER, P. S., NEY, E. P., and FOWLER, P. H., 1958, *Nature, Lond.*, **181,** 1319.
FREIER, P. S., NEY, E. P., and WADDINGTON, C. J., 1959 a, *Phys. Rev.*, **113,** 921; 1959 b, *Ibid.*, **114,** 365.
KAPLON, M. F., NOON, J. H., and RACETTE, G. W., 1954, *Phys. Rev.*, **96,** 1408.
MCDONALD, F. B., 1958, *Phys. Rev.*, **109,** 1367.
PARKER, E. N., 1958 a, *Phys. Rev.*, **109,** 1874; 1958 b, *Ibid.*, **110,** 1445.
QUENBY, J. J., and WEBBER, W. R., 1959, *Phil. Mag.*, **4,** 90.
RAJOPADHYE, V. Y., and WADDINGTON, C. J., 1958, *Phil. Mag.*, **3,** 19.
SINGER, S. F., 1958, *Progress in Elementary Particle and Cosmic Ray Physics*, **4,** 203 (Amsterdam: North-Holland Publishing Co.).
WADDINGTON, C. J., 1960, *Progress in Nuclear Physics*, **8** (London: Pergamon Press), to be published.

Soft X-ray Emission from Potassium Metal in the 40–1000 Å Range†

By R. S. Crisp‡
Department of Physics, University of Western Australia, Nedlands, W.A.

[Received June 1, 1960]

Abstract

The emission in the 40–1000 Å range, excited in a potassium target by electron bombardment, has been examined using the grazing incidence photon counting spectrometer described previously. A total of seven lines and bands are observed of which two are identified as the L and M valence spectra, three are identified as diagram lines, and two broad lines remain unidentified. An energy level scheme for solid potassium in emission has been constructed.

A note regarding the energy of the L_1 level in sodium, magnesium and aluminium is appended.

§ 1. Introduction

The M spectrum of solid potassium has been observed previously by Kingston (1951) and by Fisher *et al.* (1958) while Tyrén (1937) has observed the Ll, Lη doublet. Although the present research has been concerned principally with valence band spectra, in the case of potassium a number of atomic lines also fall in the relevant spectral range and their wavelengths may be measured. These lines can be identified by reference to the extrapolated energy values for the L and M levels, and hence exact values for these energy levels may be obtained.

§ 2. Instrumental

The spectrometer has been described in detail previously by Fisher *et al.* (1958). A number of modifications have been made subsequently and are discussed elsewhere by Crisp and Williams (1960). They include a cold baffle which nearly surrounds the target and which practically eliminated carbonaceous contamination (Crisp 1958, Ennos 1953, 1954), an improved photomultiplier detector, and replacement of the aluminium grating by a ruled glass grating which gave intense spectra down to 45 Å and enhanced reflectivity in high orders (Crisp 1960).

---

† Communicated by the Author.

‡ Now at National Research Council, Ottawa.

The targets were prepared by the evaporation of pure potassium, from a stainless-steel cup, on to a water-cooled copper target. The metal was loaded into the cup, freshly cut under the packing oil and wet with oil which was subsequently pumped off. In the preparation of an actual target, before depositing the specimen metal, the specimen chamber was 'gettered' by a massive evaporation of potassium and the copper target freshly cleaned by means of the scraper. Pressures of lower than 10^{-6} mm Hg were produced in this way and cleanliness of the specimen was ensured.

Wavelengths were calculated from the fiducial marker 'pips' on the chart records. The method of calculating the theoretical calibration curve has been indicated by Fisher *et al.* (1958) and Crisp (1960). A correction curve to this calibration was drawn using the emission edges of the L spectra of aluminium and magnesium, and the peak of the boron K spectrum in several orders. Skinner's (1940) wavelengths were taken as the 'true' wavelengths of these features and unknown wavelengths could then be determined absolutely with a probable error of ± 0·5 Å. *Differences* in wavelength may be measured with an error of ± 0·05 Å. The random errors incurred in making actual measurements on the charts may generally be reduced to a negligible figure by averaging a large number of records. The small systematic error introduced by the finite width of the analyser slit is automatically eliminated in the construction of the correction curve.

The slits were set at 40–45 μ and on the criterion of Fisher (1954) this corresponds to an optical resolution of 0·9 Å. The instrumental width referred to hereafter is merely this 0·9 Å converted to electron volts and will be somewhat smaller than the true 'line width' as used for example by Skinner (1940).

§ 3. EXPERIMENTAL RESULTS

The seven observed lines could be conveniently divided into three groups:

(i) The valence M spectrum (fig. 1†).

(ii) A number of diagram lines and the valence L spectrum (fig. 3).

(iii) Two unidentified broad lines designated X and Y for convenience (fig. 3).

The numerical data are set out in table 1, and the lines observed are illustrated in figs. 1 and 3 which are photographs of typical chart records. On each record the spectrum and order, target current and voltage, full scale counting rate and percentage error (Elmore and Sands 1949), optical resolution, target chamber vacuum and an approximate wavelength scale are indicated.

---

† Figures 1 and 3 are shown as plates.

Table 1. Emission lines from solid potassium
(Wavelengths for $M_{23}V$ are for the edge and extrapolated low energy limit)

Line	Peak (Å)	Peak energy (ev)	Half-width (ev)	Inst. width (ev)	Peak intensity counts/sec/mA at 4 kv
$M_{23}V$	$677{\cdot}9_2$ $\pm 0{\cdot}5$ 744 ± 1	$18{\cdot}28_7$ $\pm 0{\cdot}01$ $16{\cdot}66_3$ $\pm 0{\cdot}02$	$1{\cdot}62_4$ $\pm 0{\cdot}04$	0·025	500
L_3M_1 (Ll)	$47{\cdot}63_3$ $\pm 0{\cdot}15$	$260{\cdot}2_7$ $\pm 0{\cdot}8$	$1{\cdot}96$ $\pm 0{\cdot}11$	1·4	2300
L_2M_1 ($L\eta$)	$47{\cdot}22_5$ $\pm 0{\cdot}15$	$262{\cdot}5_2$ $\pm 0{\cdot}8$	$1{\cdot}96$ $\pm 0{\cdot}11$	1·4	1050
L_1L_3	$284{\cdot}6_9$ $\pm 0{\cdot}7$	$43{\cdot}54_8$ $\pm 0{\cdot}10$	$0{\cdot}7_5$ $\pm 0{\cdot}1$	0·14	30
$L_{23}V$	$41{\cdot}5_5$ $\pm 0{\cdot}4$	$298{\cdot}3_7$ $\pm 2{\cdot}7$	—	—	40
X	$50{\cdot}03$ $\pm 0{\cdot}15$	$247{\cdot}8_0$ $\pm 0{\cdot}07$	$4{\cdot}99_6$ $\pm 0{\cdot}26$	1·25	850
Y	$103{\cdot}0_9$ $\pm 0{\cdot}6$	$120{\cdot}2_6$ $\pm 0{\cdot}7$	$2{\cdot}9_8$ $\pm 0{\cdot}3$	1·2	35

Additional information:

$E_{L\eta} - E_{Ll} = 2{\cdot}25 \pm 0{\cdot}3$ ev.
Edge width for $M_{23}V = 0{\cdot}19 \pm 0{\cdot}01$ ev.

§ 4. Discussion

4.1. *The M Valence Spectrum*

The M band emitted when conduction (4s) electrons make transitions into ionized M_{23}(3p) levels is shown in fig. 1 and has been observed previously by Kingston (1951) and Fisher *et al.* (1958).

The b.c.c. alkali metal, potassium, has one valence electron per atom and is therefore expected to have a half-filled first Brillouin zone. In addition, since the first zone for an ideal b.c.c. lattice may contain 1·48 electrons per atom before the Fermi surface departs from a sphere, and since it has been calculated that for the real metal potassium the relative effective mass of the conduction electrons is 0·94 (Kittel 1956), it is anticipated that the conduction electrons in potassium will behave very much like free electrons. Hence the density of states function $N(E)$, is expected to vary parabolically with E as measured from the bottom of the band, to show a sharp cut-off at the Fermi surface and to show no evidence of zone overlap in the occupied states.

This behaviour is observed in the M emission curve of fig. 1 and in fig. 2 where the measured ordinates on the emission curve, which are recorded on a wavelength scale, are multiplied by the factor λ^3 and replotted on an energy scale to give the $f(E)N(E)$ curve (Tomboulian 1957). The broken curve in fig. 2 represents a parabolic (or $E^{1/2}$) extrapolation of the low energy portion of the curve in order to 'remove' the tail (Skinner 1940). The extrapolated bandwidth so obtained is $1{\cdot}62_4 \pm 0{\cdot}04$ ev which is smaller than the value $1{\cdot}9 \pm 0{\cdot}2$ ev given by Kingston (1951). The extrapolation shown in fig. 4 of Kingston's paper is hard to justify, and gives an excessive value for the bandwidth though the emission curve given is in close agreement with the present finding. Both these experimental values are less than the Sommerfeld 'free electron' width of 2·1 ev.

Fig. 2

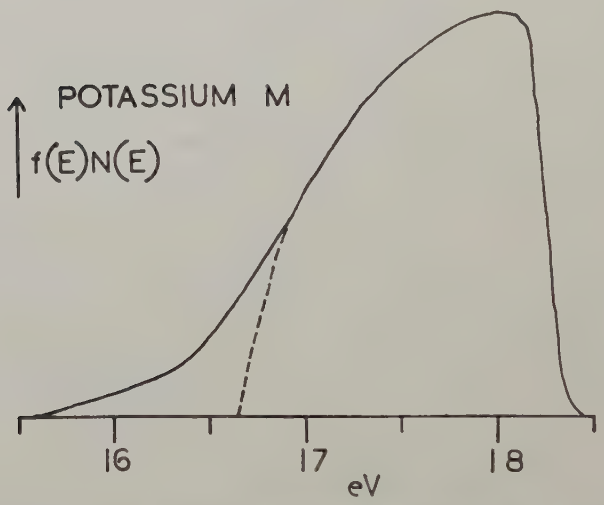

Plot of $f(E)N(E)$ vs. E deduced from the potassium M emission band.

The observed width of the emission edge is $0{\cdot}19 \pm 0{\cdot}01$ ev from 5% to 95% of the maximum intensity with the instrumental width 0·024 ev. It would appear, therefore, that about 0·17 ev of the edge width must be accounted for by temperature effects and by the width of the core level (M_2 or M_3) in emission.

There is no evidence of the edge doubling which is seen in the L spectra of the metals magnesium and aluminium, and which arises from the doublet nature of the 2p levels. The absence of edge doubling may result from either the M_2, M_3 separation being small (less than a few hundredths of an electron volt) or the M_2 band intensity being very low. Since an M_2, M_3 separation of at least some few tenths of an electron volt is expected by extrapolation from elements of higher atomic number, it must be concluded that the M_2 band intensity is very low ($<1\%$ of the M_3 band intensity). This conclusion is not entirely consistent with the results obtained by Skinner *et al.* (1954) for the M_2, M_3 separations and relative intensities for the iron transition series, but a similar near absence of the L_2 spectrum was observed in sodium by Skinner (1940).

The 0·17 ev breadth of the emission edge must then be explained partly by the width of the M_3 level and partly by temperature effects on the Fermi edge whose width from 5% to 95% of the maximum is equal to $6kT$. Since $6kT$ has values of 0·15 ev and 0·17 ev at temperatures of 20°c (cooling water temperature) and 56°c, it is seen that the maximum possible value of the M_3 width is 0·02 ev, or alternatively that the maximum possible temperature of the *emitting* atoms was 56°c. Either conclusion is quite consistent with the experimental conditions.

4.2. *The Diagram Lines and the L Valence Spectrum*

The various lines, other than the M valence band spectrum, are illustrated in fig. 3. The identifications are indicated and were made using the energy level values of Hill *et al.* (1952) and Fine and Hendee (1956) and the wavelengths of the Ll, $L\eta$ doublet given by Tyrén (1937). The peak wavelengths, widths, etc., are listed in table 1, as well as data for the two broad unidentified lines which for convenience are designated X and Y.

4.2.1. *The* 47 Å *doublet*

The doublet at 47 Å emitted when electrons make transitions from the M_1 (3s) level to the two L_{23} (3p) levels, was unresolved in first order but partially resolved in fourth order. Separation of the observed fourth-order spectrum into its two components was effected by assuming two nearly Gaussian profiles of equal widths with the intensity ratio of 2·2 : 1. Though this differs from the ideal ratio 2 : 1 it is consistent with the rapid fall of grating reflectivity in this region near cut-off. The absolute wavelength of either component is determined to 0·15 Å from fourth-order spectra, while the separation is measurable to within 0·05 Å from the same spectrum.

4.2.2. *The* 284 Å *line,* L_1L_3

Emission lines resulting from transitions within the L shell have been observed by Skinner (1940) and identified by Tomboulian and Cady (1941). The line identified as L_1L_3 in the present case is very weak (fig. 3), but it appeared on all records and its energy may be computed fairly accurately. Little can be said about the width except that it is less than 0·75 ev.

The line is identified as L_1L_3 rather than L_1L_2 or L_1L_{23} since the L_1L_3 intensity is expected to be at least twice as great as that of L_1L_2, and there is no sign of another line 15 Å distant as would be anticipated from the proposed L_2, L_3 separation of 2·25 ev.

The analogous line M_1M_3, expected at about 620 Å, was not observed.

Fig. 4

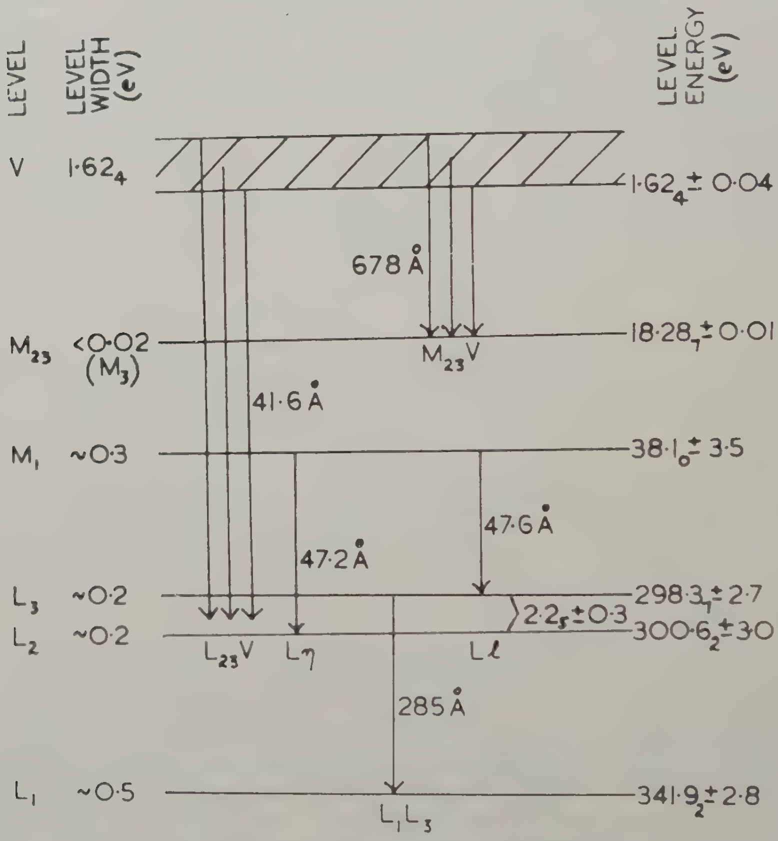

Conventional energy level diagram for solid potassium constructed from observed emission wavelengths.

4.2.3. *The L_{23} valence spectrum*

A faint line at 41 Å is identified as the L_{23} valence spectrum (fig. 3). The intensity is very low on account of the proximity of the grating reflectivity cut-off but the line was seen on all records. The peak wavelength was computed by measuring the separation from the Ll, Lη doublet. This procedure gave a probable error of ± 0·38 Å instead of ± 0·7 Å if the peak wavelength had been obtained directly from the calibration table. Since the instrumental width in this region is 7·2 ev a value is not quoted for the band width. However, the 'line' will be several electron volts broad since the 1·62 ev spread of the valence electrons and the 2·25 ev separation of the L_2 and L_3 levels both contribute to its width.

4.3. *Unidentified Lines*

There remain two lines, X and Y, which will not fit in with the proposed energy level scheme of fig. 4. In addition, their widths are excessive and not compatible with the approximate level widths of fig. 4.

4.3.1. *The line X at* 248 *eV*

It is not feasible to ascribe the line X to emission from contamination of the target since its intensity was high, its intensity relative to Ll did not change with time and there was no trace of carbon K radiation or visible deterioration of the target after bombardment for half an hour or more. The line has also been observed by Jacob (1956, private communication). The line is not a satellite with an initial state of the type KL_2, KL_3, etc., since it is still observed at the same intensity relative to Ll when the target voltage is reduced to 2·5 kv. The ionization energy of the K level is about 3·6 kev. Furthermore there is no obvious parent line for a satellite with an initial state of the type L_1L_2, L_3L_2, etc.

If it is assumed that one of the states involved in the transition giving rise to the line X is L_2 or L_3, then the other must be a band of excitation (?) states, several electron volts wide and lying some 10 ev below the M_1 level. Such excitation states have been observed by Parratt (1959) for the *valence* levels of manganese.

4.3.2. *The line Y at* 120 *eV*

As with the line X, the line Y cannot be fitted to the proposed energy level scheme. However, its intensity is very low (~ 1/20 that of the line X) and it could conceivably have been emission from a contaminant though such a possibility seems remote. It is too broad to be the result of a transition between two sharp atomic levels though it may be an unresolved doublet. Once again it is hard to identify it as a satellite line for lack of a suitable parent potassium line.,

§ 5. THE ENERGY LEVEL DIAGRAM

The conventional energy level diagram for solid potassium, constructed entirely from the present data, is shown in fig. 4. The transitions observed are indicated, as well as the energies and widths computed from them for the valence, and the three L and three M levels. In constructing the diagram the peak of the $L_{23}V$ spectrum was assumed to be the peak of the L_3V component which is expected to be at least twice as intense as L_2V.

§ 6. L_1 LEVELS OF SODIUM, MAGNESIUM AND ALUMINIUM

The transition L_1L_3 in the metals sodium, magnesium and aluminium has been observed by Skinner (1940) and identified by Tomboulian and

Cady (1941). The value of the L_1 energy level relative to the highest occupied valence level may be calculated by summing the energy of the L_1L_3 transition, and the transition energy corresponding to the L_3 emission edge. Tomboulian and Cady (1941) have made this calculation using Skinner's (1940) data.

The L_1L_3 transition has been observed in the present case for these three metals. However, while the wavelengths for sodium (379·6 ± 1·0 Å) and magnesium (317·8 ± 0·5 Å) are in fair accord with previous results, that for aluminium (274·5 ± 0·5 Å) is not. A reason for the discrepancy is not forthcoming, though Skinner's (1940) wavelengths are quoted only as rough values in a footnote. The relevant data, and the calculation for the L_1 level energy, using Skinner's (1940) wavelengths for the L_3 emission edges, are given in table 2.

Table 2. Evaluation of the L_1 energy level in Na, Mg and Al

<table>
<tr><th></th><th>Na</th><th>Mg</th><th>Al</th></tr>
<tr><td rowspan="2">λL_3 edge</td><td>405·45 ± 0·05</td><td>250·45 ± 0·05</td><td>170·56 ± 0·05</td></tr>
<tr><td colspan="3">(Wavelengths from Skinner 1940)</td></tr>
<tr><td>E_{L_3} edge (ev)</td><td>30·577 ± 0·004</td><td>49·500 ± 0·010</td><td>72·67 ± 0·02</td></tr>
<tr><td rowspan="3">λL_1L_3</td><td>379·6 ± 1·0</td><td>317·8 ± 0·5</td><td>274·5 ± 0·5</td></tr>
<tr><td colspan="3">(Wavelengths from present investigation)</td></tr>
<tr><td>(375)</td><td>(317·4)</td><td>(290)</td></tr>
<tr><td>$E_{L_1L_3}$</td><td>32·66 ± 0·09
(33·06)</td><td>39·01 ± 0·06
(39·06)</td><td>45·16 ± 0·08
(42·67)</td></tr>
<tr><td>L_1 energy (ev)</td><td>63·24 ± 0·09
(63·64)</td><td>88·51 ± 0·07
(88·56)</td><td>117·85 ± 0·10
(115·34)</td></tr>
</table>

The values in parentheses, without errors, are from Skinner's (1940) wavelengths for the peak of the L_1L_3 lines.

ACKNOWLEDGMENTS

The author wishes to thank Dr. S. E. Williams, who supervised the work, for his help and suggestions, Professor A. G. McLellan of Christchurch for the loan of the glass grating, Dr. W. Baumgartner of Institut für technische Physik der E.T.H., Zurich, for co-operation in supplying the photomultiplier, and the Australian Atomic Energy Commission for a Postgraduate Research Studentship during the tenure of which the work was carried out. The continued interest of Professor C. J. B. Clews is gratefully acknowledged.

REFERENCES

CRISP, R. S., 1958, *Aust. J. Phys.*, **11**, 449; 1960, *Opt. Acta* (in the press).
CRISP, R. S., and WILLIAMS, S. E., 1960, *Phil. Mag.* (in the press).
ENNOS, A. E., 1953, *Brit. J. appl. Phys.*, **4**, 101; 1954, *Ibid.*, **5**, 27.
ELMORE, W. C., and SANDS, M., 1949, *Electronics* (McGraw-Hill), p. 250.
FINE, S., and HENDEE, C. F., 1956, *Norelco Reporter*, **3**, 113.
FISHER, P., 1954, *J. opt. Soc. Amer.*, **44**, 665.
FISHER, P., CRISP, R. S., and WILLIAMS, S. E., 1958, *Opt. Acta*, **5**, 31.
HILL, R. D., CHURCH, E. L., and MIHELICH, J. W., 1952, *Rev. sci. Instrum.*, **23**, 523.
KINGSTON, R. H., 1951, *Phys. Rev.*, **84**, 944.
KITTEL, C., 1956, *Introduction to Solid State Physics*, 2nd ed. (New York : John Wiley and Sons), p. 317.
PARRATT, L. G., 1959, *Rev. mod. Phys.*, **31**, 616.
POLLARD, J., 1953, *Rev. sci. Instrum.*, **24**, 996.,
SKINNER, H. W. B., 1940, *Phil. Trans.* A, **239**, 95.
SKINNER, H. W. B., BULLEN, T.G., and JOHNSTON, J. E., 1954, *Phil. Mag.*, **45**, 1070.
TOMBOULIAN, D. H., 1957, *Handb. Phys.*, **30** (Berlin: Springer), p. 246.
TOMBOULIAN, D. H., and CADY, W. M., 1941, *Phys. Rev.*, **59**, 422.
TYRÉN, F., 1937, *Ark. Mat. Astr. Fys.* A, **25**, 1.

The Influence of Solutes on Self-diffusion in Metals†

By A. B. LIDIARD
Physics Department, The University, Reading, Berkshire

[Received June 20, 1960]

ABSTRACT

A statistical theory of the effect of solutes on solvent self-diffusion in dilute alloys is given. It is based on the vacancy model used previously by Hoffman, Turnbull and Hart and includes a qualitative consideration of correlation effects. Two limiting cases are considered: (i) in which the vacancy jump frequencies are not greatly changed by the solute atoms (' weak perturbation ' limit), (ii) in which the vacancies attach themselves strongly to solute atoms and where the jump frequencies may be greatly different (' tight-binding ' limit). In both cases it is shown how experimental data on solute enhanced diffusion of solvent atoms combined with knowledge of solute tracer diffusion rates may be used to deduce ' correlation factors ' for solute diffusion. Analysis of existing data on dilute Ag alloys yields similar correlation factors whichever of the two limiting equations we use. The results are not consistent with the absence of isotope effects in Cd and In diffusion in Ag : this may indicate that the model is inadequate for the discussion of solute enhanced diffusion. Further experimental work, particularly on isotope effects, is called for.

§ 1. INTRODUCTION

A number of authors (Seitz 1950, Overhauser 1953, Hoffman *et al.* 1955, Hart *et al.* 1955, Hoffman 1958, Lazarus 1955, Lomer 1958, Reiss 1959) have treated the problem of the influence of small concentrations of solutes on metallic self-diffusion. These discussions have been based on a vacancy model of diffusion and have assumed the frequency of solute-vacancy exchange to be different from the rate of solvent-vacancy exchange in the pure solvent. The frequencies of solvent-vacancy exchange in the immediate vicinity of a solute atom also are assumed to be different from their values in the pure solvent. Longer range effects have sometimes been included (Overhauser 1953). In the present note we shall concern ourselves with the model which treats the effects of the solute atom on vacancy jump frequency as localized. This is the model which most authors have used, but their results are not always consistent. In particular, various results have been presented for the concentrations of vacancies in a dilute alloy. In the next section we present the statistical thermodynamic argument by which the correct results for the local model may be derived and in the following sections we consider the application to self-diffusion in a very dilute alloy. Then in § 3 we show how an analysis of the effects of solutes on solvent self-diffusion may be used to make inferences about *solute* diffusion. In particular we are able to derive values for the correlation factor for solute diffusion (LeClaire and Lidiard 1956, Manning 1959). Knowledge of these factors is necessary to theories of the elementary jump processes. The inferred values for a number of solutes in Ag are given in the table. Those for Cd and In are not consistent with the absence of isotope effects in the diffusion of these elements (Schoen 1958 a, b). This may indicate the inadequacy of the present model for the description of the effect of solutes on solvent self-diffusion; as the isotope effect experiments in principle yield more direct information about correlation factors their extension to other solutes would be valuable.

---

† Communicated by the Author.

§ 2. VACANCY CONCENTRATIONS IN A DILUTE ALLOY

We assume the alloy to be composed of N solvent atoms and N_i solute atoms randomly distributed. It will be supposed that the energy of formation of a vacancy at a site which is a nearest neighbour of a solute atom is different from the energy of formation at more distant sites, but we neglect any interaction between solute atoms and vacancies which are not nearest neighbours (this is in general agreement with the electronic theory of these interactions). We therefore specify the state of the system by giving the number of nearest-neighbour solute-vacancy pairs and the number, n_{V}, of 'free' vacancies. Let the former be N_ip, so that a fraction p of the impurity atoms are associated with vacancies.

If the Gibbs free energy of vacancy formation is g_{V} for a free vacancy and $(g_{\mathrm{V}}+\Delta g)$ for an associated vacancy, i.e. $-\Delta g$ is the energy of solute-vacancy association, the free energy of the crystal containing n_{V} free vacancies and N_ip associated vacancies includes a term

$$n_{\mathrm{V}}g_{\mathrm{V}}+N_ip\,(g_{\mathrm{V}}+\Delta g). \qquad (2.1)$$

We must also calculate the configurational entropy associated with the various arrangements of defects all of energy (2.1), To do this we note first that the total number of lattice sites is

$$N_{\mathrm{s}}=N+N_i(1-p)+2N_ip+n_{\mathrm{V}}=N+N_i+N_ip+n_{\mathrm{V}}. \qquad (2.2)$$

The number of ways of arranging the N_ip solute-vacancy pairs among these N_{s} sites is

$$\frac{(z)^{N_ip}}{(N_ip)\,!}\prod_{s=0}^{(N_ip-1)}(N+N_i+N_ip+n_{\mathrm{V}}-2s). \qquad (2.3)$$

Here z is the number of nearest neighbours, i.e., the number of distinct orientations of a solute-vacancy pair. Expression (2.3) neglects small hindrances to the rotation of one pair caused by the proximity of others; these are negligible at the low concentration limit of interest here. After we have arranged the solute-vacancy pairs in one of the above (2.3) configurations there remain $N+N_i-N_ip+n_{\mathrm{V}}$ sites. The n_{V} free vacancies, $N_i(1-p)$ free solute atoms and N solvent atoms are to be arranged on these sites subject to the condition that no vacancies and impurities be nearest neighbours of one another—since they would then constitute a solute-vacancy pair. First, the number of ways of putting the $N_i(1-p)$ free solute atoms onto the $N+N_i(1-p)+n_V$ available sites is

$$\frac{(N+N_i(1-p)+n_V)\,!}{[N_i(1-p)]\,!\,(N+n_V\,!)}. \qquad (2.4)$$

There then remain $N+N_i(1-p)+n_V$ less $(z+1)N_i(1-p)$ sites on which to arrange the n_V vacancies. This can be done in

$$\frac{(N-zN_i(1-p)+n_V)\,!}{[N-zN_i(1-p)]\,!\,n_V\,!} \qquad (2.5)$$

ways. The product of the expressions (2.3), (2.4) and (2.5) gives the total number of configurations of energy (2.1). Actually in these configurations we have included some, e.g. a solute atom in the vicinity of a solute-vacancy pair, to which strictly we should assign an energy different from (2.1), but these configurations are so few that no significant error is introduced into the calculation. From expressions (2.1)–(2.5) we can immediately write down the free energy of the crystal: relative to a crystal without vacancies it is

$$\begin{aligned} G = -\boldsymbol{k}T \ln \Bigg\{ & \frac{(z)^{N_ip}}{(N_ip)\,!} \prod_{s=0}^{(N_ip-1)} (N+N_i+N_ip+n_V-2s) \\ & \times \frac{(N+N_i(1-p)+n_V)\,!}{[N_i(1-p)]\,!\,(N+n_V)\,!} \\ & \times \frac{(N-zN_i(1-p)+n_V)\,!}{[N-zN_i(1-p)]\,!\,n_V\,!} \Bigg\} + n_Vg_V + N_ip(g_V+\Delta g). \end{aligned} \qquad (2.6)$$

The average therodynamic values of n_V and p are obtained in the usual way by setting

$$\frac{\partial G}{\partial n} = 0 = \frac{\partial G}{\partial p}.$$

It is not difficult to show that these conditions lead to the following results, valid to first order in the concentration of solute atoms;

$$\frac{n_V}{N_S - N_ip - zN_i(1-p)} = \exp\left(-\frac{g_V}{\boldsymbol{k}T}\right) \qquad (2.7)$$

and

$$N_ip = N_iz \exp\left(-\frac{g_V+\Delta g}{\boldsymbol{k}T}\right). \qquad (2.8)$$

Hence the average number of free vacancies n_V is the same as in a pure solvent with only $N_S - N_ip - zN_i(1-p)$ sites. The terms subtracted from the actual total number of sites N_S are the number of associated vacancy sites (N_ip) and the $zN_i(1-p)$ precluded sites around the unassociated impurities. The degree of association p, by (2.8), will in general be small compared to unity and (2.7) may then be re-expressed as

$$x_V = (1-zc)\ \exp(-g_V/\boldsymbol{k}T) \qquad (2.9)$$

where $x_V = n_V/N_s$ and $c = N_i/N_s$ are molar fractions of free vacancies and solute atoms. Equation (2.9) is the expression used by Lomer (1958): it has also been obtained by LeClaire (unpublished) who calculated the entropy term by writing down the number of ways that the N_ip pairs could be arranged on the $N_sz/2$ bonds of the lattice. In the following sections we shall use (2.7) as well as (2.8).

§ 3. APPLICATION TO SELF-DIFFUSION IN DILUTE ALLOYS OF FACE-CENTRED CUBIC STRUCTURE

The elementary random walk theory of diffusion in an isotropic lattice gives the following expression for the diffusion coefficient (see e.g. Chandrasekhar 1943),

$$D = \tfrac{1}{6}\,\Gamma\,s^2 \quad . \quad . \quad . \quad . \quad . \quad . \quad . \quad . \quad (3.1)$$

in which Γ is the average number of jumps made by a diffusing atom in unit time and s is the magnitude of the jump distance. A more complete analysis of vacancy diffusion includes a consideration of the effects of correlation between successive vacancy jumps† (Bardeen and Herring 1952). In the present connection we do not aim to include these rigorously; we proceed first on the assumption that (3.1) is valid and indicate possible ways in which correlation effects may enter. We confine ourselves to a face-centred cubic lattice and begin by calculating Γ.

In the present model of a dilute alloy there are several distinct vacancy jumps; these and their associated frequencies of occurance must be considered separately to arrive at a correct expression for Γ for the solvent atoms. We use the following notation taken from earlier papers on solute diffusion: an associated vacancy exchanges places with its solute atom w_2 times/sec, it exchanges places with a given one of the four sites which are nearest neighbours to both the vacancy and the solute w_1 times/sec and it jumps to a given one of the remaining seven of its nearest neighbour sites (i.e. dissociates) k_1 times/sec. The corresponding association frequency from a next nearest neighbour site of the solute to a nearest neighbour site is k_2. The frequency with which an unassociated vacancy jumps to another unassociated site is called w_0.

With this notation and the result (2.8) we can write down the number of solvent-vacancy exchanges/sec made by vacancies initially in positions nearest-neighbour to a solute atom;

$$12\,N_i \exp\left(-\frac{g_V + \Delta g}{kT}\right).(4w_1 + 7k_1). \quad . \quad . \quad . \quad . \quad (3.2)$$

We also want the number of association jumps which occur. Now, surrounding any solute atom there are 42 sites from which a nearest neighbour position can be reached in one jump; altogether there are 84 distinct jumps, each of frequency k_2. We want the number of impurity-vacancy pairs at these separations. Now the probability that any lattice site is occupied by a vacancy is n_V/N_s if no solute is in the surrounding nearest neighbour shell. Also the probability that any site is occupied by a solute atom is $N_i(1-p)/N_s$, if no vacancy is a nearest neighbour of that site. Hence the total number of solute-vacancy pairs at the separation from which an association jump can be made is

---

† This is the original paper on the topic; for a brief review of subsequent work see Lidiard (1958).

$$42\,N_i(1-p)\,n_V/N_s.$$

The total number of association jumps occurring per sec is likewise

$$84\,k_2\,N_i(1-p)\,n_V/N_s. \qquad (3.3)$$

The remaining 420 jumps possible from these 42 sites around each solute atom are w_0 jumps and we shall assume that these occur with the same frequency as in the pure solvent. Their contribution is

$$420\,w_0 N_i(1-p)n_V/N_s. \qquad (3.4)$$

So far we have accounted for $42N_i(1-p)n_V/N_s$ of the total of n_V free vacancies. The remainder,

$$n_V(1-42N_i(1-p)/N_s),$$

execute a total of

$$12w_0 n_V(1-42\,N_i(1-p)/N_s) \qquad (3.5)$$

jumps per sec. We may note that inclusion of terms (3.4) and (3.5) is only possible for solute concentrations less than about 2%; otherwise overlapping of the spheres of influence of different solute atoms becomes important. The total number of solvent atom jumps per sec is given by the sum of terms (3.2)–(3.5) with n_V given by (2.7), and Γ, the average solvent atom jump frequency, is obtained by dividing this sum by the number of solvent atoms present. To the first order in c the result is

$$\Gamma = 12w_0 \exp(-g_V/\boldsymbol{k}T)\left[1-18c+c\exp(-\Delta g/\boldsymbol{k}T)\left(\frac{4w_1+14k_1}{w_0}\right)\right] \qquad (3.6)$$

in which we have used the result that $k_2/k_1 = \exp(-\Delta g/\boldsymbol{k}T)$.

When now we wish to consider the diffusion coefficient of the solvent atoms it is necessary to include correlation effects. The simplest situation to handle is that where the solute atoms may be regarded as constituting a 'weak perturbation'; then none of the jump frequencies will be changed radically and correlation effects will be closely the same as in the pure solvent. Under these conditions we can go immediately from (3.6) to the equation

$$D_S(c) = D_S(0)\left[1-18c+c\exp(-\Delta g/\boldsymbol{k}T)\left(\frac{4w_1+14k_1}{w_0}\right)\right] \qquad (3.7)$$

in which $D_S(c)$ is the diffusion coefficient of the solvent in an alloy containing a concentration c of solute.

Equation (3.7) may be a reasonable starting point. We have at present little knowledge of the relative magnitudes of w_1, w_2, k_0 and w_0, but a 'weak perturbation', assumption seems a better approximation than a model of tightly bound solute-vacancy pairs (§ 6), so far as one is able to judge directly from the relative diffusion rates of solutes and of the solvent. Other possibilities will be noted later.

Equation (3.7) may be written

$$D_s(c) = D_s(0)\,(1+bc), \quad b = -18 + \frac{4(w_1 + 7k_1/2)}{w_0}\exp\left(-\frac{\Delta g}{\boldsymbol{k}T}\right). \qquad (3.8)$$

Now, this same model of the alloy yields the expressions

$$D_i = \frac{2s^2 w_2\,(w_1 + 7k_1/2)}{(w_1 + w_2 + 7k_1/2)}\exp\left(-\frac{g_{\mathrm{v}} + \Delta g}{\boldsymbol{k}T}\right) \quad . \quad . \quad . \quad (3.9)$$

for the solute ('impurity') diffusion coefficient and

$$D_s(0) = 2s^2 w_0 (9/11)\exp\left(-\frac{g_{\mathrm{v}}}{\boldsymbol{k}T}\right), \quad . \quad . \quad . \quad (3.10)$$

the 9/11 being an approximation to the correlation factor, f_0 (consistent with (3.9)) for solvent self-diffusion in the pure metal. The correlation factor for solute diffusion into pure solvent is the factor†

$$f_i \equiv (w_1 + 7k_1/2)/(w_1 + w_2 + 7k_1/2) \quad . \quad . \quad . \quad . \quad (3.11)$$

in (3.9) (LeClaire and Lidiard 1956); this is a quantity of interest to the electronic theory of solute diffusion since only if it is near to unity is the solute diffusion determined by w_2 alone, as often assumed. It is therefore interesting to note that eqns. (3.8), (3.9) and (3.10) allow us to write

$$f_i = 1 - \frac{4f_0}{(b+18)}\left(\frac{D_i}{D_{\mathrm{S}}(0)}\right). \quad . \quad . \quad . \quad . \quad . \quad (3.12)$$

We may note that this is consistent with the description of a weak perturbation, for as $D_i/D_{\mathrm{S}}(0) \to 1$ and $b \to 0$, then $f_i \to f_0 = 9/11$, as it must do. The expression for b corresponding to (3.12) is

$$b = -18 + \frac{36}{11(1-f_i)}\left(\frac{D_i}{D_{\mathrm{S}}(0)}\right). \quad . \quad . \quad . \quad . \quad (3.13)$$

A qualitative consideration of correlation effects in other than the 'weak perturbation' limit indicates that (3.12) changes mainly in that the 18 is reduced. For a number of solutes b is several times 18 and the results are not greatly affected.

§ 4. EXPERIMENTAL RESULTS FOR Ag ALLOYS

Experimental results for a number of Ag alloys are available. $D_{\mathrm{S}}(c)$ is often well represented by an exponential dependence exp (bc) rather than by the linear form (3.7); however, we are only interested in the limit of $c < 2\%$ and it is reasonable to assume that b in the exponential form has the same significance as here. Results for f_i calculated from (3.12) for 1000°K are given in the table, column *W.P.* The use of Manning's expression in place of (3.11) and the consistent assumption $k_2 = w_0$ decreases the values of f_i in the table only very slightly.

---

† A more accurate expression for f_i is available in the special case when $k_2 = w_0$ (Manning 1959).

Values of b and $D_i/D_s(0)$ for various solutes in Ag at 1000°K (as interpolated from experimental results) and the values of the solute atom correlation factor f_i as deduced in weak perturbation and tight-binding approximations

Solute	b	$D_i/D_s(0)$	f_i, $W.P$	f_i, $T.B$
Pd	$-8{\cdot}2^a$	$0{\cdot}123^b$	0·96	—
Cu	$10{\cdot}2^c$	$1{\cdot}25^d$	0·86	—
Cd	$6{\cdot}9^e$	$3{\cdot}67^c$	0·52	0·46
In	$12{\cdot}7^e$	$5{\cdot}35^e$	0·43	0·48
Tl	$36{\cdot}4^f$	$8{\cdot}39^f$	0·50	0·72
Ge	$32{\cdot}7^c$	$9{\cdot}51^f$	0·39	0·61
Pb	$86{\cdot}0^c$	$11{\cdot}1^c$	0·65	0·89
Sb	$51{\cdot}7^g$	$7{\cdot}65^h$	0·64	0·86

Sources of experimental data in this table :

(a) N. H. Nachtrieb, quoted by H. Reiss in *Phys. Rev.*, **113,** 1445 (1959).
(b) N. H. Nachtrieb, J. Petit and J. Wehrenberg, *J. chem. Phys.*, **26,** 106 (1957).
(c) R. E. Hoffman, D. Turnbull and E. W. Hart, *Acta Met.*, **3,** 417 (1958).
(d) A. Sawatsky and F. E. Jaumot ; quoted by R. E. Hoffman, *Acta Met.*, **6,** 95 (1958).
(e) A. H. Schoen, Ph.D. Thesis, University of Illinois (1958).
(f) R. E. Hoffman, *Acta Met.*, **6,** 95 (1958).
(g) E. Sonder, *Phys. Rev.*, **100,** 1662 (1955).
(h) E. Sonder, L. M. Slifkin and C. T. Tomizuka, *Phys. Rev.*, **93,** 970 (1954).

For the calculation of $D_i/D_s(0)$ we have used

$$D_s(0) = 0{\cdot}442 \exp\left(-\frac{44{\cdot}27 \text{ k cals}}{\boldsymbol{k}T}\right) \text{cm}^2/\text{sec}$$

as given by Schoen's analysis of the data of Slifkin, Sonder and Tomizuka.

§ 5. Discussion of Results in § 4

The correlation factor for solute diffusion in pure solvent, f_i, must by its definition lie between 0 and 1. It is encouraging that the values in the table all do lie within this range. It is encouraging also that the value for Cu in Ag, which we might expect to be a closely ideal system, is close to the value for Ag self-diffusion (i.e. 0·82 in the present approximation). There are indications that this is true also for Au in Ag (Slifkin, unpublished data). It is also worth drawing attention to the fact that none of the f_i values is small, and, although this is not a sensitive test of our 'weak perturbation' assumption, it is nevertheless consistent with it.

On the other hand, it must be pointed out that there exists the quite independent, and apparently direct, evidence of the isotope effect experiments for the diffusion of Cd and In in Ag which shows that the correlation factors for these solutes are small, i.e. that their diffusion is controlled by $(w_1+7k_1/2)$ and not by w_2 (Schoen 1958 a, Tharmalingam and Lidiard 1959). If these results are confirmed and extended to other elements we must infer from the table that a considerable part of b, i.e. of the enhancement of self-diffusion, is due to longer range effects than we have considered. Thus, while it appears from Schoen's work that the Overhauser type of theory cannot account for all the enhanced Ag diffusion caused by Cd and In solutes (Schoen 1958 b) it may account for part of it and so give lower f_i values than we have obtained here.

§ 6. COMPARISON WITH WORK OF HOFFMAN, TURNBULL AND HART AND WITH 'TIGHT-BINDING' MODEL

These authors (HTH) made the first quantitative application of the model described in this note to the problem of the enhancement of metallic self-diffusion by solutes. Not surprisingly, their result is similar in general form (see Hart *et al.* 1957). One obvious difference, though, is the occurrence of the number of nearest neighbours, 12, in place of the 18 in our eqn. (3.13). Thus their equation in our notation and for the f.c.c. lattice reads

$$b=-12+8\alpha_1\left(\frac{D_i}{D_s(0)}\right), \qquad . \quad . \quad . \quad . \quad . \quad (6.1)$$

in which α_1 is their quantity, "the number of effective solvent diffusion jumps per solvent atom while in the first co-ordination shell of the solute". The 12 in eqn. (6.1) arises in the HTH treatment through the use of eqn. (2.9) and the assumption that this gives the fraction of time that a given solvent atom diffuses with diffusion coefficient $D_s(0)$. The two treatments come closest to formal similarity if we take $k_2=w_0$, i.e. the assumption of very short range of interaction which is sometimes made. Terms (3.3) and (3.4) may then be taken together and the constant term in b then becomes -11 instead of -18 as in (3.8) and (3.13). The remaining difference of 1 is due to an apparent neglect by HTH of the fact, included in (3.6), that the molar fraction of solvent is $1-c$ and not 1. Actually such a comparison is rather forced since the HTH treatment, although it can be said to include the association jumps (if $k_2=w_0$), does not explicitly include the dissociation jumps (k_1). In fact if $k_2=w_0$ then $k_1 \exp(-\Delta g/\boldsymbol{k}T)$ also equals w_0 and in place of (3.8) it would be consistent to write

$$b=-4+\frac{4w_1}{w_0}\exp\left(-\frac{\Delta g}{\boldsymbol{k}T}\right). \qquad . \quad . \quad . \quad . \quad . \quad . \quad (6.2)$$

The real point of alternatives such as these must however lie in the correlation effects. The correlations between subsequent jumps of a solvent atom and a prior jump are unlikely to be very different from those in the pure lattice if the prior jump is either a k_2 or a k_1 jump, particularly if $k_2=w_0$†. On the other hand, if the prior jump is a w_1-jump then the correlation effects may be different from those in the pure lattice especially when $w_2 \ll w_1$. If we introduce a different correlation factor for the w_1-jumps we must replace (6.2) by

---

† Dr. J. R. Manning in a private communication reports that this is confirmed by calculation.

$$b = -4 + \frac{4w_1 f_1}{w_0 f_0} \exp\left(-\frac{\Delta g}{\boldsymbol{k}T}\right), \quad (k_2 = w_0) \quad . \quad . \quad . \quad (6.3)$$

in which f_0 is the correlation factor for the pure solvent metal $(=0{\cdot}78$ accurately); the second correlation factor $f_1 \equiv f_1(w_2/w_1)$ is for an initial jump w_1 and has been calculated by Compaan and Haven (1956) and, more approximately, by Reiss (1959). Equation (6.3) and the corresponding expression

$$b = -4 + \frac{4f_1}{(1-f_i)}\left(\frac{D_i}{D_S(0)}\right), \quad . \quad . \quad . \quad . \quad . \quad (6.4)$$

with

$$f_i = w_1/(w_1 + w_2), \quad . \quad . \quad . \quad . \quad . \quad . \quad (6.5)$$

may be regarded as reasonable approximations to the 'tight-binding' limit, i.e., the opposite limit to (3.8) and (3.13). Owing to present limited knowledge of the function $f_1(w_2/w_1)$ solutions of (6.4) and (6.5) must be obtained by graphical interpolation between the values given by Compaan and Havan (1956). This yields the f_1 values given in the table under the coulmn headed T.B. (the second decimal figure is uncertain). For Cd and In the figures are little altered from those obtained in the weak perturbation limit; for the elements Tl–Sb they are increased by about 0·2. These changes come primarily from the incorporation into the equations of f_1, the values of which are several times less than the 9/11 assumed in the weak perturbation treatment. This means that in order to give the same observed effects it is necessary to have larger ratios of w_1/w_2 than are obtained if we use eqn. (3.8) (cf. the product $w_1 f_1$ which occurs in (6.3)). This in turn leads to larger values for f_i.

In a recent private communication to the author Dr. J. R. Manning reports a more extended discussion of the model with $k_2 = w_0$. He does not neglect k_1 in comparison with w_1 and w_2 as we have done. In addition he uses a more accurate expression for f_i (Manning 1959) and develops expressions for f_1 as function of w_1/k_1 and w_2/k_1. Experimental data on b and $D_i/D_S(0)$ is then used to infer w_1/k_1 and w_2/k_1 and hence f_i. The inferred values of w_1/k_1 and w_2/k_1 are large compared to unity and the f_i values agree well with those in the table, column T.B. These results may mean that more reliance should be placed on the T.B. values. However the inference of separate values for w_1/k_1 and w_2/k_1 is only possible on account of the assumption that $k_2 = w_0$; the sensitivity of the analysis to this assumption is not known.

§ 7. CONCLUSION

The table shows that the inferred correlation factors are not highly sensitive to the alternative mathematical assumptions which we have made about relative jump frequencies entering into this problem. In particular the values for Cd and In seem to be firm. These values are however in conflict with the much lower values demanded by Schoen's isotope effect experiments. The inference may be that the present model is too simplified to deal with the problem of solute enhanced diffusion and that effects of longer range must be included. However, we emphasise that the analysis presented here is perfectly consistent considered on its own, and that any such inference rests entirely on the isotope effect results for Cd and In in Ag. It would clearly be of interest to have these measurements extended to other solutes.

ACKNOWLEDGMENTS

The author is greatly indebted to Dr. J. R. Manning for stimulating correspondence and to Mr. A. D. LeClaire for his comments on the manuscript.

REFERENCES

BARDEEN, J., and HERRING, C., 1952, *Imperfections in Nearly Perfect Crystals* (New York : Wiley), p. 261.

CHANDRASEKHAR, S., 1943, *Rev. mod. Phys.*, **15,** 1.

COMPAAN, K., and HAVEN, Y., 1956, *Trans. Faraday Soc.*, **52,** 786.

HART, E. W., HOFFMAN, R. E., and TURNBULL, D., 1957, *Acta Met.*, **5,** 74.

HOFFMAN, R. E., 1958, *Acta Met.*, **6,** 95.

HOFFMAN, R. E., TURNBULL, D., and HART, E. W., 1955, *Acta Met.*, **3,** 417.

LAZARUS, D., 1955, *Impurities and Imperfections* (Cleveland : American Society of Metals), p. 107.

LECLAIRE, A. D., and LIDIARD, A. B., 1956, *Phil. Mag.*, **1,** 518.

LIDIARD, A. B., 1958, *Nuovo Cim.*, Suppl., **7,** 620.

LOMER, W. M., 1958, *Symposium on Vacancies and other Point Defects in Metals and Alloys* (London : Institute of Metals), p. 79.

MANNING, J. R., 1959, *Phys. Rev.*, **116,** 819.

OVERHAUSER, A. W., 1953, *Phys. Rev.*, **90,** 313.

REISS, H., 1959, *Phys. Rev.*, **113,** 1445.

SCHOEN, A. H., 1958 a, *Phys. Rev. Letters*, **1,** 138 ; 1958 b, Ph.D. Thesis, University of Illinois.

SEITZ, F., 1950, *Acta Cryst.*, **3,** 355.

Optical Model Analysis of Nuclear Scattering†

By B. Buck‡, R. N. Maddison and P. E. Hodgson
Clarendon Laboratory, Oxford

[Received June 15, 1960]

Abstract

The mathematical methods used in a calculation of nuclear interactions by the optical model are described, and the most efficient way of programming the calculation for an electronic computer investigated.

§ 1. General Formulation

When a nucleon or group of nucleons interacts with a nucleus, the behaviour of the system is determined by all the possible interactions between the nucleons present. This is very difficult to handle mathematically, so the optical model replaces all these separate interactions by a two-body interaction between the incident particle and the target nucleus of the form (Bjorklund and Fernbach 1958)

$$V(r) = V_{\mathrm{c}}(r) + Uf(r) + iWg(r) + (U_{\mathrm{S}} + iW_{\mathrm{S}})h(r)\,\boldsymbol{l}\,.\,\boldsymbol{\sigma} \qquad . \quad . \quad (1)$$

where r is the separation of the two particles, and U, W, U_{S} and W_{S} are the real and imaginary parts of the central and spin-dependent potentials respectively. V_{c} is the Coulomb potential, $f(r)$, $g(r)$ and $h(r)$ are functions giving the radial variations of the potentials (cf. § 4). This is equivalent to replacing the target nucleus by a potential well having both refracting and absorbing parts. The refracting potential U elastically scatters the incident particles, and the absorbing potential W takes account of all the inelastic processes, including inelastic scattering and absorption. The spin-dependent term given above is appropriate for the scattering of spin $\frac{1}{2}$ particles by spin 0 nuclei; for the scattering of particles of zero spin there is of course no spin-dependent term, while for the scattering of particles of higher spins more complex forms are required. In all optical model calculations it is usual to take the spin of the target nucleus to be zero.

To calculate the observable cross sections for two particles interacting through the above potential, Schrodinger's equation is applied to the whole system

$$\frac{\hbar^2}{2\mu}\nabla^2\Psi + (E - V)\Psi = 0 \qquad . \quad . \quad . \quad . \quad . \quad . \quad (2)$$

where E is the centre-of-mass energy.

---

† Communicated by the Authors.

‡ Now at Oak Ridge National Laboratory, Tennessee, U.S.A.

If the total wave function Ψ is expanded in spherical harmonies

$$\Psi=\sum_{jlm}\frac{U_{jl}(r)}{r}\sum_{\mu}C_{m\lambda\mu}^{\ jls}Y_l^{\lambda}(\theta,\phi)\chi_s^{\mu} \quad . \quad . \quad . \quad . \quad . \quad . \quad . \qquad (3)$$

we obtain a series of equations for each radial wave function. The spin of the incident particle can couple in two ways to the orbital angular momentum l to give the total angular momentum $j=l\pm\frac{1}{2}$, and the eigenvalues of $\boldsymbol{l}.\boldsymbol{\sigma}$ corresponding to these two spin orientations are l and $-(l+1)$. The corresponding radial wave functions $U_l^+(r)$ and $U_l^-(r)$ satisfy the equations

$$\frac{d^2U_l^+(\rho)}{d\rho^2}+\left[1-\frac{V_c}{E}-\frac{Uf(\rho)+iWg(\rho)}{E}\right.$$
$$\left.-\frac{l(U_s+iW_s)h(\rho)}{E}-\frac{l(l+1)}{\rho^2}\right]U_l^+(\rho)=0, \quad . \quad . \quad . \qquad (4a)$$

$$\frac{d^2U_l^-(\rho)}{d\rho^2}+\left[1-\frac{V_c}{E}-\frac{Uf(\rho)+iWg(\rho)}{E}\right.$$
$$\left.+\frac{(l+1)(U_s+iW_s)h(\rho)}{E}-\frac{l(l+1)}{\rho^2}\right]U_l^-(\rho)=0 \quad . \quad . \quad . \qquad (4b)$$

where $\rho=kr$, k being the wave number $k=\sqrt{(2\mu E)}/\hbar$ where μ is the reduced mass of the incident particle, $\mu=A_{\rm I}/(A_{\rm I}+A_{\rm T})$, $A_{\rm I}$ and $A_{\rm T}$ being the masses of the incident and target particles in a.m.u. These radial wave functions are zero at the origin and beyond the nuclear field tend asymptotically to the forms

$$U_l^{\pm}(\rho)=F_l(\rho)+iG_l(\rho)+S_l^{\pm}[F_l(\rho)-iG_l(\rho)] \quad . \quad . \quad . \quad . \qquad (5)$$

where the $S_l^{\pm}=\exp(2i\delta_l)$ are the (complex) elements of the scattering matrix, and $F_l(\rho)$ and $G_l(\rho)$ are regular and irregular solutions of the eqn.(4) without the nuclear terms. These functions are taken to have the asymptotic forms

$$F_l(\rho)\xrightarrow[\rho\to\infty]{}\sin[\rho-\gamma\ln 2\rho-\tfrac{1}{2}l\pi+\sigma_l], \quad . \quad . \quad . \quad . \quad . \qquad (5a)$$

$$G_l(\rho)\xrightarrow[\rho\to\infty]{}\cos[\rho-\gamma\ln 2\rho-\tfrac{1}{2}l\pi+\sigma_l]. \quad . \quad . \quad . \quad . \quad . \qquad (5b)$$

The non spin-flip and spin-flip scattering amplitudes are then

$$A(\theta)=f_c(\theta)+\frac{1}{2ik}\sum_{l=0}^{\infty}\{(l+1)S_l^{+}+lS_l^{-}-(2l+1)\}\exp(2i\sigma_l)P_l(\cos\theta) \quad (6a)$$

$$B(\theta)=\frac{1}{2ik}\sum_{l=0}^{\infty}\{S_l^{+}-S_l^{-}\}\exp(2i\sigma_l)P_l^1(\cos\theta) \quad . \quad . \quad . \quad . \quad . \quad . \quad . \qquad (6b)$$

where $f_c(\theta)$ is the Coulomb scattering amplitude

$$f_c(\theta)=-\frac{\gamma}{2k}\operatorname{cosec}^2\frac{\theta}{2}\exp[2i\sigma_0-2i\gamma\ln\sin\theta/2] \quad . \quad . \quad . \qquad (7)$$

where

$$\gamma=\frac{\mu Z_{\rm I}Z_{\rm T}e^2}{k\hbar^2},$$

$Z_{\rm I}$ and $Z_{\rm T}$ being the charges of the incident and target nuclei, and σ_l is the Coulomb phase shift for the lth partial wave.

The observable quantities may be expressed in terms of the scattering amplitudes. The differential cross section for elastic scattering is given by

$$\sigma(\theta)=|A|^2+|B|^2 \quad . \quad . \quad . \quad . \quad . \quad . \quad . \quad . \quad (8)$$

and the polarization by

$$P(\theta)=\frac{2\ \mathrm{Im}\ AB^*}{|A|^2+|B|^2}\boldsymbol{n} \quad . \quad . \quad . \quad . \quad . \quad . \quad . \quad . \quad (9)$$

where $\boldsymbol{n}=\boldsymbol{k}_i\times\boldsymbol{k}\ /|\boldsymbol{k}_i\times\boldsymbol{k}_f|$.

The total absorption cross section is given by

$$\sigma_A=\frac{\pi}{k^2}\sum_{l=0}^{\infty}\{(l+1)(1-|S_l^+|^2)+l(1-|S_l^-|^2)\}. \quad . \quad . \quad . \quad (10)$$

If the incident particles are uncharged, V_{c}, $f_{\mathrm{c}}(\theta)$ and σ_l are all zero, and the total elastic cross section is finite

$$\sigma_E=\frac{\pi}{k^2}\sum_{l=0}^{\infty}\{(l+1)|1-S_l^+|^2+l|1-S_l^-|^2\}. \quad . \quad . \quad . \quad . \quad (11)$$

The total cross section is

$$\sigma_T=\frac{2\pi}{k^2}\sum_{l=0}^{\infty}\{(l+1)(1+\mathrm{Re}\,S_l^+)+l(1-\mathrm{Re}\,S_l^-)\}. \quad . \quad . \quad . \quad (12)$$

In practice, partial waves with l greater than some value $l_{\max}$ do not contribute significantly to these summations and so they may be neglected.

§ 2. METHOD OF SOLUTION

The essential part of the calculation is the numerical integration of the radial wave eqns. (4) from the origin out to a distance ρ_M where the nuclear field is negligible. The wave function obtained by this integration of the internal equation must join smoothly to the external solution (5). Thus, if f_l is the logarithmic derivative of the internal wave function at ρ_M,

$$f_l^{\pm}=\left(\frac{F_l'(\rho)+iG_l'(\rho)+S_l^{\pm}[F_l'(\rho)-iG_l'(\rho)]}{F_l(\rho)+iG_l(\rho)+S_l^{\pm}[F_l(\rho)-iG_l(\rho)]}\right)_{\rho=\rho_M} \quad . \quad . \quad . \quad (13)$$

Since $f_l^{\pm}$ is determined from the internal integration, and the F's and G's may be calculated as described below, this determines the $S_l^{\pm}$, and hence the observable quantities by the relations (6)–(12).

The internal integration was initially coded for the Runge–Kutta–Gill method, since this is available as a subroutine on the computer used. Advantage can, however, be taken of the absence of first derivatives in (4) to use the Fox–Goodwin method 7, and this is up to ten times faster. In the Runge–Kutta method the value of the function and its derivative is required at one point beyond the origin and in the Fox–Goodwin method the values of the function at two points beyond the origin are required before the numerical integration can begin. If these points are taken close to the origin a series solution of (4) may be obtained for small ρ, and very few terms suffice to give accurate starting values of the wave function and its derivative.

In the external region, the wave eqn. (4) reduces to

$$\frac{d^2U_l}{d\rho^2}+\left[1-\frac{2\gamma}{\rho}-\frac{l(l+1)}{\rho^2}\right]U_l=0. \quad . \quad . \quad . \quad . \quad . \quad . \quad (14)$$

For $\gamma \neq 0$ its solutions are the regular and irregular Coulomb wave functions $F_l(\rho)$ and $G_l(\rho)$. The F_l may be readily calculated by several methods among which the asymptotic series expansion, the Shepansky–Butler series and Miller's method (Stegun and Abramowitz 1955) were investigated. Miller's method was chosen for its simplicity and speed. This method sets $F_{l+1}(\rho)=0$, $\alpha F_l(\rho)=\epsilon$, where l is an integer $>l_{\max}$ ($l=60$ was used here), α is a constant to be determined, and ϵ a very small number. Using the recurrence relation

$$\frac{[\gamma^2+(l+1)^2]^{1/2}}{l+1} F_{l+1}(\rho) + \frac{[\gamma^2+l^2]^{1/2}}{l} F_{l-1}(\rho) = (2l+1)\left[\frac{\gamma}{l(l+1)} + \frac{1}{\rho}\right] F_l(\rho) \quad . \; . \; . \quad (15)$$

all the $\alpha F_l(\rho)$'s down to $\alpha F_0(\rho)$ may be calculated. The constant α was found from the Wronskian

$$F_0'(\rho)G_0(\rho) - F_0(\rho)G_0'(\rho) = 1 \quad . \; . \; . \; . \; . \; . \quad (16)$$

where $F_0'(\rho)$ was found from the recurrence relation

$$\left[\frac{\gamma}{l+1} + \frac{l+1}{\rho}\right] F_l(\rho) - F_l'(\rho) = \frac{[\gamma^2+(l+1)^2]^{1/2}}{l+1} F_{l+1}(\rho) \qquad (17)$$

and $G_0(\rho)$ and $G_0'(\rho)$ were calculated as described below.

The irregular functions were evaluated using the expression (Froeberg 1955)

$$\left.\begin{aligned} G_0(\rho) &= s\cos(-\gamma\ln 2\rho+\rho+\sigma_0) - t\sin(-\gamma\ln 2\rho+\rho+\sigma_0), \\ G_0'(\rho) &= S\cos(-\gamma\ln 2\rho+\rho+\sigma_0) - T\sin(-\gamma\ln 2\rho+\rho+\sigma_0), \end{aligned}\right\} \quad . \quad (18)$$

where

$$s = \sum_{n=0}^{25} s_n, \quad t = \sum_{n=0}^{25} t_n; \quad S = \sum_{n=0}^{25} S_n, \quad T = \sum_{n=0}^{25} T_n.$$

The number of terms in these sums was found by experience to be adequate, and the individual terms were calculated from the recurrence relations

$$\left.\begin{aligned} s_{n+1} &= \frac{(2n+1)\gamma}{2\rho(n+1)} s_n - \frac{\gamma^2-n(n+1)}{2\rho(n+1)} t_n; \\ t_{n+1} &= \frac{(2n+1)\gamma}{2\rho(n+1)} t_n + \frac{\gamma^2-n(n+1)}{2\rho(n+1)} s_n \\ S_{n+1} &= \frac{(2n+1)\gamma}{2\rho(n+1)} S_n - \frac{\gamma^2-n(n+1)}{2\rho(n+1)} T_n - \frac{s_{n+1}}{\rho}; \\ T_{n+1} &= \frac{(2n+1)\gamma}{2\rho(n+1)} T_n + \frac{\gamma^2-n(n+1)}{2\rho(n+1)} S_n - \frac{t_{n+1}}{\rho}. \end{aligned}\right\} \quad . \; . \quad (19)$$

and the initial values

$$s_0=1, \quad s_1=\frac{\gamma}{2\rho}; \quad S_0=0, \quad S_1=\frac{\gamma^3-\gamma^2}{2\rho^2}-\frac{\gamma^2}{2\rho};$$

$$t_0=0, \quad t_1=\frac{\gamma^2}{2\rho}; \quad T_0=1-\frac{\gamma}{\rho}, \quad T_1=-\frac{\gamma^2}{\rho^2}+\frac{\gamma}{2\rho}.$$

The summations satisfy the relation

$$sT - St = 1. \qquad (20)$$

The convergence of these series improves as ρ increases, and to obtain accurate results a value of ρ substantially greater than ρ_M must be used. To ensure accuracy, ρ was first set to a suitable starting value, and the series summed. If the relation (20) was satisfied to one part in 10^4, the values were accepted; if not, ρ was increased until it was.

The values of $G_0(\rho_M)$ and $G_0'(\rho_M)$ were obtained from these $G_0(\rho)$, $G_0'(\rho)$, where $\rho > \rho_M$, by integrating the eqn. (14) inwards numerically. The $G_l(\rho_M)$ and $G_l'(\rho_M)$ were then found from (17) and (15).

The relations (15) and (17) are satisfied by both the F's and the G's. They may only be used downwards in l for the F's and upwards in l for the G's, when $l > \rho$; otherwise instabilities develop and all accuracy is lost (cf. Hartree 1952). Likewise, eqn. (14) may only be integrated outwards for the F's and inwards for the G's in the unstable regions.

The Coulomb phase shifts $\sigma_l(\gamma)$ were calculated from the asymptotic series expansion for large l ($l = 50$ was used)

$$\begin{aligned}\sigma_l(\gamma) &= \alpha(l+\tfrac{1}{2}) + \gamma[\ln\beta - 1]\\ &\quad + \frac{1}{\beta}\left[-\frac{\sin\alpha}{12} + \frac{\sin 3\alpha}{360\beta^2} - \frac{\sin 5\alpha}{1260\beta^4} + \frac{\sin 7\alpha}{1680\beta^6} - \frac{\sin 9\alpha}{1188\beta^8} + \dots\right] \qquad (21)\end{aligned}$$

where

$$\alpha = \tan^{-1}[\gamma/(l+1)], \quad \beta = [\gamma^2 + (l+1)^2]^{1/2}$$

and the recurrence relation

$$\sigma_l(\gamma) = \sigma_{l+1}(\gamma) - \tan^{-1}[\gamma/(l+1)]. \qquad (22)$$

If $\gamma = 0$, the solutions of (14) are spherical Bessel and Neumann functions

$$F_l(\rho) = \rho j_l(\rho), \quad G_l(\rho) = -\rho n_l(\rho). \qquad (23)$$

The F's were calculated by Miller's method and the G's, using (19), with the initial values

$$j_0(\rho) = \frac{\sin\rho}{\rho}, \qquad j_1(\rho) = \frac{\sin\rho}{\rho^2} - \frac{\cos\rho}{\rho};$$

$$n_0(\rho) = -\frac{\cos\rho}{\rho}, \qquad n_1(\rho) = -\frac{\cos\rho}{\rho^2} - \frac{\cos\rho}{\rho}.$$

The F's and G's and their derivatives were required to satisfy the Wronskian

$$F_l'(\rho)G_l(\rho) - F_l(\rho)G_l'(\rho) = 1 \qquad (24)$$

for all l to two parts in 10^5.

§ 3. Choice of Parameters

Four parameters determine the numerical part of the calculation: (*a*) the matching radius ρ_M, (*b*) the number of steps in the Coulomb integration N_c, (*c*) the number of steps in the nuclear integration N_n, and (*d*) the number of partial waves ($l_{\max} + 1$). Within certain limits, the larger these numbers are the more accurate the final result, but the longer the time of computation. It is therefore necessary to choose them to minimize the time consistent with the desired accuracy of the final results.

Since the Coulomb integration is done only once, N_c can be chosen generously without substantially affecting the total time. This leaves ρ_M, N_n and l_{max} to be studied in detail. In general, such parameters can either be chosen once and for all, or calculated for each run by some empirical formula, or fixed automatically to satisfy some pre-determined accuracy criterion. The latter procedure is inherently the most satisfactory, but is only convenient for l_{max} in the present work. The nuclear integrations were performed for increasing l-values, until $1-|ReS_l|$ for the last partial wave became less than some small number ϵ. Such an automatic procedure would be possible to fix ρ_M and N_n also, but it is not efficient as the nuclear integrations would have to be done again and again for increasing ρ_M and N_n until some pre-set condition was satisfied. It is easier to use an empirical formula for them.

The best choice of ρ_M and N_n was investigated by calculating the scattering of 14 Mev neutrons by aluminium for a range of values, and recording the accuracy with which sample cross-sections and polarizations were determined. For this investigation, l_{max} was chosen considerably larger than usual. Some typical results are shown in tables 1–3. Since most of the computation time is taken up by the numerical integration, and this is proportional to $N_n l_{max}$, it is apparent from the table that, adequate accuracy for most purposes can be obtained by choosing $C=7$ where

$$\rho_M=\rho_R+C\alpha \qquad . \quad . \quad . \quad . \quad . \quad . \quad . \quad . \quad (25)$$

where ρ_R and α are the nuclear radius and diffuseness in ρ units, $\rho_R=kR$, $\alpha=ka$.

The best value of ρ_M chosen in this way is very insensitive to E and A, so the above relation was written into the programme. The best values of N_n depend on E and A and it was found adequate to have ten steps per unit of ρ.

It would be possible to use varying step lengths for the numerical integration, the shorter steps where the wave function changes rapidly and the longer steps elsewhere. This would reduce the calculation time, but as the improvement is marginal it has not been done. A value of $\epsilon=0{\cdot}0001$ was found to give accuracies at least as good as the best in tables 1–3.

Combinations of the physical constants occur in three places in the calculation:

the Coulomb constant

$$\gamma=\frac{\mu Z_I Z_T e^2}{k\hbar^2}=0{\cdot}157454 Z_I Z_T (A_I/E_{lab})^{1/2} \qquad . \quad . \quad . \quad . \quad (26)$$

where E_{lab} is in Mev.

the wave number

$$k=0{\cdot}218728\,(\mu E_{CM})^{1/2} \qquad . \quad . \quad . \quad . \quad . \quad . \quad (27)$$

and the coefficient of the spin–orbit term (see § 4).

$$\left(\frac{\hbar}{2Mc}\right)^2 = 0{\cdot}011057 \times 10^{-26}\,\text{cm}^2 \quad . \; . \; . \; . \; . \quad (28)$$

Table 1. Percentage error in calculation of total cross section for 14 MeV neutrons on aluminium for various C and N_n

C	Number of integration steps N_n			
	15	20	25	30
6	0·05	0·03	0·03	0·03
7	0·06	0·02	0·02	0·02
8	0·07	0·02	0·011	0·008
9	0·11	0·02	0·008	0·003

Table 2. As table 1 for differential cross section at 0°

C	Number of integration steps N_n			
	15	20	25	30
6	0·66	0·47	0·44	0·43
7	0·60	0·25	0·19	0·18
8	0·84	0·18	0·09	0·08
9	1·35	0·20	0·07	0·04

Table 3. As table 1 for polarization at 120°

C	Number of integration steps N_n			
	15	20	25	30
6	−3·80	−0·76	−0·20	−0·03
7	−6·01	−0·82	+0·03	+0·27
8	−10·5	−3·09	−0·39	−0·04
9	−17·9	−4·20	−0·83	−0·32

The programme was arranged to read the parameters of each calculation from a separate data tape. The parameters were A_T, A_I, Z_T, Z_I, the masses (in a.m.u.) and charges of the target and incident particles respectively, the energy E of the incident particle in the laboratory system in MeV, the central and spin–orbit potentials (in MeV) and the parameters of their form factors (in 10^{-13} cm), the Coulomb radius r_c, and the angular range required in the output. A second data tape provides the experimental data with which the calculation is to be compared.

The output consists of all the input numbers, the range of the nuclear integrations, k, γ, the $S_l^{\pm}$, the $\sigma_A{}^l$ and σ_A (also $\sigma_E{}^l$, σ_E, σ_{T} for $Z_{\mathrm{I}}=0$) $d\sigma/d\Omega$ and $\mathbf{P}$ for the angular range specified, and Δ_σ and Δ_P for each point of the experimental distribution, and their totals.

The time in seconds for a calculation on the Ferranti Mercury computer is approximately

$$T \approx 0{\cdot}5\, E_{\mathrm{lab}}\, R^2 + 20 \qquad \ldots \ldots \qquad (29)$$

where R is the nuclear radius in fermis. This is halved if there is no spin–orbit potential.

§ 4. RADIAL VARIATION OF THE COULOMB AND NUCLEAR POTENTIALS

The Coulomb potential was taken to be that due to a charged sphere of radius $R_{\mathrm{c}} = r_{\mathrm{c}} A^{1/3}$

$$\begin{aligned} V_{\mathrm{c}} &= \frac{Z_{\mathrm{I}} Z_{\mathrm{T}} e^2}{2R_{\mathrm{c}}}(3 - r^2/R_{\mathrm{c}}{}^2) \quad \text{for} \quad r < R_{\mathrm{c}} \\ &= \frac{Z_{\mathrm{I}} Z_{\mathrm{T}} e^2}{r} \qquad\qquad\qquad \text{for} \quad r > R_{\mathrm{c}}. \qquad \ldots \qquad (30) \end{aligned}$$

It would be more accurate to use the potential due to a charged sphere with a diffuseness corresponding to that of the nuclear potential. This would substantially increase the computation time, without significantly affecting the results. The interaction is insensitive to the radial form of the potential and the form (30) is adequate for all practical purposes. This is shown by the comparison in tables 4 and 6 between two calculations with identical parameters except for r_{c}.

The nuclear potentials can be represented by a number of form factors all having a rapid fall-off beyond the nuclear surface. Those used in the present programme were the Saxon–Woods form

$$f(r) = \frac{1}{1 + \exp\left(\dfrac{r-R}{a}\right)} \qquad \ldots \ldots \qquad (31)$$

where $R = r_0 A^{1/3}$ is the nuclear radius and a the diffuseness of the nuclear surface, and the Gaussian form

$$g(r) = \exp\left[-\left(\frac{r-R}{a}\right)^2\right]. \qquad \ldots \ldots \qquad (32)$$

The form factor for spin-orbit potential, by analogy with the Thomas term in atoms, was taken to be

$$h(r) = -\left(\frac{\hbar}{2Mc}\right)^2 \cdot \frac{1}{r} \cdot \frac{df(r)}{dr}. \qquad \ldots \ldots \qquad (33)$$

The factor $(\hbar/2Mc)^2$, the square of half the Compton wavelength of the proton, is introduced simply to keep $h(r)$ dimensionless. Some authors use $(\hbar/m_\pi c)^2$, where m_π is the pion mass. The corresponding potentials must then be divided by $(2M/m_\pi)^2 = 180{\cdot}59$. The negative sign is introduced to keep $h(r)$ positive.

The programme was arranged to use the Saxon–Woods form for U, either the Saxon–Woods or the Gaussian for W, and the form given by (33) for the spin-orbit potentials.

The choice of a definite ρ_M for matching the internal and the external wave function is equivalent to cutting off the potential at that radius. The problem is then solved exactly for the cut-off potential. Since little is known about the nuclear field at such distances from the nucleus, nothing is lost by this procedure.

Table 4. Effect of altering Coulomb field. Calculation with same parameters as table 6 but with $r_c = 1{\cdot}4$ F ($\text{F} \equiv 10^{-13}$ cm)

θ_{CM}	$d\sigma/d\Omega$	P
20	2·818, 3	−0·0584
40	1·827, 2	0·0490
60	2·067, 1	0·2404
80	1·597, 1	−0·0965
120	3·442, 0	−0·7532
160	2·257, 0	0·6367
σ_R	1055·8 mB	

§ 5. PROGRAMME CHECKS

With a calculation of this complexity it is essential to check that no analytical or programming errors have been made. In the present case there are no simple limiting cases that could be used, and the whole calculation would take a prohibitively long time to check on a desk computer. The best check is to compare the results of some trial calculations with that of similar runs with exactly the same initial parameters using another programme written independently for another computer. Through the courtesy of Professor M. A. Melkanoff such runs have been made, and the results are given in tables 5 and 6. The agreement is generally satisfactory, and the remaining small discrepancies may be accounted for by slightly different choices of the numerical parameters in the programmes, and to the accumulation of small rounding errors. The agreement is sufficiently good for comparison with experimental data.

§ 6. COMPARISON WITH EXPERIMENTAL DATA

It is frequently necessary to compare the calculated angular distributions and polarizations with experimental data, and it is convenient to incorporate facilities for doing this into the programme. The experimental data forms part of the input, and when the rest of the calculation is complete, the values of

$$\Delta_\sigma = \sum \left[\frac{\left(\frac{d\sigma(\theta)}{d\Omega}\right)_T - \left(\frac{d\sigma(\theta)}{d\Omega}\right)_E}{\delta\left(\frac{d\sigma(\theta)}{d\Omega}\right)_E} \right]^2 \quad \text{and} \quad \Delta_P = \sum \left(\frac{P_T(\theta) - P_E(\theta)}{\delta P_E(\theta)}\right)^2 \tag{34}$$

where the suffix E denotes experimental data, are calculated for each experimental point and included in the output.

Table 5. Comparison of present programme with that of Melkanoff for 17 MeV protons on gold, with $U = -48$ MeV, $W = -8$ MeV, $r_0 = 1{\cdot}3$ F, $r_C = 1{\cdot}3$ F, $a = 0{\cdot}5$ F, $A_I = 1$, $A_T = 197$. Both form factors are Saxon–Woods, and there is no spin–orbit potential. All cross sections are in millibarns per steradian, and are written in floating point form

θ_{CM}	$d\sigma/d\Omega$ (Melkanoff)	$d\sigma/d\Omega$ (present work)
20	3·202, 4	3·203, 4
40	1·549, 3	1·549, 3
60	2·951, 2	2·951, 2
80	6·728, 1	7·624, 1
120	1·460, 1	1·458, 1
160	7·825, 0	7·807, 1
σ_R	984·7 mB	985·2 mB

Table 6. Comparison of present programme with that of Melkanoff for 17 MeV, protons on copper, with $U = -46$ MeV, $W = -9$ MeV, $U_S = -1444$ MeV, $W_S = 361$ MeV, $r_0 = 1{\cdot}33$ F, $r_C = 1{\cdot}33$ F, $a = 0{\cdot}48$ F, $A_I = 1$, $A_T = 64$. (In all these check calculations Melkanoff's values of the constants in eqns. (26) and (27) were used. These are 0·158051 and 0·219438 respectively)

θ	$d\sigma/d\Omega$ (Melkanoff)	$d\sigma/d\Omega$ (present work)	P (Melkanoff)	P (present work)
20	2·807, 3	2·809, 3	−0·0590	−0·0578
40	1·819, 2	1·822, 2	0·0425	0·0426
60	2·140, 1	2·136, 1	0·2614	0·2623
80	1·563, 1	1·567, 1	−0·1213	−0·1168
120	3·396, 0	3·389, 0	−0·7876	−0·7811
160	2·310, 0	2·310, 0	0·6727	0·6646
σ_R	1054·7 mB	1055·0 mB		

Experimental differential cross sections are often subject to a larger absolute than relative error. If the incident particle is charged, and the cross-sections are available to small angles, it is then desirable to normalize the experimental cross-sections to the theoretical in this region. A facility to do this for a specified number of experimental points was incorporated in the programme.

ACKNOWLEDGMENTS

We would like to thank Professor D. H. Wilkinson, F.R.S., for suggesting and guiding this work, Professors F. Bjorklund, A. E. Glassgold and M. A. Melkanoff who have communicated details of their own optical model work, the Director of the Oxford University Computing Laboratory for the use of the computer, Miss N. Reynolds, Miss S. Tilley and the staff of the Computing Laboratory for their assistance, and the D.S.I.R. for its support.

Note added in proof.—Professor M. A. Melkanoff has now published (University of California Press, 1960) a detailed account of his own calculations, with full derivations of the equations used in the above paper.

REFERENCES

BJORKLUND, F., and FERNBACH, S., 1958, *Phys. Rev.*, **109,** 1295.
FOX, L., and GOODWIN, E. T., 1949, *Proc. Camb. phil. Soc.*, **45,** 373.
FROEBERG, C. E., 1955, *Rev. mod. Phys.*, **27,** 399.
HARTREE, D. R., 1952, *Numerical Analysis* (Oxford: University Press), p. 246.
HILDEBRAND, F. B., 1956, *Introduction to Numerical Analysis* (McGraw-Hill), p. 233.
SHEPANSKY, J. R., and BUTLER, S. T., 1956, *Nucl. Phys.*, **1,** 313.
STEGUN, I., and ABRAMOWITZ, M., 1955, *Phys. Rev.*, **98,** 1851.

CORRESPONDENCE

Giant Spin Density Fluctuations

By J. C. Phillips[†]
Royal Society Mond Laboratory, Cambridge

[Received August 17, 1960]

Recently Overhauser (1960) has presented a one-dimensional model of interacting fermions which has the remarkable property that it exhibits in the Hartree–Fock approximation spin density fluctuations in the presence of an arbitrarily weak repulsive interaction. He has also argued that the qualitative features of his results can be obtained in two and three dimensions, and has thereby called into serious question the modern electron theory of metals.

Overhauser's spin-fluctuation state is based on energy gaps generated by exchange. The situation in one dimension is especially favourable for two reasons:

1. Very little additional kinetic energy is required to generate the spin fluctuations. In the weak coupling limit (Overhauser's $n \rightarrow \infty$) the additional longitudinal kinetic energy vanishes exponentially.

2. The exchange interaction is coherent in one dimension, since only one propagation vector $\mathbf{q}$ is used. In general the additional exchange energy ΔJ (we use Overhauser's notation) contains a factor $\delta_{qq}{}'$. If the electrons are divided into m equivalent groups with different $\mathbf{q}$'s, ΔJ is multiplied by $1/m$. This has the effect of replacing n everywhere by mn.

To see how these factors nullify Overhauser's results in three dimensions, we consider the most favourable case, the cubic fluctuations sketched in Overhauser's fig. 2. In contrast to the one-dimensional case the perturbed states here necessarily have an additional 'transverse' kinetic energy ΔU arising from the non-spherical occupied region. Again choosing the most favourable case, $n=1$, we find

$$\begin{aligned} W &\simeq 2NE_{\mathrm{F}}(1-\coth 2mn), \\ &\simeq -4NE_{\mathrm{F}}\exp(-12) = -0{\cdot}024NE_{\mathrm{F}} \qquad (1) \end{aligned}$$

$$\Delta U \simeq 0{\cdot}024NE_{\mathrm{F}}, \qquad (2)$$

so that in this case the non-magnetic, ferromagnetic and spin-fluctuation states all have nearly the same energy. If $n < 1$, however, the ferromagnetic state will be lowest (since its exchange energy is not reduced by the factor m^{-1}) while if $n > 1$ the non-magnetic state will be lowest. In normal metals

---

[†] National Science Foundation Post-doctoral Fellow.

$$n \simeq 4E_{\mathrm{F}} / \langle v \rangle \simeq 10 \qquad \ldots \ldots \quad (3)$$

with $\langle v \rangle = N\gamma/L \simeq 2\,\mathrm{ev}$, $E_{\mathrm{F}} \simeq 5\,\mathrm{ev}$. Thus in normal metals W is negligible compared with ΔU.

Overhauser has suggested that ΔU can be reduced by increasing m. While it is not convenient to analyse all possible combinations of spin-fluctuation states, it can be seen from (1) that increasing m reduces W exponentially, while ΔU is decreased only like m^{-2}. Thus it appears that unless n is very near 1 either the non-magnetic or ferromagnetic Hartree–Fock states will have lower energy than Overhauser's spin-fluctuation states. This conclusion is apparently valid for fairly general short-range repulsive interactions (including screened Coulomb interactions).

Recently Kohn and Nettel (1960) have arrived at conclusions similar to ours in the weak interaction limit ($n \gg 1$), by very general arguments which apply explicitly to the Hartree state. While our arguments are more particular, they show directly why exchange generates spin density fluctuations in the Hartree–Fock states for one but not for two or three dimensions.

ACKNOWLEDGMENT

I am grateful to Dr. L. M. Falicov for assistance with certain calculations.

REFERENCES

KOHN W., and NETTEL, S. J., 1960, *Phys. Rev. Letters*, **5**, 8.
OVERHAUSER, A. W., 1960, *Phys. Rev. Letters*, **4**, 462.

The Etching of Sub-structures in Beryllium

By J. SAWKILL and J. E. MEREDITH
Tube Investments Research Laboratories, Hinxton Hall, Cambridge

[Received July 27, 1960]

IN the course of some work on the electropolishing of beryllium, using the commercial ' Disa Electropol ' apparatus and electrolytes, it was found that beryllium was being etched in addition to being electropolished. With commercially pure cast beryllium both grain boundaries and sub-boundaries were delineated, and in addition there were etch figures in the grains. It was subsequently found that the commercial A2 electrolyte, containing, according to Jacquet (1956), perchloric acid, ethyl alcohol, and butyl cellosolve, could be used simply as an etchant on surfaces previously electropolished or mechanically polished. However, a fresh solution did not etch the boundaries. Only after electropolishing beryllium with it for a few hours did the solution work as an etchant. It was also discovered that the etchant did not pit the surface, but rather, it produced a deposit at the boundaries. For example, the boundaries could be ' moved ' by brushing the surface, and observations in phase contrast illumination showed the boundaries to be standing proud of the general surface.

An attempt was made to analyse the deposit by evaporating a carbon film on to an etched surface, stripping it, and examining the film, with the deposit attached, by electron diffraction in an electron microscope. The deposit could easily be recognized in the microscope, but it did not give a crystalline diffraction pattern. Recently, however, etched surfaces have been examined in an electron probe X-ray microanalyser and the deposit has been shown to be copper.

The action of the etchant is thus to decorate the boundaries and other sites with copper, and it is presumed that the fresh solution did not etch because it did not contain copper ions, whereas the electropolishing of beryllium allowed the copper, present as an impurity in the metal, to go into solution. The next step was to add a few crystals of copper sulphate to the fresh A2 solution, and this then etched perfectly well. Finally, it has been shown that the A2 solution is not necessary as an ingredient. The best etchant found so far is an aqueous solution of copper sulphate, with the copper content at a few hundred parts per million. It is also possible to deposit silver at the boundaries using a silver nitrate solution, and gold using a gold chloride solution, although in the latter case the chloride ions cause excessive pitting of the surface.

Figures 1 and 2† show respectively the microanalyser electron image and x-ray image taken in copper radiation from a surface etched in copper sulphate solution. Figure 2 shows conclusively the copper at the three grain boundaries and additionally at sites within the grains. It was possible to prove that the radiation came from the deposit and not, for example, from the grain boundaries themselves.

Examples of the use of the copper sulphate etchant are given in figs. 3 and 4. Figure 3 is an optical micrograph of cast beryllium showing sub-boundaries and grain boundaries. Figure 4 shows the complex polygonized structure produced by deforming hot extruded beryllium at room temperature and annealing for 24 hours at 850°c. In both cases the misorientations across the sub-structures were such that they could not be detected by polarized light methods. Some recent experiments on the heat treatment of beryllium indicate that impurities in the metal may play a part in the etching reaction.

ACKNOWLEDGMENTS

We thank Mr. A. E. Parsons for assistance with the metallography and Miss M. Nevard for carrying out the x-ray microanalysis. Part of this work was supported by a contract from the U.K.A.E.A. This note is published by permission of the Chairman of Tube Investments Ltd.

REFERENCE

JACQUET, P. A., 1956, *Met. Rev.*, **1**, 214.

---

† All figures are shown as plates.

Stress Concentrations at Crystal Surfaces and the Embrittlement of Sodium Chloride

By D. M. Marsh
Tube Investments Research Laboratory, Hinxton Hall, Saffron Walden, Essex

[Received July 4, 1960]

The brittleness of ionic crystals has attracted considerable attention recently and the purpose of this letter is to suggest an explanation of this effect in terms of stress concentrations at surface steps and other irregularities. The author has been studying the stress concentrations which may exist at the root of such surface steps using frozen-stress photoelastic techniques on large models. The experimental results show that a step, as in fig. 1, exhibits a stress concentration factor at its root given by

$$\text{shear s.c.} = \text{tensile s.c.} = 1 + 0{\cdot}7\sqrt{(l/r)}.$$

This type of relation has been verified over large range of values of l/r and for two different riser angles. The point of note is that the stress concentration is found to be almost equal to that at a Griffith crack of comparable dimensions, and so may be very severe.

Fig. 1

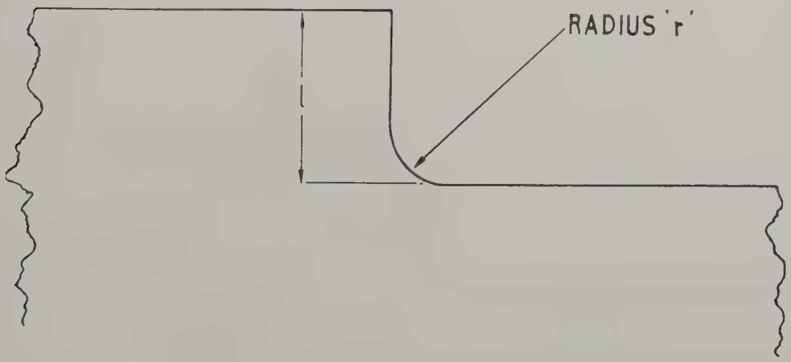

It is suggested that such stress concentrations embrittle ionic crystals by two alternative mechanisms:

(1) In a ductile crystal, failure is initiated at an internal defect which is only effective as a crack source after severe work-hardening and deformation of the whole crystal, as only then will it sustain a fatal stress concentration (Stokes *et al.* 1959 a). However, a surface stress concentration provides an alternative crack source which is available from the beginning of stressing and so may cause almost immediate failure.

(2) The surface stress concentration raises the stress locally so that a small length of crystal deforms and fractures before there is much overall strain. This embrittlement is assisted by the flow-induced fracture mechanism (Stokes *et al.* 1959 a) specific to ionic crystals, which limits the permissible *local* flow before fracture.

The experimental evidence for the first mechanism is provided by the fracture faces of many brittle specimens on which the surface defect responsible for failure can be clearly seen at the source of fracture. This experimental evidence was suggested by some interesting results of Stokes *et al.* (1959 b). They showed that NaCl single crystal bars could be made reliably and permanently ductile by washing, if every trace of solution was subsequently removed from the surface. However, their as-cleaved specimens were often brittle, and ductile specimens could be made brittle by two treatments :—

(1) If a drop of solution was allowed to dry on the surface to form a ' stain '.

(2) If carborundum was sprinkled onto the specimens.

They further showed that while fracture of the ductile bars was initiated internally, the failure of brittle specimens started at the surface. However, the present author has found that not only is failure initiated at the surface in such specimens, but also that a surface step or notch could be found at the source of the fracture. For example, fig. 2 (*a*) (Pl. 151) shows that fracture started from a step on the surface of a ' stained ' specimen and fig. 2 (*b*) shows initiation at a cleavage step which intersects the fracture face. The effect of cleavage steps may be further demonstrated by deliberately cleaving specimens slightly skew to the {100} faces to give gross steps. Such specimens are invariably brittle. Fracture faces of carborundum-treated specimens show that failure starts from the roots of sharp notches which have been chipped out of the specimen surfaces. In contrast fig 2 (*c*) shows the internal initiation of fracture in a washed specimen.

In general a complete range of surface-initiated fractures may be found from those in which fracture is almost completely brittle as in fig. 2 (*b*) to those in which the surface stress concentration is small and considerable flow has occurred before failure. In the latter instances it is presumed that the small surface stress concentrations have been assisted by the long-range stress concentrations, created by plastic flow, which cause the characteristic ' chequerboard ' patterns observed in polarized light.

Experimental evidence for the second embrittling mechanism (i.e. localization of strain) is provided by an experiment in which small semi-circular notches were washed out of NaCl bars before annealing. These were found to be brittle in four-point bending despite being given the standard washing treatment (Stokes *et al.* 1959 b) after the anneal. Micrographs in polarized light showed intense deformation at the notch only, while the fracture at the notch showed the characteristic ductile failure as in fig. 2 (*c*). Thus premature failure was by localization of slip rather than by limitation of slip.

One advantage of the present theory is that it provides a common mechanism for all of the above specimens and no evidence was found in NaCl for the special embrittling mechanism suggested by Stokes *et al.* (1959 b) to account for the brittleness of their stained specimens. However, microcracks such as they found in 'as-cleaved' MgO, certainly assist embrittlement when present.

It is important to ensure that the proposed mechanisms are not equally applicable to metals as these do not exhibit this embrittlement. It is also important to ask why the surface steps and notches do not render themselves harmless by flow as do stress concentrations in metals. Two obvious reasons are :

(1) The surface stress concentrations can be more easily and quickly relieved in metals owing to the higher mobility of dislocations and the larger number of slip systems available.

(2) In ionic crystals relief of the stress concentration by flow merely promotes failure by the second mechanism—a mechanism which is much more effective in ionic crystals due to the internal defect mentioned above.

In summary, it has been suggested that the embrittlement of NaCl is often due to the presence of surface steps and notches which act as stress raisers and cause premature failure by two distinct mechanisms. A fuller and more rigorous treatment of these ideas will appear elsewhere.

ACKNOWLEDGMENTS

My thanks are due to Mr. J. E. Gordon and other colleagues for their interest and helpful criticism of the manuscript. The letter is published by permission of the Chairman of Tube Investments Limited.

REFERENCES

STOKES, R. J., JOHNSTON, T. L., and LI, C. H., 1959 a, *Phil. Mag.*, **4**, 920; 1959 b, Sixth Tech. Rep. ONR Project No. 2456 (00) NR 032–451 (to be published in *Trans. Amer. Inst. min. (metall.) Engrs*).

REVIEWS OF BOOKS

Elements of the Kinetic Theory of Gases. By E. A. Guggenheim. (Pergamon Press, 1960.) [Pp. xii + 92.] Price 17*s*. 6*d*.

The physicist or physical chemist whose knowledge of the kinetic theory of gases stops at about the level of the formula $\eta = \frac{1}{3}nm\bar{c}l$ is often daunted by the mathematical complexity which accompanies more exact treatments of transport phenomena. Professor Guggenheim does not eschew mathematics—that is not his purpose—but by taking as his standard example the hard sphere model of a gaseous molecule he is able to explain the physical basis of the sophisticated theory with a minimum of computational involvement. Moreover, he shows that even this crude model can be made to give fairly close agreement with experiment when it is worked out correctly. The moral of this analysis, that this sort of data does not give any exact indication of the form of intermolecular forces, he drives home by a similar careful discussion of the second virial coefficient in terms of the scarcely less crude square well potential. In a final chapter he employs data for solid as well as gaseous argon to synthesize an interaction potential for this particular atom. Here, as in the rest of the book, the clarity of the presentation gives great pleasure ; one can recommend the book with enthusiasm to anyone who wishes to take his understanding of kinetic theory beyond the scope of a normal undergraduate course.

A. B. P.

An Introduction to Thermonuclear Research. Albert Simon. (Pergamon Press, 1959.) [Pp. ix + 182.] 35*s*.

The full title of this book, which is *An Introduction to Thermonuclear Research.—A series of lectures given in* 1955, gives a very good indication both of its scope and limitations. Although an enormous number of papers on controlled thermonuclear research have appeared since the removal of security restrictions in 1958, there have been very few attempts to provide books which assemble the material in an orderly fashion for the benefit of the non-specialist reader. Dr. Simon's book sets out to explain to such a reader what is being attempted, but does not attempt to explain what progress has been made in recent years. For no attempt has been made to refer to material published since 1956, and the reader who is looking for an up-to-date account of the subject will be disappointed. But the book does provide an excellent introductory account of the more important proposals for making thermonuclear reactors. It is clearly written, and the author explains the subject by means of simplified qualitative arguments, avoiding long and complicated mathematics.

The early chapters deal with the potentialities of fusion reactors, the basic conditions which have to be met in such reactors, and the motion of charged particles in magnetic fields. In the next four chapters, the author explains the fundamentals of the Stellarator, of mirror machines and of pinch devices. Finally there is a chapter on stability and another on the diffusion of plasma across magnetic fields. The emphasis throughout is on the principles involved, and very little is said about experimental apparatus or results.

T. F. J.

BOOK NOTICES

Progress in Elementary Particle and Cosmic Ray Physics. Vol. V. Edited by J. G. WILSON and S. A. WOUTHUYSEN. (North Holland Publishing Company.) [Pp. 461.] £4 5*s.* 0*d.*

A Collection of Mathematical Problems. By S. M. ULAM. (New York : Interscience Publishers.) [Pp. 150.] $5.00.

Penetration of Charged Particles in Matter. Proceedings of an Informal Conference, Gatlinburg, Tennessee, September 15–18, 1958. Edited by E. A. UEHLING. Nuclear Science Series Report No. 29. (Washington, D.C. : National Academy of Sciences, National Research Council, 1960.) $2.00.

A Physics Anthology. Edited by N. CLARKE. (London : Chapman & Hall.) [Pp. 323.] £1 15*s.* 0*d.*

Physical Methods in Chemical Analysis. Vol. 1. Second revised edition. Edited by WALTER G. BERL. (New York and London : Academic Press.) [Pp. 686.] $19.00.

Experimental Physics for Colleges. Revised edition. By WALTER A. SCHNEIDER and LLOYD B. HAM. (New York : The Macmillan Company.) [Pp. 442.] £1 14*s.* 6*d.*

Chemical Instrumentation. A Systematic Approach to Instrumental Analysis. By HOWARD A. STROBEL. (Reading, Massachusetts and London : Addison-Wesley Publishing Company.) [Pp. 653.] £3 14*s.* 0*d.*

University Physics. By F. C. CHAMPION. (Glasgow : Blackie & Son Ltd.) [Pp. 786.] 30*s.*

Electromagnetic Wave Propagation. International Conference sponsored by the Postal and Telecommunications Group of the Brussels Universal Exhibition. Edited by M. DÉSIRANT and J. L. MICHIELS. (London and New York : Academic Press.) [Pp. 730.] $22.00.

ERRATA

On Dislocations Formed by the Collapse of Vacancy Discs, by C. Elbaum, 1960, *Phil. Mag.*, 5, 669.

Page 670, line 12: increases *should read* decreases.

Page 671, eqn. (5): the equation should read as follows:

$$T_c = \frac{1 - A\dfrac{(\mu \mathbf{b}^3)_{T_0}}{U_f}\,1 + 300(\beta + 3\alpha)}{\dfrac{1}{T_M} + A\dfrac{(\mu \mathbf{b}^3)_{T_0}}{U_f}(\beta + 3\alpha)} \quad . \quad . \quad . \quad . \quad . \qquad (5)$$

[*The Editors do not hold themselves responsible for the views expressed by their correspondents.*]

Fig. 1

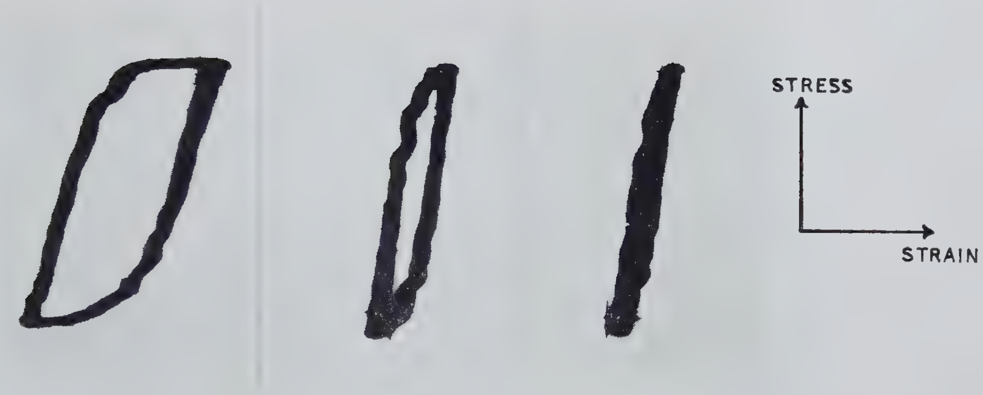

(*a*) (*b*) (*c*)

Hysteresis loops from an aluminium crystal fatigued at ±700 g/mm^2 resolved shear stress at room temperature. (*a*) 400 cycles (0·6% life), (*b*) 2800 cycles (4% life), (*c*) 40 300 cycles (57% life).

Fig. 2

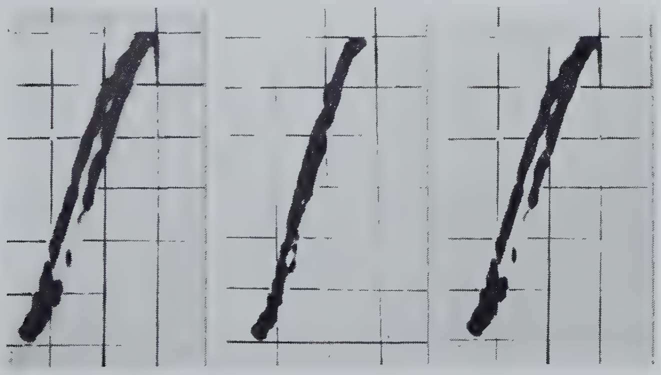

(*a*) (*b*) (*c*)

Hysteresis loops from a crystal fatigued at ±1015 g/mm^2 resolved shear stress at −78°c. (*a*) 6500 cycles, (*b*) 6500 cycles, rested at room temperature then re-tested, (*c*) 6600 cycles.

Fig. 1

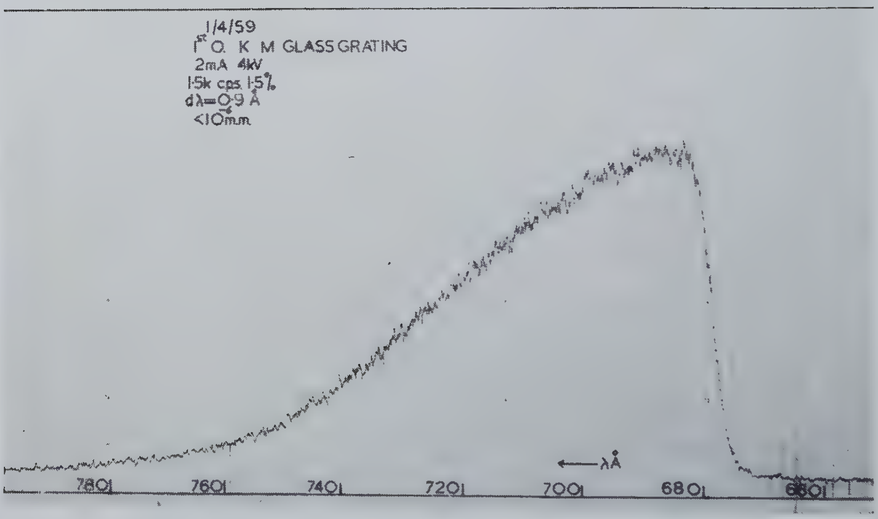

The M emission band of solid potassium.

Fig. 3

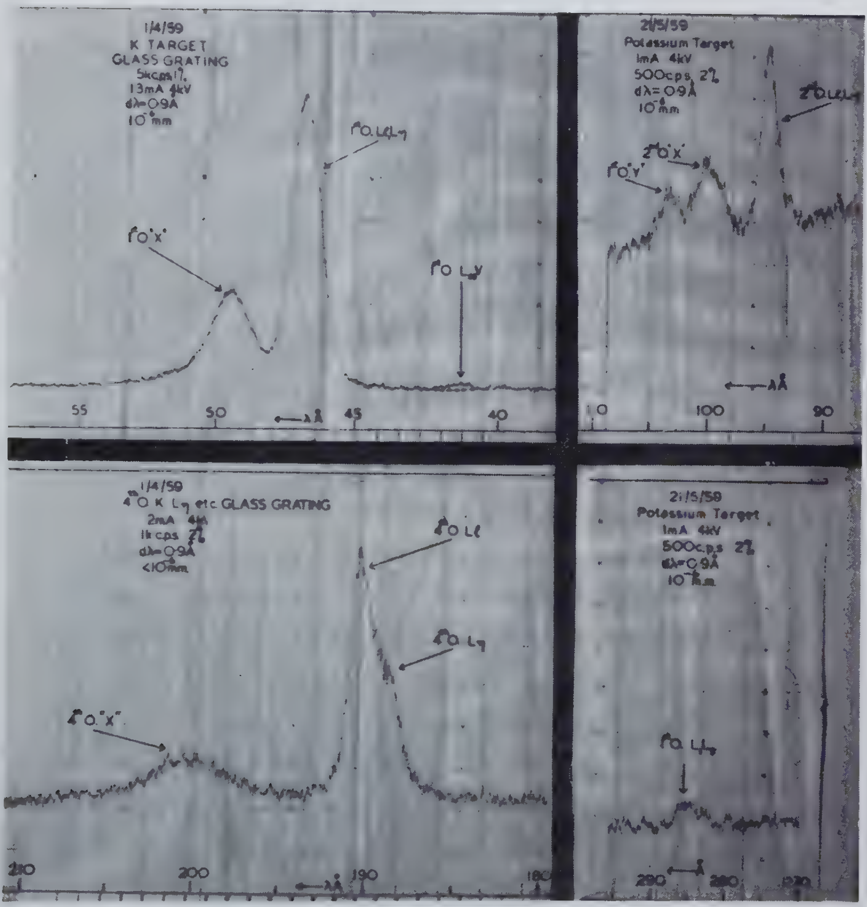

Emission lines from solid potassium in the 40–1000 Å range.

Upper left: 1st O.L_{23}V, 1st O.Ll, Lη, 1st O.X.
Upper right: 2nd O.Ll, Lη, 2nd O.X, 1st O.Y.
Lower left: 4th O.Lη, 4th O.Ll, 4th O.X.
Lower right: 1st O.L_1L_3.

Fig. 1

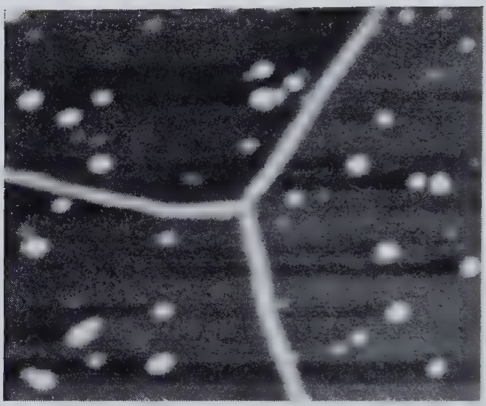

Microanalyser electron image of junction of grain boundaries.
Etched in copper sulphate solution. ×1450.

Fig. 2

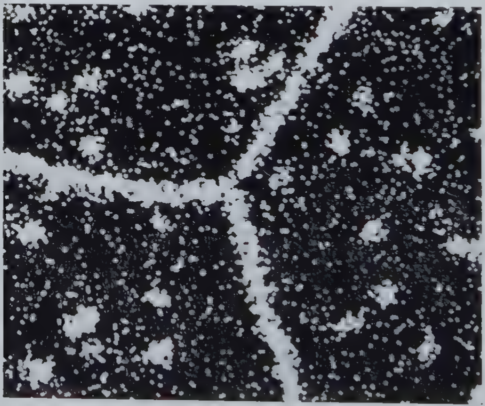

Same field as fig. 1, x-ray image taken in copper Kα radiation. ×1450.

Fig. 3

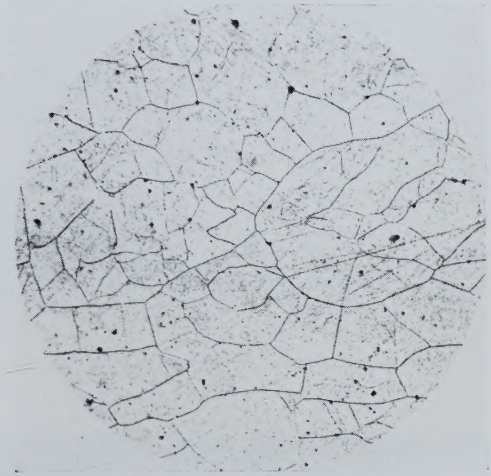

Optical micrograph of cast beryllium showing grain and sub-boundaries.
Etched in copper sulphate solution. × 55.

Fig. 4

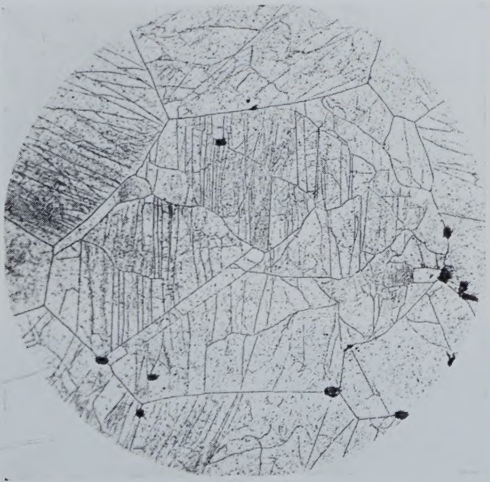

Complex polygonized structure in deformed and annealed beryllium.
Etched in copper sulphate solution. × 110.

Fig. 2

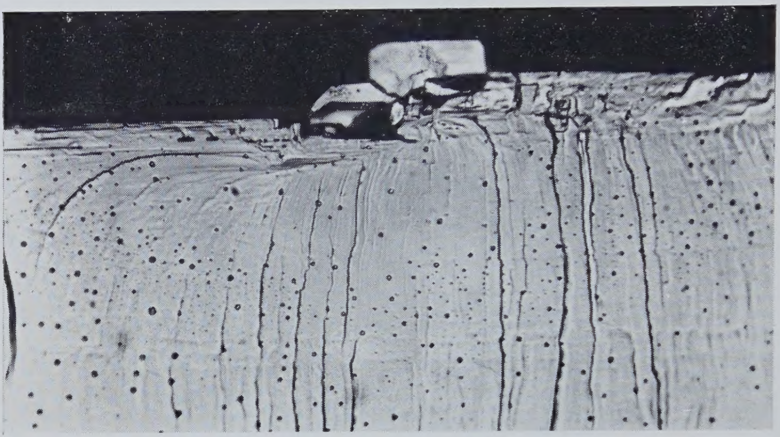

(*a*) ‘Stained’ specimen (×570).

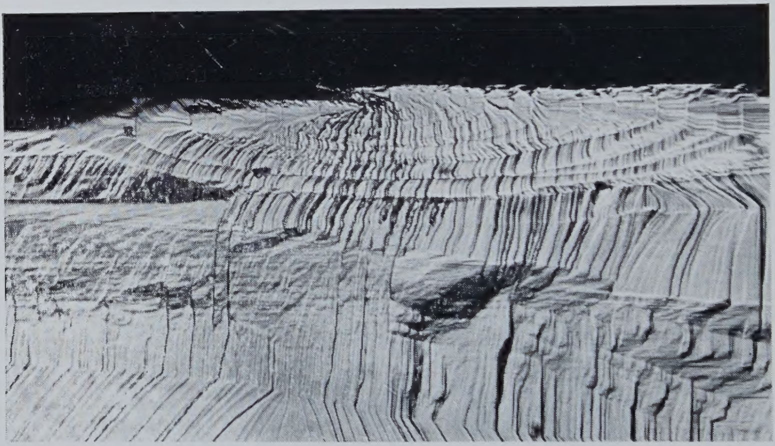

(*b*) As-cleaved specimen (×100).

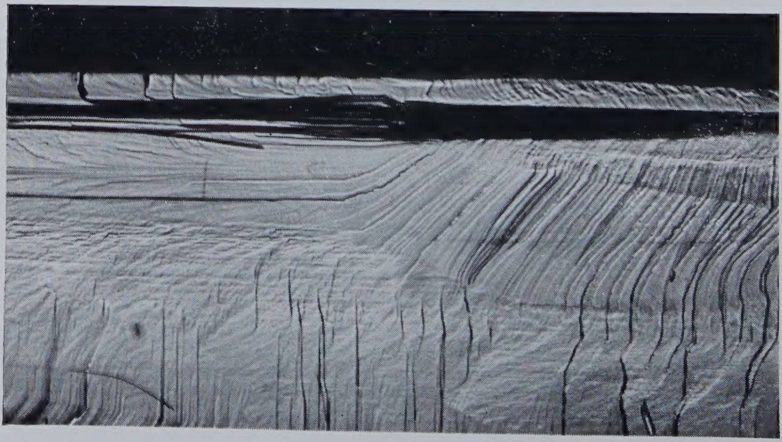

(*c*) Standard washed specimen (×100).

Fracture faces of NaCl.